Mechanical Properties of cBN-Al Composite Materials Dependence on Grain Size of cBN and Binder Content

Amanda Lynne McKie

A dissertation submitted to the Faculty of Engineering and the Built Environment, University of the Witwatersrand, Johannesburg, in fulfilment of the requirements for the degree of Master of Science in Engineering.

October 2009

DECLARATION

I declare that this dissertation is my own unaided work. It is being submitted to the degree of Master of Science in Engineering to the University of the Witwatersrand, Johannesburg. It has not been submitted before for any degree or examination to any other University.

Amanda Lynne McKie

---------- day of ---------- 2009

ABSTRACT

PcBN materials have been widely used as cutting tools for ferrous materials for which PcD materials have limitations. Like diamond, cBN has excellent properties, a hardness in excess of 40 GPa, good thermal and chemical stability and good thermal conductivity. Several research studies have gone into the development of PcBN materials, but very little has been done on determining the mechanical properties affecting them.

It is important to know the mechanical properties of polycrystalline cBN materials such as hardness, fracture toughness and strength (σ_f) in order fully to understand the behaviour of these materials in application. There has not yet been an extensive mechanical testing out on cBN-Al composites.

The aim of this project is to investigate the relationship between the microstructure and mechanical properties for a wide range of composite materials based on polycrystalline cubic boron nitride and aluminium as a binder phase (PcBN-Al). The PcBN-Al composites were made using high-pressure high-temperature (HPHT) sintering methods, yielding materials with grain sizes of cBN of between 2 – 20 μm and an amount of Al binder of between 15 – 25 vol.%.

Mechanical properties tested were hardness, fracture toughness, K_{IC}, R-curve behaviour and transverse rupture strength (TRS). Hardness ranged between 15 – 40

GPa, while fracture toughness and strength were between 6.4 – 8.0 MPa.m$^{1/2}$ and 355 – 454 MPa, respectively.

Fractography was employed to rationalize the scatter in fracture strengths, to understand the nature of the flaws and correlate fracture strength with fracture toughness through the size of the fracture origins.

The main findings concerning structure properties relationships of the PcBN-Al composite materials are: There is a strong dependence of hardness on grain size and binder phase, but a weaker dependence exists for fracture toughness and strength. The results confirm that the hardness increases with increasing cBN grain size and decreasing binder content. Fracture toughness generally increases with increasing cBN grain size for low binder contents and decreases with increasing binder content. R-curve behaviour was also found. It is suggested that the toughening mechanisms involved in the cBN-Al composites are due to crack and grain bridging.

Strength decreases with increasing cBN grain size and there is no relationship with a change in binder content. Large strength limiting flaws were found to exist in the materials, these flaws ranged between 100 – 500 μm. The strength limiting flaws are caused mainly by large binder pools.

DEDICATION

I dedicate this work to the most important people in my life; my mom, dad and brother.

Thank you for all your help and support.

ACKNOWLEDGEMENTS

I would like to acknowledge the following people for their valuable contributions which facilitated the completion of this research work.

a) Prof. I. Sigalas for suggestions and supervising this work.
b) Dr. M. Herrmann for his advice, useful comments, time and constructive criticism.
c) Prof. J. Rödel for the use of the NAW facilities and his advice.
d) Element Six (Pty) Ltd – Diamond Research Laboratory for their financial support.
e) NRF Centre of Excellence in Strong Materials for financial assistance.
f) The staff at Element Six (Pty) Ltd – Diamond Research Laboratory, especially Josias, Rod, Festus, Themba, Nedret and Hester for their help and advice.
g) Jami, Ludwig and the rest of the staff of NAW, Technische Universitate of Darmstadt, for their help and advice.
h) K. Katuku for his time and assistance in achieving good SEM images and useful advice.
i) My family, especially my mom, dad and brother, for their support and sacrifices throughout this period.

TABLE OF CONTENTS

LIST OF FIGURES

Figure **Page**

LIST OF TABLES

Table **Page**

LIST OF SYMBOLS:

A – Area of plastic contact (m^2)

a – notch length (μm)

a – length of the moment arm (mm)

a_C – critical flaw size (μm)

a_O – length of pre-crack (μm)

α – thermal expansion coefficient ($10^{-6}K^{-1}$)

B, b – specimen thickness (mm)

c – Crack length (μm)

d – Grain size (μm)

d – Average length of diagonals (mm)

E – Young's modulus (GPa)

f – Volume fraction

F – Fracture load (MN)

G – Grain size (μm)

H – Hardness (GPa)

$K_{1\ \&\ 2}$ – Strength coefficient

K_{IC} – Fracture toughness ($MPa.m^{1/2}$)

K_{IF} – Crack resistance ($MPa.m^{1/2}$)

K_{SE} – Steady state crack resistance ($MPa.m^{1/2}$)

l – Length of crack tip (μm)

m – Weibull modulus

m_i – mass % of component i

n – Notch length (μm)

ρ – Density (g/cm^3)

P – Applied load (N)

P_f – Probability of failure

P(V) – Probability of occurrence of a critical defect.

$S_{1\ \&\ 2}$ – Outer and Inner support spans

σ – Applied stress (MN)

σ_f – Fracture strength (MPa)

σ_O – material constant for starting strength (MPa)

σ_θ – Characteristic strength (MPa)

T – Temperature (K)

ν – Poisson's ratio

V – Volume (cm^3)

V_O – Mean Volume (cm^3)

W – Specimen width (m)

W_{dry} – Dry Weight (g)

W_{sat} – Saturation Weight (g)

W_{Susp} – Suspended Weight (g)

Y – Stress intensity factor

Chapter 1: Introduction and Motivation

Sintered superhard materials such as diamond and cubic boron nitride are used extensively in machining due to their excellent properties such as high hardness (cBN has a hardness of 45 GPa, half that of diamond), good thermal conductivity and chemical and thermal stability. Diamond compacts are widely used as cutting tools for materials such as glass, stone, concrete, ceramics and other hard abrasive materials. Diamond has its limitations; it cannot be used for the machining of ferrous materials, as it reacts with iron at temperatures above 700°C [(1)]. However, cBN compacts are relatively chemically inert to iron and thus thermally stable at temperatures as high as 1000ºC. This makes cBN a potential material for the machining of hardened ferrous materials.

Intensive research has been carried out to develop cBN materials, but there are only a few papers [(2,3,4,5,6,7,8)] dealing with the mechanical properties of cBN material such as hardness, fracture toughness and strength and most of them focused on hardness. These properties are especially necessary for materials that are used in applications where these properties are crucial such as in cutting tools.

In cutting applications, a material is needed which is very hard, with excellent strength and which has a high wear resistance and good thermal stability to withstand high operating temperatures without decomposing or significantly weakening. Good

fracture toughness and strength are also required, as they will determine the extent to which a material will fail through flaws and crack propagation.

The aim of this project is to determine the mechanical properties of PcBN-Al composite materials based on variations in the microstructure. The systematic change of microstructure will be achieved by varying the cBN grain size and the volume content of the binding aluminium metal. The effect of these changes to the mechanical properties will be analysed. A detailed flowchart describing the project process is shown in Figure 1.1

A detailed overview of the cBN-Al materials is presented in Chapter 2.

Chapter 3 contains a detailed description of the mechanical properties of cBN materials, such as the toughening mechanisms and effects of grain size and binder content.

Chapter 4 contains a detailed description of all the powder processing and experimental procedures, equipment and testing techniques used in the project.

Chapter 5 summarizes the results of the sintered composites analysis.

Chapter 6 summarizes the results of the mechanical properties. The effect of microstructure on the mechanical properties is discussed at the end of the chapter.

The conclusions and recommendations for future work are discussed in Chapter 7.

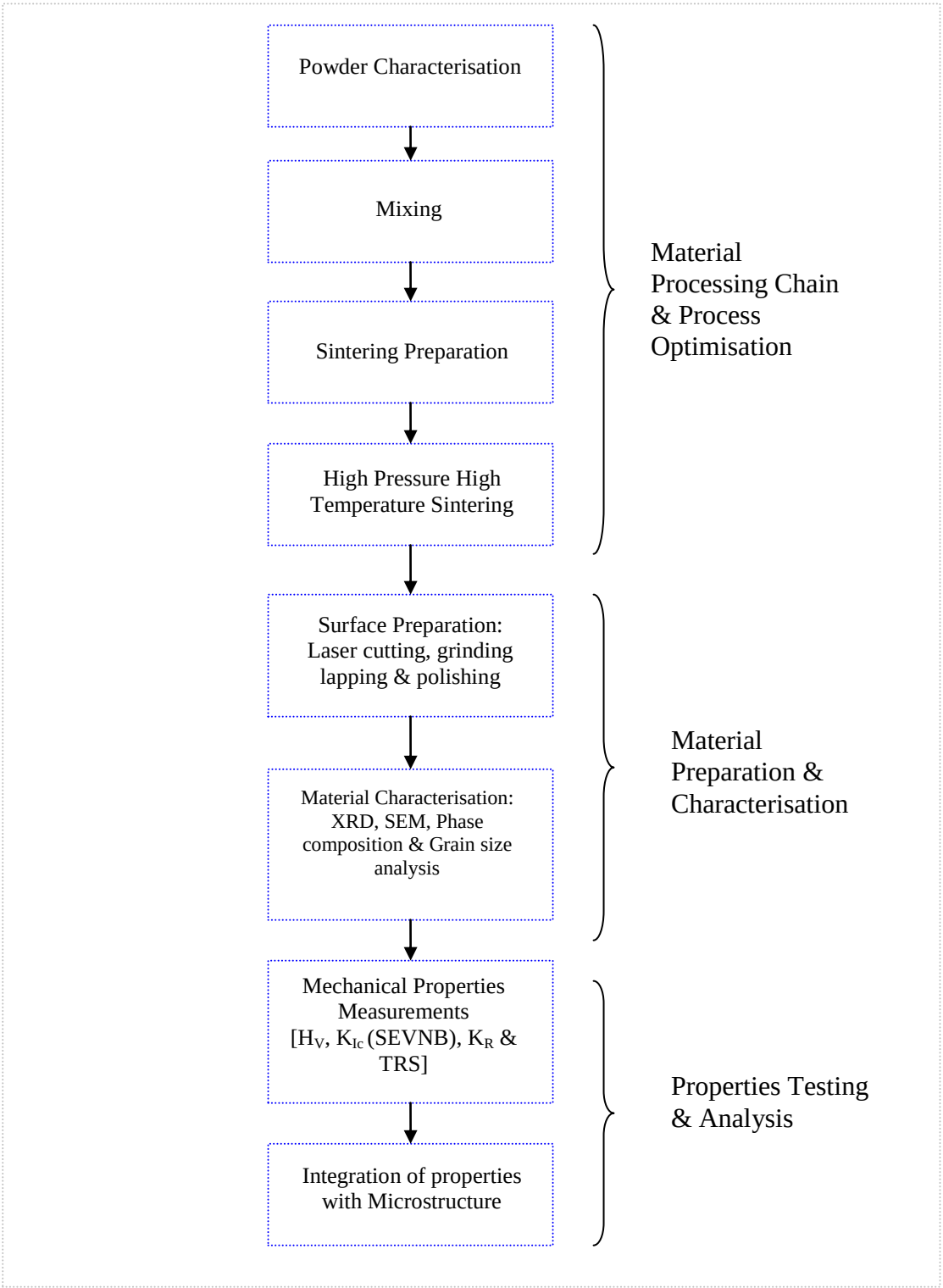

Figure 1. 1: Flowchart describing the sample preparation and testing for the research project.

Chapter 2: Overview of Boron Nitride Materials

2.1. History of Boron Nitride (BN) Materials

Boron nitride (BN) is a commercially synthesized material discovered in the early 19th century, but not used commercially until the 20th century. It consists of equal amounts of boron and nitrogen atoms and has a structure similar to carbon. Thus like carbon, BN has different allotropes; hexagonal BN (hBN), cubic BN (cBN) and wurzite BN (wBN), although hBN and cBN are the most common forms **(9)**.

Hexagonal boron nitride (hBN) is similar to graphite, consisting of layers of nitrogen and boron atoms combined in a hexagonal network. Between the layers only a weak bonding exists, therefore it has a soft material structure **(10)**. hBN is produced by nitridation or the ammonolysis of boron trioxide (B_2O_3) at elevated temperatures. Due to its graphite-like structure hBN is used as a lubricant in various applications where the chemical reactivity and the electrical conductivity of graphite would cause problems if used **(10,11)**.

The second most common BN form is cubic boron nitride (cBN); cBN has a zinc blende structure which resembles that of diamond. It consists of boron and nitrogen atoms in a three-dimensional network where B and C have 4 equivalent strong covalent bonds. It is extremely hard, although less than diamond. cBN is used as an

abrasive and as a cutting tool. cBN is formed by the conversion of hBN under high pressures (4 – 6 GPa) and temperatures (1200 - 1700°C) similar to the synthesis of diamond from graphite [11,12]**.** Figure 2.1 shows the crystal structure of BN allotropes.

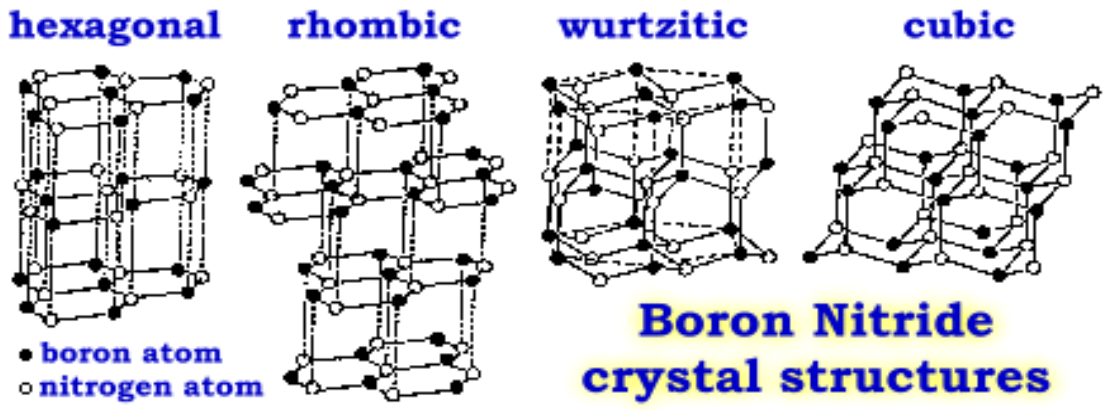

Figure 2. 1: Crystal structures of Boron Nitride allotropes [13].

2.2. Synthesis of Cubic Boron Nitride (cBN)

Cubic boron nitride (cBN) was first synthesized in 1957 by Wentorf [14].It was found that high temperature and high pressure conditions similar to those needed for the synthesis of diamond could be used to convert hexagonal boron nitride to the cubic form.

Wentorf [14] showed that cBN can be produced by the direct conversion of hBN to cBN by high-pressure high temperature treatment. The direct conversion of hBN to cBN can be done with pressures of up to 18 GPa and temperatures between 1750 and 3023°C. Additions of small amounts of boron oxide can lower the pressure to 4 – 7

GPa and temperature to 1500°C. Commercially cBN is synthesized by a mixture of hBN and various catalysts/solvents, which are subjected to pressures in the range of 4.5 – 5.5 GPa and temperatures between about 1200 - 1700°C [(11)]. The various catalysts/solvents that can be used are lithium nitride, calcium nitride and magnesium nitride.

Diamond and cBN have excellent properties such as high hardness, thermal conductivity and chemical stability. They are therefore used widely in industry applications, such as in cutting tools. Diamond is widely used as a cutting tool for hard materials such as concrete, stones, ceramics, non ferrous metals and other hard materials that have a low chemical reactivity with carbon. Due to the tendency of iron and its alloying elements such as nickel to react with diamond at high temperatures when machined and cause deterioration of the cutting tool [(15)], cBN was introduced as the alternative.

cBN is an extremely hard material, second only to diamond and it is chemically inert to iron and is thermally stable to temperatures as high as 1000ºC, better than that of diamond. It can also form passive oxide layers at high temperatures when in contact with oxygen. It is thus suitable for the machining of hard ferrous alloys. cBN particles also bind well to metals, forming interlayer's of metal borides or nitrides. The mechanical properties of single crystal cBN and natural diamond are given in Table 2.1.

Low-pressure methods can also be used to manufacture thin films of cBN on a substrate; such as CVD, PVD and ion beam deposition [16]. These methods result in materials with good properties and are also more cost effective when used on coatings.

Table 2. 1: Properties of cBN, PCD and diamond [11].

Property	**Diamond (natural)**	**cBN**
Density (g/cm^3)	3.5	3.48
Melting point (°C)	-	2700
Fracture Toughness ($MPam^{0.5}$)	3.4	5
Knoop Hardness (GPa)	57-104	43-47
Young's Modulus (GPa)	1141	600-800
Thermal expansion ($10^{-6}K^{-1}$)	1.5-4.8	4.9
Thermal conductivity $20^oC(Wm^{-1}K^{-1})$	500-2000	150-700

2.3. Production of Polycrystalline Cubic Boron Nitride (PcBN) Materials

Although single crystal cBN is useful, it is also limited in its use as only small particles of single crystal cBN can be produced. It is necessary for application purposes to produce materials containing polycrystal crystals of cBN joined together with a binder. Higher fracture toughness is introduced into polycrystalline cubic boron nitride (PcBN) materials with the addition of different binder phases. However, fully densified PcBN can only be manufactured through high pressure (~ 7 GPa) and high temperature conditions with the aid of binders. This is due to cBN's strong

covalently bonded structure, which is very difficult to compress and sinter at low pressures [11]. Still, research has been done on the sintering of PcBN materials at low pressures [17,18,19].

Wentorf and Rocco [20,21] sintered the first PcBN materials. The sintered PcBN material contained alloys of nickel, iron, cobalt and aluminium as binders. In the study of cBN to cBN bonding, it was believed to have been achieved by a liquid phase sintering process, which involved the binder alloys. Hibbs and Wentorf [22] produced high cBN-content cutting tools by infiltrating molten Al-Co from WC-Co substrate into cBN layers during high-pressure and high temperature sintering. In 1980 a patent was filed by Sumitomo Electric Industries Ltd [23] that covered the manufacturing of any sintered compact for a machining tool with 10-80% cBN and various binders comprising carbides, nitrides, borides or silicates of many of the metals. Other composites that have been formed recently include cBN-TiN [24,25], cBN-Al [1,3,8,26,27], cBN-WC-Co [28], cBN-Ti [29] and cBN-TiN-Al [6]. The composites of the cBN-Al system will be described in more detail in section 2.4.

High purity polycrystalline cBN single phase (binderless) materials have also been produced; these materials have the advantage of excellent mechanical and thermal properties free from the effects of the binder phase. Wakatsuki et al,[30] reported on the direct conversion of hBN to PCBN at low pressures of 55 kbar and temperatures of 1100-1400°C with no catalyst.

The commercial method of PcBN production is done by sintering together cBN with sintering additives or binder materials at pressures of 4-6 GPa and temperatures of between 1200 and 1500°C [(11)]. PcBN is sintered by cold and hot compaction stages and liquid phase sintering mechanisms. Reaction sintering plays a major role in the driving force of the densification process. A reaction between the BN and the metal binder occurs to form borides and nitrides. These act as the binder phase. The metal binders added influence the final properties of the material. Composite metals of the elements in groups IV-VI of the Periodic table are often used [(31)]. Other metals can also be added as a binder such as aluminium (group III), cobalt and nickel [(3,17)] as well as binders that can increase the thermal stability or wear resistance of the material such as titanium nitride (TiN) and titanium carbide (TiC). Aluminium has the lowest melting point at ambient pressures and can react with cBN under a mild temperature [(8)]. Studies by Hara and Yazu [(25)], Morgiel et al [(29)] and Rong et al [(6)] on the sintering of cBN-Ti based composites have shown that Ti can be used as an important binder to produce a material with thermal stability and wear resistance by forming TiN or TiC. The properties of the PcBN compact are determined by the final microstructure and the phases formed during sintering.

From chemical equilibrium calculations in the BN-Al system it is known that Al reacts with BN in a wide temperature and pressure range. The type and number of new phases formed through sintering depends on the temperature and pressure. The reaction mechanism is still unclear.

2.4. Synthesis of cBN-Al Composite Materials

The synthesis of cBN with Aluminium was first reported in 1987 **(1)** using high temperatures and high pressures. In this study, solid cBN reacted with molten Al to form residual binder phases of Aluminium nitride (AlN) and Aluminium diboride (AlB_2). The AlN and AlB_2 phases protected the internal surfaces from chemical attack and gave the material good thermal stability. cBN-Al type sintered materials have been commercially marketed and are known as Amborite. Figure 2.2 shows the microstructure of Amborite (De Beers/ Element Six Ltd). Some property comparisons of Amborite and other cutting tool materials are listed in Table 2.2 below.

When compared to the PCD material Syndite 010 or Tungsten Carbide (WC), as can be seen in the table above, Amborite has good properties. The strong covalent bonds in Amborite give it its good properties such as high hardness 31.5 GPa and good fracture toughness 6.36 $MPa.m^{1/2}$. The original cBN particles provide the hardness and wear resistance of the material, thus giving it use in cutting tool applications.

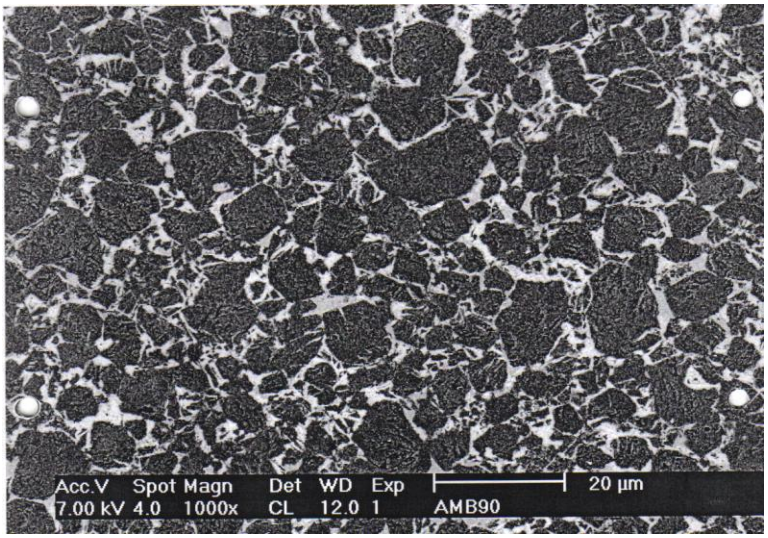

Figure 2. 2: SEM image of the microstructure of surface polished Amborite (courtesy of Element Six Ltd).

Table 2. 2: Properties of PcBN and other cutting tool materials [(11)].

	Amborite	**SYNDITE 010**	**WC/Co**
Density [g cm^{-3}]	3.41	4.127	14.7
Compressive strength [GPa]	2.73	4.74	4.5
Fracture toughness [$MPa.m^{0.5}$]	6.36	8.39	10.8
Knoop Hardness [GPa]	31.5	50	13.0
Young modulus [GPa]	653	993	620
Modulus of rigidity [GPa]	228	453	258
Bulk modulus [GPa]	297	412	375
Poisson's ratio	0.13	0.102	0.22
Thermal expansion coefficient [$10^{-6}K^{-1}$]	4.9	3.8	5
Thermal conductivity [$W.m^{-1}K^{-1}$]	100	120	100

In a study conducted by Rong and Fukunaga [(24)] on the sintering behaviour of the cBN-Al system they described the reactions occurring during high-temperature and high-pressure conditions in which cBN powder (1-3 μm) was mixed with Aluminium

powder (1-4 μm) in various compositions ranging between 50 and 90 mol% cBN. The powders were sintered at temperatures of between 1200 and 1400˚C and a pressure of 5.75 GPa. The residual binder phases formed were Aluminium nitride (AlN), Aluminium diboride (AlB_2) and α-AlB_{12}. The reaction of the cBN-Al system can be observed in the following reactions:

$$2BN + 3Al \rightarrow AlB_2 + 2AlN \quad (1)$$

$$12BN + 13Al \rightarrow \alpha - AlB_{12} + 12AlN \quad (2)$$

Rapid grain growth of AlN and AlB_2 was observed during sintering, consequently lowering the mechanical strength. TEM analysis of the cBN-Al composites showed that the AlN phase existed around the cBN grains, while the AlB_2 and AlB_{12} phases existed between the AlN-AlN phase. The diffusion of B ion was faster than the N ion within the aluminium liquid.

Knoop Hardness measurements were done on the sintered cBN-Al compacts **(26)** sintered at 1200˚C and 1400˚C. Later Rong and Fukunaga **(6)** added TiN as a secondary phase to the cBN-Al system to prevent the rapid growth of the AlN and AlB_2 grains and to improve its properties. TiN has an intermediate thermal expansion coefficient between that of cBN and Al; this prevents cracking in the microstructure. The sintering of cBN-TiN-Al resulted in the cBN grains reacting with the TiN to

form TiB_2 and AlN. The TiB_2 and AlN formed around the cBN and TiN grains and reinforced the strength of the matrix.

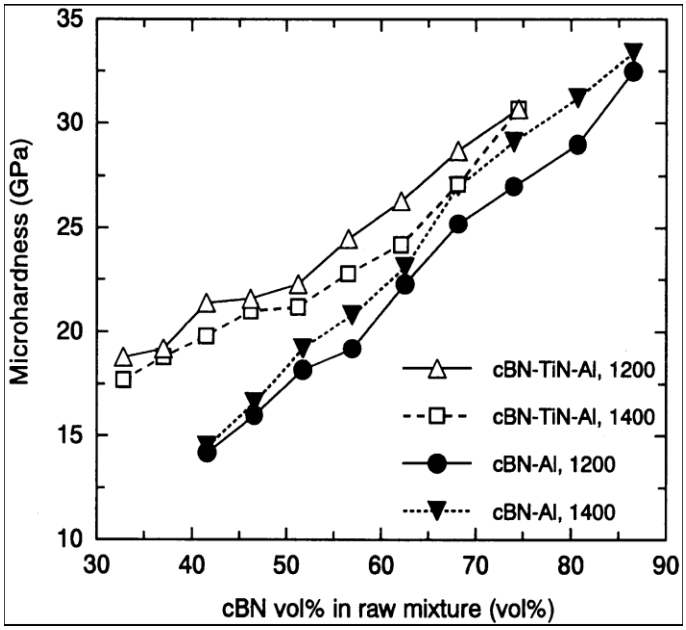

Figure 2. 3: Comparison of the Knoop hardness of the cBN-TiN-Al system and the cBN-Al system [(6)].

Figure 2.3 also shows the Knoop hardness values for the cBN-TiN-Al samples sintered at 1200 - 1400˚C. The samples sintered at 1200˚C have a higher hardness than that of the 1400˚C samples across the composition range. This resulted in the TiN reducing the sintering temperature of the system.

Compared with the hardness values of the cBN-Al system (Figure 2.3), the hardness of the cBN-TiN-Al system was always higher than the cBN-Al system at 1200˚C and 1400˚C. The addition of the relatively hard TiN enhanced the hardness of the binder phase especially in the region of the lower cBN compositions. While in the cBN-Al

system at the lower cBN compositions significant amounts of AlB_2 were formed which was softer and thus lowered the hardness of the system. Thus by adding TiN to the composite the hardness was increased at a lower sintering temperature. Table 2.3 shows the main phases found in PcBN-Al composites after sintering and the properties associated with each phase.

Table 2. 3: Properties of the main phases found in PcBN-Al products after sintering [(11)].

Properties	**cBN**	**Diamond**	**AlN**	**AlB_2**	**AlB_{12}**
Crystal structure	Cubic	Cubic	Hexagonal	Hexagonal	Tetragonal
Density [g/cm^3]	3.48	3.51	3.26	3.17	2.57
Melting Point [°C]	2700	-	2300	975	2070
Knoop Hardness [GPa]	47	57-104	12		24
Young Modulus [GPa]	700-800	1141	318		4.3
Thermal expansion coefficient [$10^{-6}K^{-1}$]	3.2	1.5-4.8	3.9		
Thermal Conductivity [$W.m^{-1}K^{-1}$]	150-700	500-2000	200		

Research on the phases present in cBN-Al materials sintered under HP-HT conditions was looked at by Zhao and Wang [(27)] in which cBN powder (3-5 μm) was mixed with Al powder (38 μm) in a volume ratio of cBN:Al = 7:3. Sintering was done at about 5.5 GPa at temperatures ranging from 1300ºC - 1500ºC for 10 min.

Figure 2.4 shows the XRD results which show that at 1300ºC no AlN or AlB_2 was observed therefore no reaction had taken place between the cBN and Al. At 1400ºC,

new phases (AlN and AlB_2) were formed while retaining some Al. At 1500ºC all Al disappeared and only AlN and AlB_2 remained with the cBN. The XRD and TEM results showed that the Al reacted with cBN at 1400ºC to produce AlN and AlB_2. Al atoms diffused into the hBN layer of cBN particles and reacted with hBN to form AlN, while B atoms diffused into the Al zone and reacted with Al to form AlB_2.

Recently Li et al **(8)** investigated the high pressure sintering behaviour of cBN-Al composites on WC/Co substrates at various temperatures and cutting performance. Hardness results showed a decrease with increasing binder content.

Benko et al **(3)** also did research on cBN-Al composite materials under hot pressing conditions. In this research composites with a BN:Al ratio of 9:1 was sintered under a pressure of 10 MPa and at a temperature of 1750ºC. The samples were then thermally treated in a vacuum of 3×10^{-3} Pa for 1 hour. Knoop hardness of the sintered compacts was measured before and after annealing. The study showed that the hardness increased from 10 to 20 GPa after annealing, which showed that in thermal annealing the compacts could increase the hardness of the material.

Sithebe **(18)** investigated the preparation of cBN-Al composites at low pressures by hot pressing 50vol.%Al with 50 vol.% cBN at different temperatures. Reaction between the cBN and Al was observed at temperatures between 1000ºC and 1400ºC under N_2 and Ar. AlB_2 started forming at 1100ºC, but disappeared above 1300ºC where AlB_{12} started to form. In this study Sithebe et al **(18,19)** also looked at pressure infiltration of

molten Al in a porous hBN or cBN matrix at 800ºC and 12 MPa. Fully infiltrated cBN performs were made with 12 μm cBN, while a limited extent of infiltration was achieved for 3 μm cBN grains. Results showed that the hardness was higher for the infiltrated cBN than the hBN.

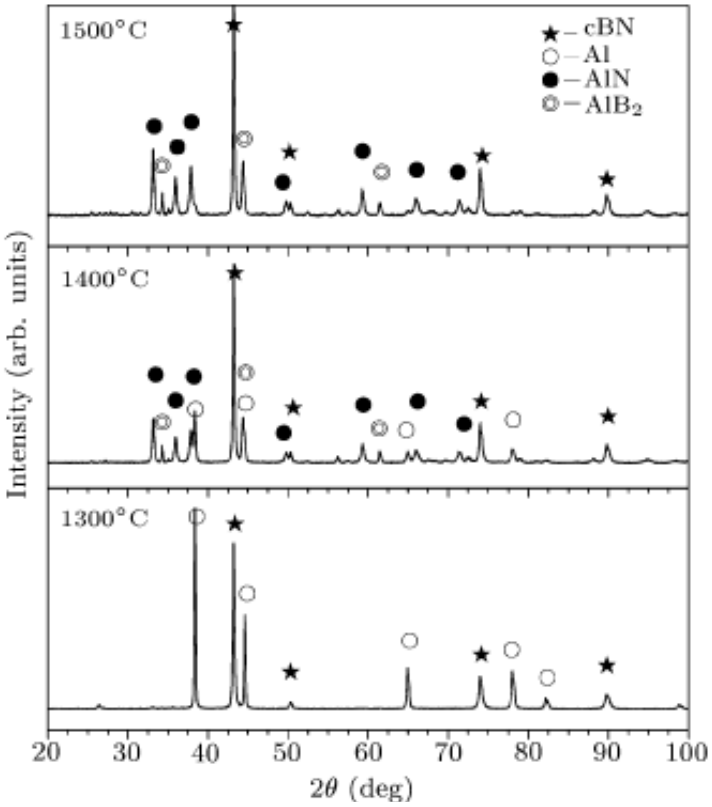

Figure 2. 4: XRD graph showing the phases present in the cBN-Al materials at temperature of 1300ºC, 1400ºC and 1500ºC [(27)].

Chapter 3: Strengthening & Toughening of cBN Materials

Ceramic materials and their composites are mostly brittle materials. Ceramics and ceramic composites are used in a wide variety of advanced engineering applications. Knowledge of how these materials behave is important in understanding their behaviour during application. It is essential to understand the structures to properties relationships for these materials.

Hardness, strength and fracture toughness are crucial in understanding when a material will fail in application. Failure of these materials during application can have consequences on productivity and operations. Failure of ceramic materials is caused by the extension of flaws, which are usually introduced into the material during processing or surface treatment such as grinding and polishing. Flaws in the material can be inclusions, pores and cracks.

The strength of a material is related to the maximum flaw size a_c, and the critical fracture toughness K_{1C}, of a material. So in order to improve the strength ($\sigma_{f,}$) of a material a reduction in the maximum flaw size a_c, and/or an increase in the critical fracture toughness K_{1C}, are required.

The Griffith equation shows the dependence of the strength (σ_f) of a material on the critical flaw size a_c and the fracture toughness K_{1C} [(32)].

$$\sigma_f = \frac{K_{1C}}{Y\sqrt{a_C}} \qquad (3.1)$$

Where Y depends on the position and shape of the crack, and can usually be taken to be $Y \approx 1$ for most ceramics, but can also be calculated using $Y = \sqrt{\pi}/2$ for penny-shaped cracks [(32)].

Since the strength of a material is both related to the flaw size and its fracture toughness, it is important to have a material with high fracture toughness. Fracture toughness is mostly influenced by microstructure. Improving fracture toughness therefore needs a tailoring of the microstructure.

3.1. Fracture Toughness

The fracture toughness of a material is a very important parameter, it is the material's resistance to crack propagation, but ultimately it is characterized by the critical stress intensity factor K_{1C} as the limiting value of stress intensity which can be applied to a material above which crack propagation will occur. K_{1C} corresponds to the critical stress intensity factor of the mode I fracture mode. There are 3 basic modes of crack tip deformation: the opening (mode I), the in-plane shear (mode II) and the out-of-

plane shear (mode III). Figure 3.1 shows the various fracture modes. Mode I is used for crack opening and tension applications.

Mode I: Tension, Opening; Mode II: In-plane shear, sliding and Mode III: Out-of-plane shear, tearing.

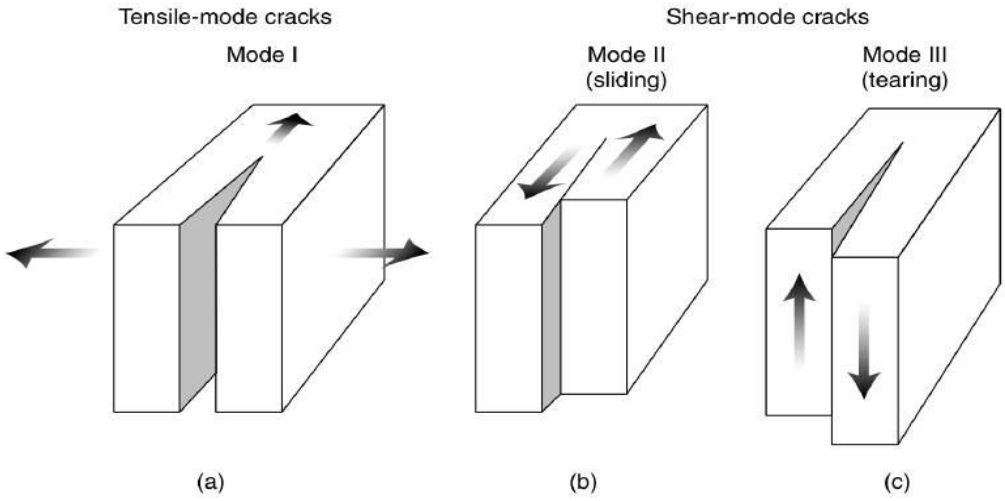

Figure 3. 1: Fracture modes of crack deformation [33].

3.2. R-Curve Behaviour

Since ceramics such as cBN-based materials are brittle they generally fail by brittle fracture. This puts some major limitations on applications. This has motivated researchers to develop ways of increasing the toughness of ceramics. The R-curve behaviour has thus been a characteristic feature of toughened ceramics.

The R-curve or Resistance curve behaviour concept of crack propagation arose from the studies of fracture in metals and alloys described by Broek (1986) [34], but was

later applied to ceramics [34,35,36,37]. The R-curve behaviour of a material is the enhanced resistance to crack growth during crack extension. R-curve behaviour is typically indicated by a rising fracture resistance curve. The crack tip is screened or prevented from propagating, causing an increase in the toughness of the material. The mechanisms involved in toughening materials will be described in Section 3.3.

The R-curve behaviour of a material can be seen in Figure 3.2, which shows the resistance of a crack to propagation with increasing crack length of a V-notched sample under 4-point bend loading. *n* symbolizes the length of the V-notch, which is constant for all specimens, and *l* and a_0 denote the length of the crack tip and length of the pre-crack respectively.

With increasing crack length the crack resistance increases due to shielding mechanisms in the precracked zone. After a certain distance the shielding and the distortion due to large crack openings are equal and a steady state of resistance is reached (K_{SE}).

Crack propagation occurs from the crack tip until steady-state toughness (K_{SS}) is reached. This remains so until fracture occurs. Ceramic materials exhibiting R-curve behaviour are more flaw-tolerant than ceramics that do not [38]. In Figure 3.2, the dotted line shows a flat curve which means that no R-curve behaviour occurs.

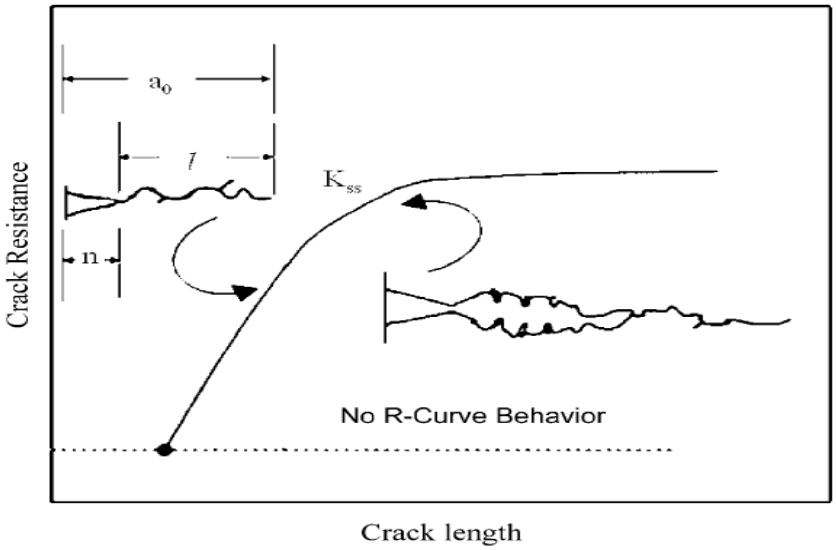

Figure 3. 2: A graphical representation of the ideal dependence of fracture toughness with flaw size of a ceramic material. The top curve shows the rising R-curve behaviour and the bottom curve a flat R-curve behaviour [(38)].

R-curve behaviour results in [(32)]**:**

1) Materials with a rising R-curve show an increase in their strength compared with a material with the same crack tip toughness and a flat R-curve. Materials with coarse grains and two phases with an elongated or needle-like phase lead to a rising R-curve and thus higher strength values.
2) A rising R-curve decreases the scatter in the measured strength from sample to sample compared to a material with the same crack tip toughness.
3) R-curve behaviour can be determined by macrocracks.

The various types of toughening mechanisms involved in the toughening of materials are given in Section 3.3. In a study on R-curve behaviour by various researchers and summarised by Munz [(32)], non-phase transforming ceramics with rising R-curves have

crack face interactions which are responsible for the rising crack growth resistance observed. These crack face interactions are usually crack deflecting or bridging in nature.

3.3. Toughening Mechanisms

One of the objectives of developing advanced ceramic composite materials is a high reliability. To achieve this, the flaw size distribution and toughening mechanisms acting in the material need to be controlled. The flaw size control approach takes into account the brittleness of the material and attempts to control the processing flaw, while the toughening control approach attempts to create microstructures that impart sufficient fracture resistance so that the strength becomes insensitive to the flaw size.

The resistance of brittle materials to crack propagation can be strongly influenced by the microstructure and by adding various reinforcements such as secondary phase particles, whiskers and fibres. It is possible that a material can have more than one toughening mechanism; this thus generates a net toughness larger than that resulting from the separate mechanisms. In multiple mechanism systems the dominant mechanism usually changes as the microstructure varies.

Toughening mechanisms that result in the enhancement of the fracture toughness of ceramic materials can be divided into three basic types shown in Figure 3.3. Each toughening mechanism is described below [39,40,41].

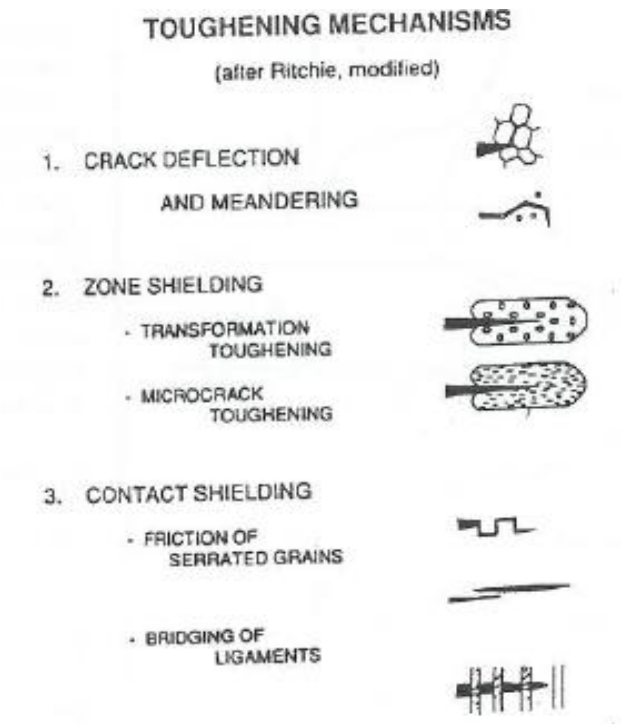

Figure 3. 3: Toughening mechanisms [41].

3.3.1. Crack Deflection

This mechanism of toughening occurs by impeding the growth of the crack by placing obstacles in the crack path thus increasing the toughness of the material. The necessary conditions of crack deflection are that the particles have weak interfaces and high residual stresses between the different phases, so that crack growth occurs along the grain boundaries. These obstacles can include secondary phase particles, whiskers, fibres or platelets. The crack takes the path of least resistance, the obstacles pin the crack thus causing the crack to either bow around the obstacle or deflect out

of the crack plane. The extent of crack deflection does not in general increase with crack length so that long R-curve behaviour and crack tolerance cannot be expected.

PcBN materials are brittle materials and thus fail in a brittle manner with rapid crack propagation throughout a stressed material. The material contains very little plastic deformation before failure and the cracks run perpendicularly to the applied stress. Brittle fracture can be classified into two main groups: transgranular and intergranular fracture. Transgranular fracture is the fracture through the grain of a material. The fracture path changes direction from grain to grain and is sometimes dependent on the orientation of the grain. The crack chooses the path of least resistance. Intergranular fracture occurs when a crack travels along the grain boundaries of the material and usually occurs when the phase between the grains is weak.

3.3.2. Zone Shielding

This toughening mechanism results from shielding the crack tip from applied stress as the crack grows. There are two types of zone shielding toughening effects: transformation toughening and microcrack toughening.

3.3.2.1. Transformation Toughening

Transformation toughening is seen mostly in Zirconia-containing ceramic materials, resulting from a volume increase caused by the phase transformation of zirconia from tetragonal into its monoclinic allotrope. This transformation induces high

compressive stresses in the vicinity of the crack, which prevent the cracks from propagating. PcBN materials do not go through any phase change during cracking, thus they do not experience any transformational toughening.

3.3.2.2. Microcack Toughening

Microcrack formation occurs at the grain boundaries of a material as a result of high residual stresses generated by thermal expansion anisotropy in single phase ceramics or thermal expansion mismatch in multiphase ceramics. Microcracking as a toughening mechanism has not been seen in PcBN materials but microcrack development has been linked to one of the major causes of replacements of cutting tools [(42)].

3.3.3. Contact Shielding

Contact shielding is the shielding of the crack tip by forming a crack closure behind the crack, either by the friction of serrated grains or by the bridging of the crack by ligaments.

3.3.3.1. Crack Bridging

Toughness can be increased by the presence of reinforcing elements that bridge the crack surfaces. Bridging can be both ductile and brittle [(39)]. In ductile bridging as it pertains to metal-toughened ceramics, the ductility and high toughness of the metal ligaments provide the toughening through plastic dissipation. Large local residual

stresses caused by thermal expansion mismatch can suppress local crack propagation, which allows the intact ligament to exist behind the crack front as can be seen in Figure 3.4. Once the ligaments have failed the energy is dissipated as acoustic waves. Figure 3.5 shows a schematic of effects the bridging has on the crack.

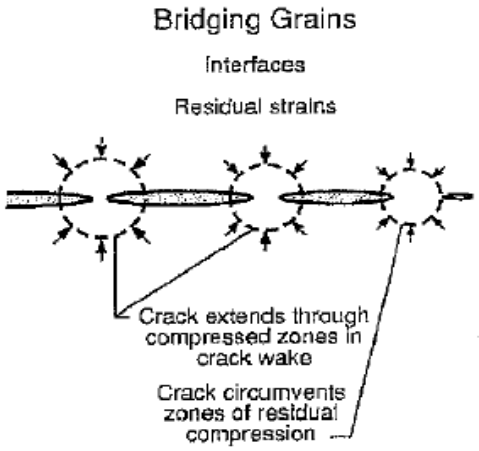

Figure 3. 4: Bridging grains: Ligament formation allowed by residual stress [(39)].

For brittle materials the toughening is more subtle and is similar to non-bridging materials. The bridging requires microstructural residual stress or weak interfaces. The low energy interfaces and/or grain boundaries can cause the crack to deflect along those interfaces, also permitting intact ligaments. As the crack extends, further debonding can occur and eventually the bridges fail either by debonding around the end or fracture. After failure, frictional sliding may occur along the debonded surface.

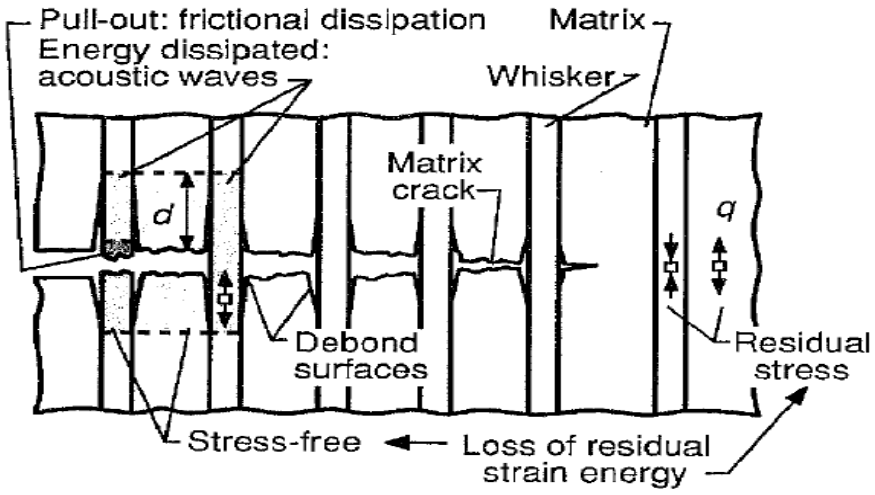

Figure 3. 5: Toughening of material by bridging of crack [39].

3.4. Relationship of the Structure to Properties of the Polycrystalline Cubic Boron Nitride Composites

The relationship of the microstructure of the PCBN composites on mechanical properties is an important aspect in understanding the materials. The effect of the grain size of the cBN particles and the amount of binder phase have on the hardness, fracture toughness and strength of the material will be discussed in this chapter.

The binder chemically reacts with the cBN grains under sintering conditions to form bonds between the cBN grains. The residual binder phase has properties that will affect the properties of the whole composite material. In the PcBN-Al composite system the Aluminium added reacts with the cBN to produce a residual binder phase made up of AlN and AlB_2 as shown in Chapter 2. These residual binder phases are ceramic and thus quite brittle.

In explaining the effects of the microstructure on the mechanical properties of the PcBN materials, there is insufficient information on fracture toughness and strength [2,11]. There is a close relationship between the properties of PcBN and polycrystalline diamond (PCD). The most significant difference between PcBN and PCD materials is the binder phase; in PcBN materials the binder phase is normally ceramic and brittle as in the case of PcBN-Al composites, while the PCD materials contain Co, which is more ductile. As there are much more data on the mechanical properties of PCD materials [43,44,45], the effect of the grain size and binder content on the properties of PCBN will be explained using the corresponding information available for PCD materials. Extrapolation from this body of information into PcBN will be made, as part of an effort to understand the mechanical properties of PcBN materials and to interpret the results obtained in this work.

3.4.1. Hardness

In a study on the hardness of PcBN materials by Hooper and Brookes (1986) [46] they suggested that the highly deformed structure formed through the synthesis of high content cBN materials results in a high level of hardness. Hooper [47] indicated that the hardness of the PcBN materials could be accurately modelled using the rule of mixtures relationship between hardness and cBN content as shown in equation 3.2.

$$H = (1 - f)H_{cBN} + fH_{binder} \qquad \textbf{(3.2)}$$

Where *f* is the volume fraction of the binder phase and H is the hardness.

Since the ultra hard cBN particles are the main contributors to the hardness of the PCBN composite, the size of these particles will affect the hardness of the material. Similarly to other brittle materials, the relationship between the hardness and the grain size of the cBN grains can be approximated by the Hall-Petch equation shown below. This relationship shows that the hardness is inversely proportional to the square root of the grain size (d) [48].

$$H \propto \frac{1}{\sqrt{d}} \qquad (3.3)$$

Thus the hardness increases with the decreasing particle size of the cBN grains. This occurs because the smaller the grain size, the higher the applied stress needed to cause dislocation movement through the material. With a coarse grained material a lower stress is needed to move dislocations, therefore reducing the hardness of the material as more plastic flow can occur.

Rice (1994) **[48]** reported conflicting trends in literature where for some materials of large grain sizes the hardness decreases with decreasing grain size. In a study on the hardness-grain size relationships in ceramics Rice **[48]** tested the two trends, concluding that the confusion was due to lack of sufficient data to properly cover the two trends. Of the two conflicting trends, the first was the normal inverse trend of hardness with grain size ($H \propto G^{-1/2}$) applied to finer grain sizes (1 – 50 μm). The second trend was for a minimum hardness value occurring at intermediate grain sizes (20 – 50 μm) (where cracking or spalling occur along grain boundaries) and also for

hardness increases towards single crystal values for large grain sizes (>50 μm). Table 3.1 shows variations in hardness with grain size for some ceramic materials.

The Hall-Petch relationship can only be used as a guideline in determining the grain size effect on the hardness of cBN materials as it was developed for single phase materials. Since PcBN materials consist of two phases the effect of the binder phase can change the relationship between the hardness and the grain size. Thus the effect of the binder phase needs to be looked at.

Table 3. 1: Changes in Hardness with grain size of ceramics [48].

	Hardness (GPa) (100g load)			**% Change**	
	2 μm	**50 μm**	**100 μm**	**(2 -50 μm)**	**(50-100 μm)**
Al_2O_3*	24.7	23.5	23	4.8%	2.1%
B_4C**	-	37	36.5	-	1.4%
SiC*	-	34.5	34	-	1.5%
Si_3N_4*	17.5	21	-	- 20%	-

*H_V (100g load) **H_K (100g load)

Both the composition of binder material and the amount of binder will affect the hardness of the composite material. The binder phase is usually a softer material than the ultra-hard cBN phase and thus will decrease the hardness of the composite material. Low binder content leads to more contact between the cBN grains, generating high stresses in the material structure due to the ultra high pressures used for sintering, thus increasing the hardness of the material. Increasing the binder content causes a decrease in the hardness due to the decrease in the harder grain

abating against each other and a decrease in the flow stress (see Figure 2.3, Chapter 2).

3.4.2. Fracture Toughness

The resistance to crack propagation plays an important role in understanding a material's behaviour and enhancing application limits. The fracture toughness and toughening mechanisms are important in understanding the material. As stated previously there is very little data on the mechanical properties of PcBN materials [2,11]. Thus some of the trends for fracture toughness will be discussed using PCD adapted to PcBN materials.

Studies by Lammer (1988) [43] and later Meiss (1996) [44] investigated the changes of fracture toughness of PCD materials with diamond grain size. The technique used to determine the fracture toughness was the diametral compression test or Brazilian disk test. In this study, the fracture toughness increased with increasing grain size to a maximum value and then remained constant (2 – 6 $MPa.m^{0.5}$). Figure 3.6 shows the fracture toughness as a function of the average grain size of the diamond grains for Miess' [44] work. He explained this trend on the basis of the work of Rice [48,49] on the changes of fracture energy with differences in thermal expansion coefficients between the primary and secondary phases, which cause microcracking to occur and propagate at the interface. Microcracking has not however been seen in PcBN materials and thus is unlikely to cause toughening.

Huang (1997) [45] also did a study on the fracture toughness of PCD materials; in this study the fracture toughness was measured using a modified single-edge-precracked beam method test. The investigation also showed that the fracture toughness increased with the increasing grain size of the diamond particles.

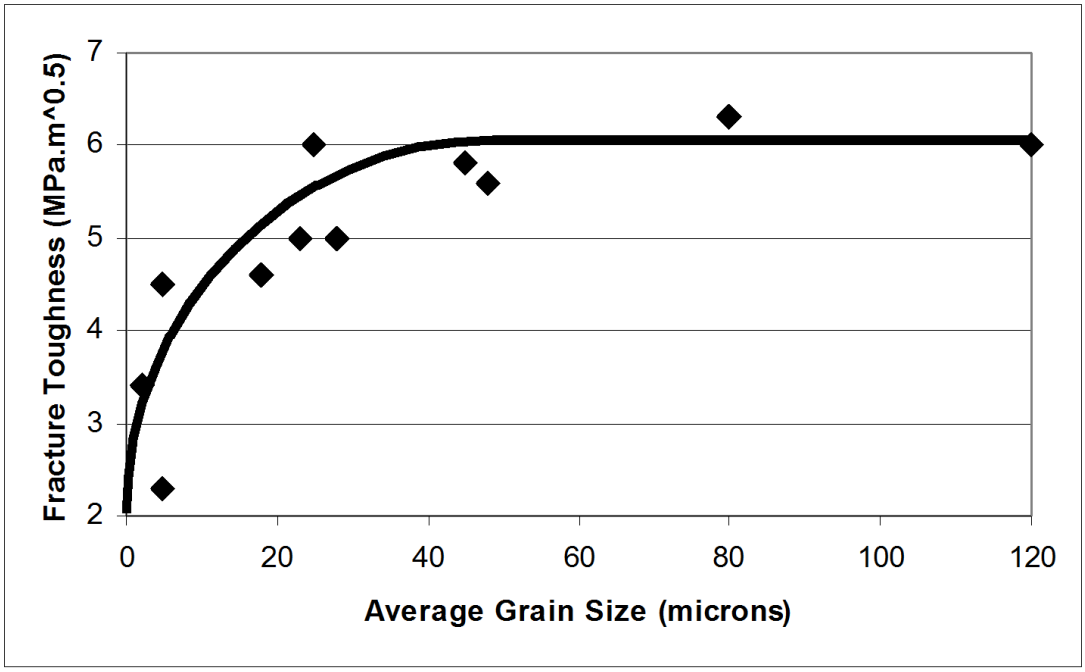

Figure 3. 6: Fracture toughness as a function of the average grain size of diamond for PCD materials with Co-binder [44].

Rice et al (1979) [49] reported that the fracture toughness of polycrystalline ceramic depended on the grain size, i.e. fracture toughness increasing with the particle size of the hard phase. It was suggested that the internal stresses that existed between the components due to different thermal expansions resulted in local tensile and compressive stresses. The stresses near flaws or along the applied stress resulted in failure by adding to the applied stress. Rice et al [49] suggested that the contribution of

the internal stresses to failure increased with decreasing grain size. Other factors such as impurities in the matrix material, the size and amount of the secondary phase and deformation of the grains during synthesis could also have affected the fracture toughness of the material.

As described in section 3.3 the most likely toughening mechanisms to occur in PcBN materials are crack deflection, grain bridging and to lesser extent crack bridging due to residual Al metal left after sintering. As PcBN materials are phases made up from man with hard cBN grains surrounded by one or more ceramic binder phases, these cBN grains will act as obstacles to crack propagation and thus cause a certain amount of toughening in the material. Crack propagation is generally affected by the residual stresses in the material. In a multi-phase material such as PcBN the differences in the thermal expansion cause residual stresses between the different phases. This will likely affect crack propagation. The magnitude of residual stresses and their local distribution is determined by the volume fraction of the ceramic phases.

Estimation of the internal stresses formed in the material by thermal expansion mismatch of the various phases is given in equation 3.4 **(50)**. The internal stresses are modelled for the ceramic binder phase.

$$\sigma_r = -\beta\left(\frac{R}{r}\right)^3 ; \quad \sigma_t = \frac{\beta}{2}\left(\frac{R}{r}\right)^3 \qquad \textit{where} \quad \beta = \frac{(\alpha_m - \alpha_p)\Delta T}{\left(\frac{1+\nu_m}{2E_m}\right) + \left(\frac{1-2\nu_p}{E_p}\right)} \quad (3.4)$$

Where σ_r and σ_t are the radial and tangential stresses, the tangential stress is half the radial stress. E_m, ν_m and E_p, ν_p are the Young's modulus and Poisson's ratio for the matrix (cBN) and secondary phase (AlN). R and r are the secondary phase particle size and the distance from the centre of the particle, at the interface of the phases R = r. Poisson's ratio for cBN and AlN is 0.2 **(51)** and 0.22 **(52)** respectively. The result from equation 3.4 gives the radial stress as 442 MPa and the tangential stress as – 221 MPa. A residual radial matrix compressive stress is generated around the AlN phase, as the thermal expansion of the AlN is higher than the matrix phase. The compressive stresses can prevent or reduce intergranular cracking and crack propagation.

The binder phase also affects the fracture toughness and acts typically as a crack blunting. A more ductile binder phase can increase the blunting effect on the crack. The higher the content of the binder phases the greater the effect on fracture toughness, which should increase with increasing binder content.

3.4.3. Transverse Rupture Strength

The strength of a material is important as it indicates the material's ability to resist a force and thus the strength at which a material will fail. As stated previously there is limited data on the mechanical properties of PcBN materials **(2,11)**. Thus some of the trends for the strength will be discussed using PCD and adapted to PcBN materials.

A study by Lammer [43] on the mechanical properties of PCD materials showed that strength decreased with increasing grain size for PCD materials as can be seen in Figure 3.7. He explained this trend according to two models, the first using the classical Griffith-Orowan strength relationship shown in equation 3.5, the second using the Hall-Petch strength relationship shown in equation 3.6. The Griffith-Orowan relationship shows that the largest grain size had the most severe flaw, which leads to failure, with a failure mechanism caused by the propagation of cracks originating in these existing flaws. Although this was applied to an ideal material, in reality there were pores in the material, which were larger than the grain size and could have resulted in the most severe flaws. In the second model the Hall-Petch strength relationship was used for smaller grain size materials and the mechanism was based on the microplastic flow or dislocation movement which leads to crack initiation, propagation and then failure. Microplastic flow did not occur in the cBN material since the binder was brittle, so a different mechanism needed to be proposed for PcBN materials. Since the flaw size was equivalent to the particle size due to flaws introduced during the machining process, Figure 3.7 should be redrawn with respect to $1/\sqrt{d}$, as shown in Figure 3.8, where region 1 and 2 are represented by equations 3.5 and 3.6 respectively.

Griffith-Orowan Strength relationship (Region 1):

$$\sigma_f = K_1 / \sqrt{d} \qquad (3.5)$$

Where σ_f is the fracture strength, K_1 a constant and d the average grain size.

Hall-Petch Strength relationship (Region 2):

$$\sigma_f = \sigma_O + K_2 / \sqrt{d} \qquad (3.6)$$

Where σ_f is the fracture strength; σ_O the material constant for the starting strength due to dislocation movement, K_2 the constant (strength coefficient) and d the mean grain size.

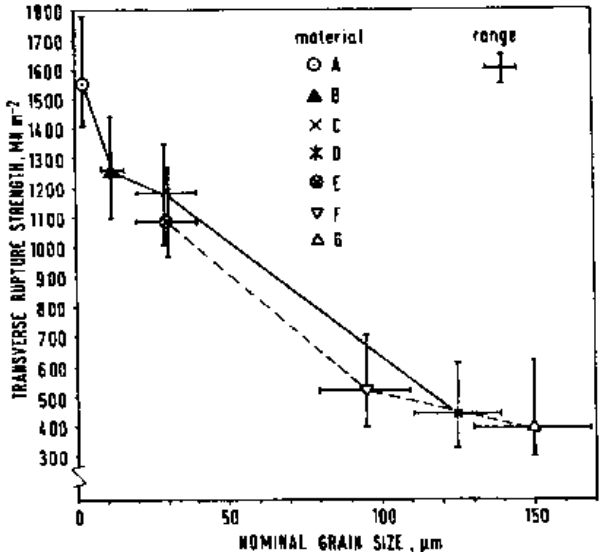

Figure 3. 7: Transverse rupture strength as a function of the nominal grain size of diamond for PCD materials [(43)].

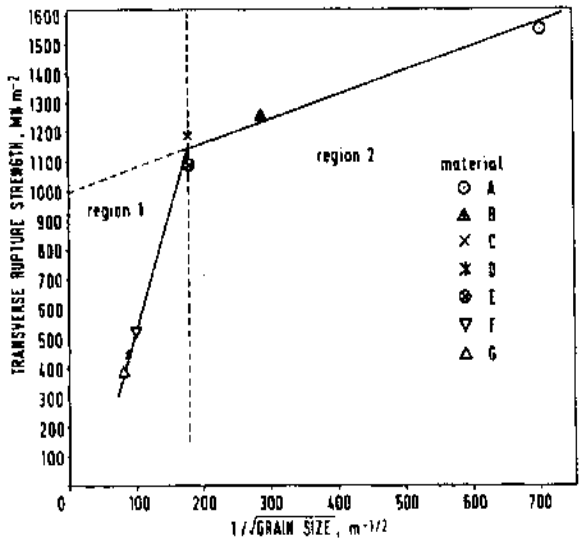

Figure 3. 8: Strength as a function of the grain size relationship for PCD materials [43].

Rice [48] also suggested that the bimodal behaviour of the curve of TRS versus grain size was more likely to be due to the grain size d versus crack size c relationship. He showed that in ceramic materials the inherent flaw introduced by machining and surface finishing procedures were independent of grain size. The surface flaw resulted in a sharp strength reduction in the brittle region [45]. Rice suggested that the fracture strength σ_f of fine grain size materials was controlled by the polycrystalline surface energy, while for coarse-grained materials the fracture strength was controlled by the single crystal crack surface energy or the size of the defects since the flaw is contained within a single grain. Therefore, when the critical stress intensity factor corresponding to the single crystal was reached, the crack propagated and would lead to failure. According to this theory, the transition grain size occurred at $c \approx d$. From experimental measurements Lammer [43] calculated that for PCD materials the critical ratio of $c/d = 1$ should be reached between 12 and 30 µm. This can be seen in Figure

3.8, the two lines intersect where the flaw size is equivalent to the particle size, approximately 30 μm. Lammer [43] also showed that the fracture mode of the coarse grained areas (≥30 μm) was transgranular while the fine grained areas (≤ 30 μm) was microplastic flow and microcracking where dislocations lead to crack nucleation.

The strength of cBN materials appears to increase with the decreasing grain size of the cBN particles. However, strength is also affected by the largest flaw in the material. Large flaws can form due to agglomerated particles, either as cBN particles sticking to each other or the binder materials can act as defects in the microstructure. These defects are fracture initiation sites, which can lead to the lowering of the strength of the material. It is thus important to have good mixing techniques to produce uniform distributions of all the phases throughout the composite material [53, 54].

The strength of the material is also affected by the binder phase; higher binder phase content will increase the chances for flaws to be present in the material and thus increase the risk of premature failure. Lammer [43] suggested that the strength of PCD materials depended also on the amount of secondary phase, cobalt. The strength increases with increasing secondary phase content.

Consequently there is a weigh-up with the mechanical properties dependence on grain size and binder content. Large grain sizes are favoured when fracture toughness is the

critical property, while materials with smaller grain sizes are used where hardness and strength are the most important properties. Low binder content is favoured for materials that require high hardness and medium strength. Thus a balance must be reached depending on application. The dominating effect controlling the mechanical properties needs to be determined as well as the influence of binder content. All these aspects will be analyzed in subsequent chapters.

Chapter 4: Experimental Procedure

This chapter describes in detail the experimental procedures used in the making, characterisation and mechanical testing for PCBN-Al composite materials. A detailed description of all the equipment used for making, characterisation and mechanical testing is also provided in this chapter. The starting powders, mixing procedures and powder characterisation are also described in this chapter.

4.1. Starting Materials

All the powders used in this study are given in Table 4.1. The average particle size and manufacturing company are also provided.

Table 4. 1: Powders used for processing.

Material:	**Particle Size, d_{50} (μm)**	**Company**
Grade M2-4 cBN powder	2.45	Element Six (Pty) Ltd
Grade 2 cBN powder	1	Element Six (Pty) Ltd
Grade 4 cBN powder	6.37	Element Six (Pty) Ltd
Grade 9 cBN powder	14.5	Element Six (Pty) Ltd
Grade M20-40 cBN powder	14.75	Element Six (Pty) Ltd
Aluminium powder	4.2	Saarchem

The starting materials used for this work were crushed cBN powders grades 2, M2-4, 4, 9 and M20-40 (average particle size ranges from: 1 – 40 μm) in various grade size

combinations and Aluminium powder (average particle size: 1 – 4 μm). The Aluminium powder was wet sieved before use to remove all large particles (section 4.2.1).

The powders were analysed using a scanning electron microscope (SEM) to determine the morphology of the particles. The SEM images of the various cBN grades and the Aluminium powder are shown in Figure 4.1. The images show that the cBN grains are facetted and the Aluminium powder consists of spherical particles.

A Malvern Mastersizer 2000 (Section 4.3) was used to measure the particle size and particle size distribution of the powders. Figure 4.2 shows the particle size distribution of the cBN powders. d (10), d(50) and d(90) means that 10, 50 and 90% of the particles are less than the particle size indicated.

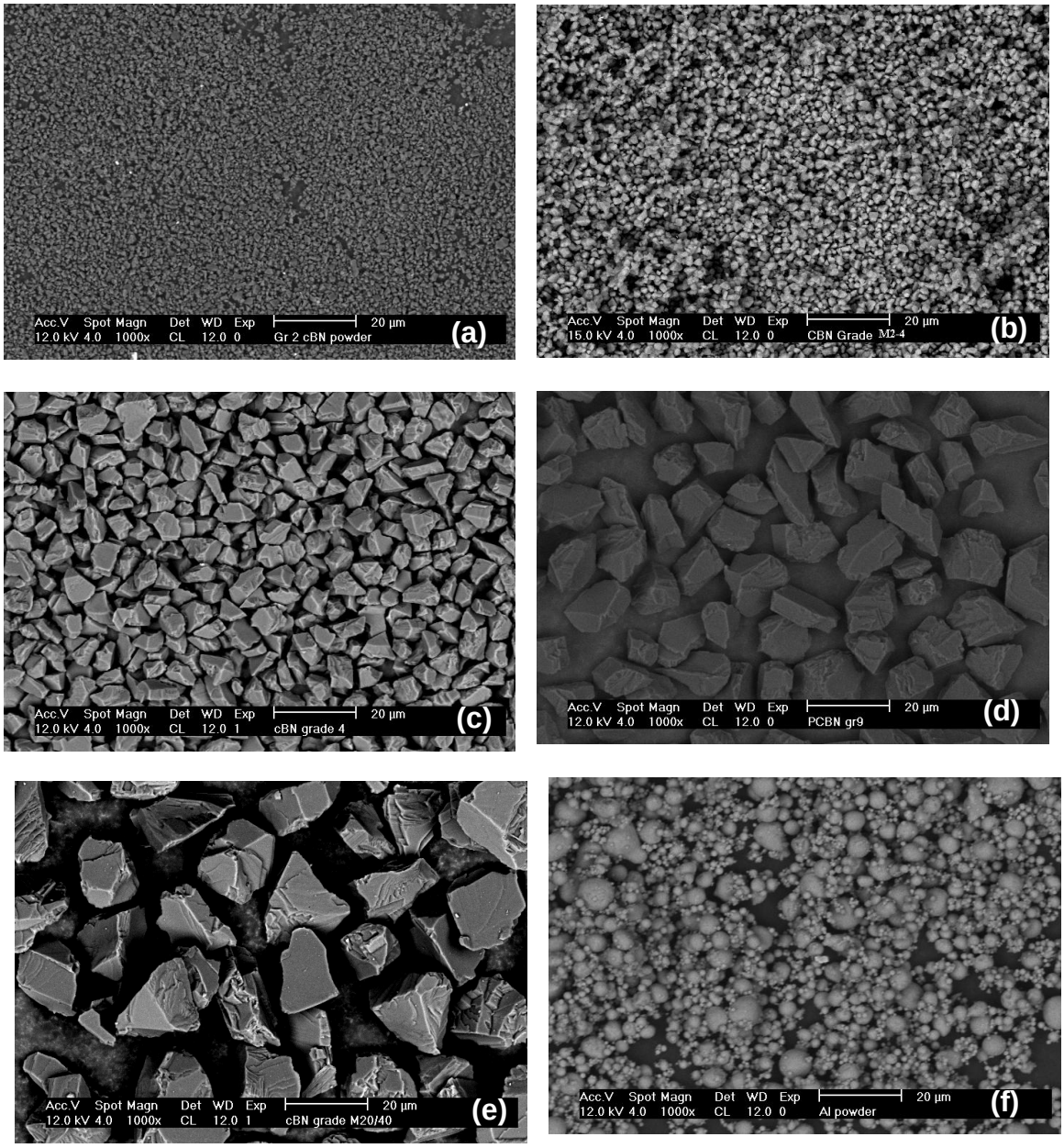

Figure 4. 1: SEM micrographs of the cBN and Aluminium powders used in the PcBN-Al composite; a) grade 2 cBN powder; b) grade M2-4 cBN powder; c) grade 4 cBN powder; d) grade 9 cBN powder; e) grade M20-40 cBN powder and f) Aluminium powder.

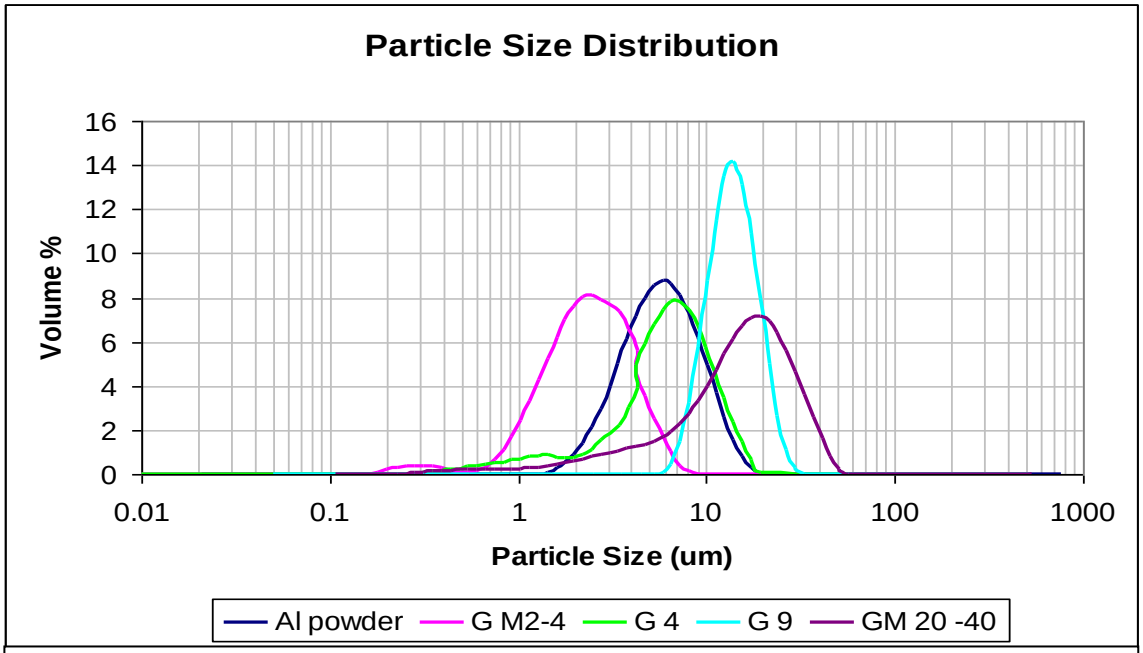

Aluminium: d(10) = 2.9 µm d(50) = 4.2 µm d(90)= 10.5 µm
G M2-4: d(10) =1.12 µm d(50) = 2.45 µm d(90)= 4.65 µm
G 4: : d(10) = 1.28 µm d(50) = 6.37 µm d(90)= 11.7 µm
G 9: : d(10) = 9.9 µm d(50) = 14.5 µm d(90)= 21.25 µm
G M20-40: d(10) = 4.07 µm d(50) = 14.75 µm d(90)= 29.0 µm

Figure 4. 2: Particle size distribution of the cBN and Aluminium original powders used in the PcBN-Al composites.

4.2. Experimental Equipment for Powder Processing

4.2.1. Wet Sieving of Aluminium Powder

The Aluminium powder was wet sieved before use, to remove any particles that were larger than 4µm. Wet sieving was done by mixing small amounts of the Aluminium powder (20 g) with hexane (C_6H_{14}) and placing the mixture in a container with a filter cloth. The filter cloth had an aperture of 4µm to allow all the fine particles to pass through and retain the larger particles. The mixture was then mixed using a rotating

stirrer to assist the movement of particles through the filter cloth. After 1 hour of stirring, the mixture was drained into a container; extra amounts of hexane were added to the container to wash the fine particles through the aperture. The fine particle slurry was then dried in a rotary evaporator. The filter cake on the filter cloth was dried and placed into a container. Figure 4.3 illustrates the apparatus used for wet sieving the Al powder.

A rotary evaporator was used to evaporate the solvent (hexane). The hexane gas was re-condensed and the liquid hexane captured in a flask. The temperature and pressure of evaporation were 40°C and 335 mbars respectively. Figure 4.4 shows an image of a rotary evaporator.

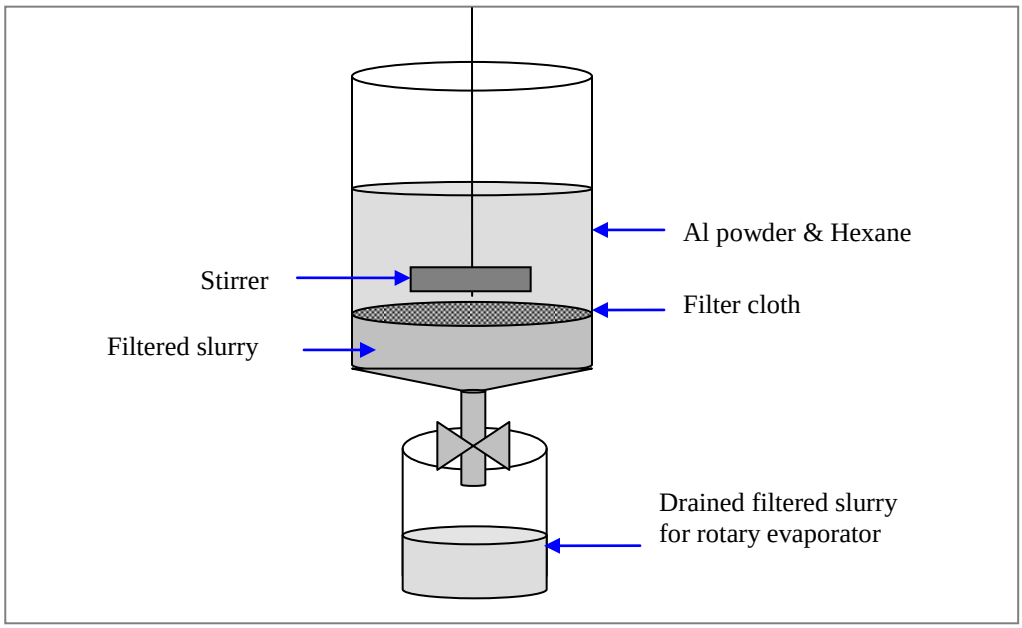

Figure 4. 3: Wet sieving apparatus

Figure 4. 4: Image of a rotary evaporator.

4.2.2. Turbula Mixer

A turbula mixer was used to assist in the mixing of the dry powders. This was done to prepare the powders for sintering. The powders were weighed into their correct proportions and placed into a plastic container. 10 mm stainless steel balls were used as milling media to aid in the mixing and breaking up of agglomerates in the powders. The number of balls depended on the amount of powder that was being made (8 steel balls were used for 30 g of powder). The mixing time was 1 hour. After mixing, the steel balls were removed and cleaned and the mixed powder was decanted into a labelled storage container and placed in a vacuum chamber set at 20°C to prevent oxidation and moisture from affecting the powders. The powders were kept in the vacuum chamber until use.

4.2.3. Uniaxial Pressing

After the powders had been mixed and placed in to the vacuum oven overnight, the powders were then used for sintering. The powders were placed into the required 50 mm diameter metal containers used in the sintering process. The powders were then uniaxially pressed using a 50 MPa pressure into smooth surfaced compacted powder disks. The containers were then closed with a metal lid and sealed with a metal wire.

4.2.4. Vacuum Degassing

The sealed compact containers were then placed in a Torvac vacuum furnace for outgassing and subsequent sealing. The vacuum heat treatment is used to remove all absorbed gases and surface impurities from the powders so as to prevent oxidisation during sintering. After the outgassing stage the containers are heated to a higher temperature to melt the sealing metal wire to seal them from the outside environment. The process of vacuum degassing and sealing takes 10 hours.

4.2.5. High Temperature High Pressure Sintering

After the compacts had been outgassed and sealed, the compacts were then prepared for sintering. The compacts were placed into the required containers used for sintering (the exact procedure and type of sintering containers used in the sintering process are classified by Element Six (Pty) Ltd and thus cannot be divulged).

Sintering was done at high pressure high temperature (HPHT) to facilitate full densification. HPHT belt apparatus was used. This operation was carried out at the pressing facilities at Element Six (Pty) Ltd in Springs, South Africa. The sintering process is information proprietary to Element Six (Pty) Ltd and thus most aspects of this process cannot be divulged. The sintering profile consisted of first by applying pressure and then heating the material to sinter and form fully densified compacts. The approximate temperature of sintering was 1400°C. Figure 4.5 shows the sintering powder and load profile. After sintering the sintered disks were removed and taken for surface processing. The metal container surrounding the sintered PcBN disk was removed by surface and OD grinding (outer diameter) of the PcBN disk.

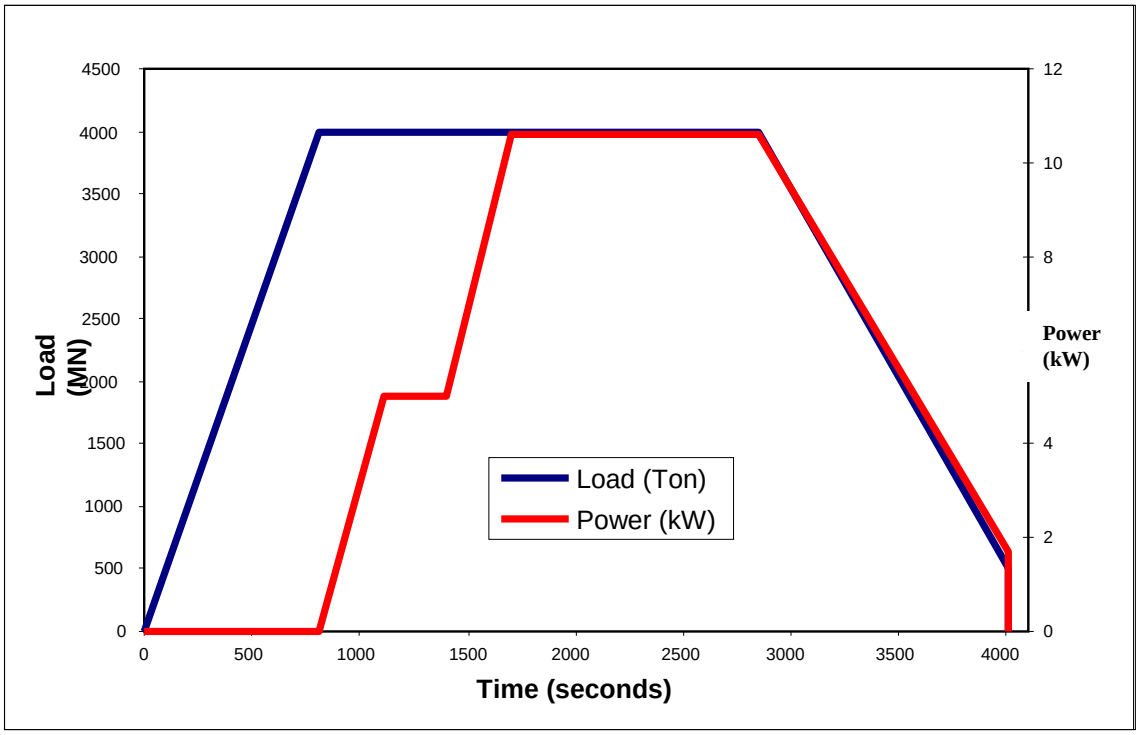

Figure 4. 5: Load and power profile used to sinter the PcBN-Al composites.

4.2.6. Lapping, Surface and OD Grinding Machines

Lapping and surface grinding of the sintered compacts were done to remove the outside metal container and to machine the components to the correct dimensions and surface quality for testing. The sample disks were first taken to the surface grinding machine to remove the metal container on the flat surfaces of the disk. Then the disk was taken to the OD (outer diameter) grinding machine to remove the metal container on the circumference of the disk.

After the metal container had been removed from the disks, the PcBN disks were lapped in two stages; the first stage was aimed at grinding to the correct disk thickness and the second to prepare the correct surface quality. The first stage of lapping was done using a coarse lapping grit of 120-grit size; this was done for about 1 – 2 hours to reduce the thickness of the disks to approximately 3.2 mm. The samples were then fine lapped using a fine lapping grit of 300-grit size to further reduce the thickness to 3 mm and to make sure that the surface contained no visible scratches and had a smooth surface quality.

4.2.7. Laser Cutting

Test samples were cut to the required dimensions for each of the mechanical tests, using laser cutting. The sample dimensions were 25 x 4 x 3 mm for fracture toughness and strength bend bars. Figure 4.6 shows the arrangement of the bend bars

laser cut-out of the PcBN disks, with 8 samples being cut out per disk. 4 disks per material were sintered for the bend bar samples, and a total of 28 samples were cut out; 20 for TRS and 5 for SEVNB with the rest used for testing.

The compact tension samples measured 36 x 33.5 x 3 mm and hardness samples 10 x 10 x 3 mm. Figure 4.7 shows the arrangement of the CT samples laser cut-out of each PCBN disk, 1 sample being cut out for each disk. 2 PcBN disks per material were sintered for the CT samples. The laser cut samples had a heat affected zone due to the high temperatures of the laser, thus the samples needed to undergo lapping in order to remove the heat affected zone.

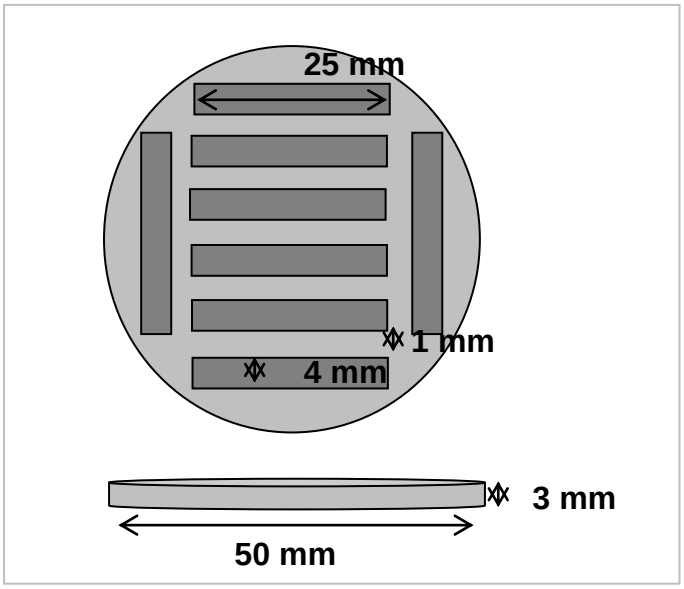

Figure 4. 6: Laser cutting of bend bars from PcBN sintered disk.

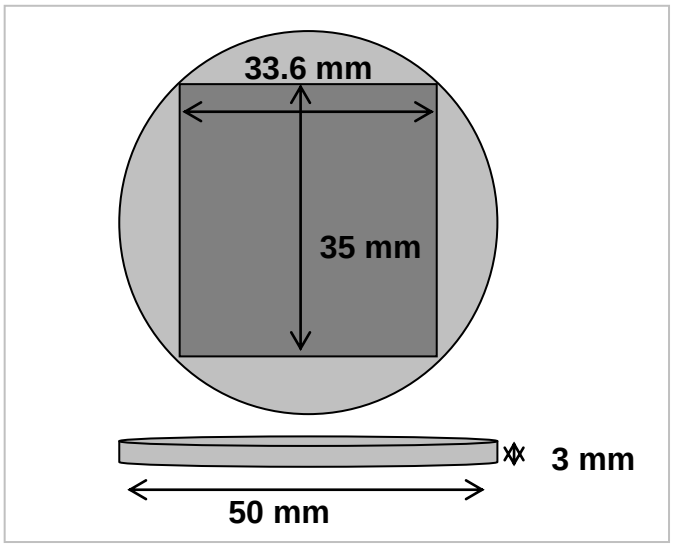

Figure 4. 7: Laser cutting of compact tension (CT) samples from PcBN sintered disk.

After laser cutting of the samples the bend bars were fine lapped again to remove any residual heat affected zone left from the laser cutting and to straighten out the edges of the bars. The lapping was done using a 120 mesh size.

4.2.8. Polishing Equipment

The samples prepared for SEM analysis and hardness testing needed to be polished. The polished PcBN discs were prepared by lapping a cut surface flat and then presenting the flat surface to a diamond scaife wheel. Speeds, loading conditions and details regarding the operation of the scaife wheels for the polishing process are information proprietary to Element Six (Pty) Ltd.

4.3. Powder Processing Procedure

4.3.1. Preparation of cBN Powders

The various cBN powders used in this work were mixed together to form multimodal powders. This was done in order to facilitate particle packing and to prevent the larger grains from breaking during sintering on application of pressure. The process of mixing is described in section 4.2.2. Table 4.2 shows the composition of the mixed cBN powders, where G2, G6, G10 and G20 are the names of the mixed multimodal cBN powders used for the sample materials.

Table 4. 2: Composition of the mixed cBN powders.

cBN powders:	Particle Size (µm)	Composition:	Average Grain Size (µm)
G 2	Bi-modal ~ 2 µm	100 % grade M2-4	2.45
G 6	Multi-modal with 10 µm as the largest size	80 % grade 4 20 % grade 2	5.96
G 10	Multi-modal with 20 µm as largest particle size	80 % grade 9 20 % grade 2	11.8
G 20	Multi-modal with < 20 µm as largest particle size	75 % grade M20/40 10 % grade 4 15 % grade 2	16.19
Aluminium powder, 99.9% pure	4.2 µm		4.2

The powders were mixed in a turbula mixer for 30 minutes; Figure 4.8 shows the mixed cBN powders. The particle size and particle size distribution of these powders were measured using the Malvern Mastersizer 2000 particle size analyser. Figure 4.9 shows the particle size distribution, d10, d50 and d90 of the mixed powders. The multimodality of the G6, G10 and G20 cBN mixed powders is evident in the double peaks. The average particle size of the G6 and G10 mixed powders decreased from the original cBN grade powder due to the high amount (20%) of fine grade 2 cBN powder added. The G20 mixed cBN powder showed an increase in the average particle size due to the addition of the grade 4 cBN powder. This could also be attributed to breakage of the larger particles during mixing.

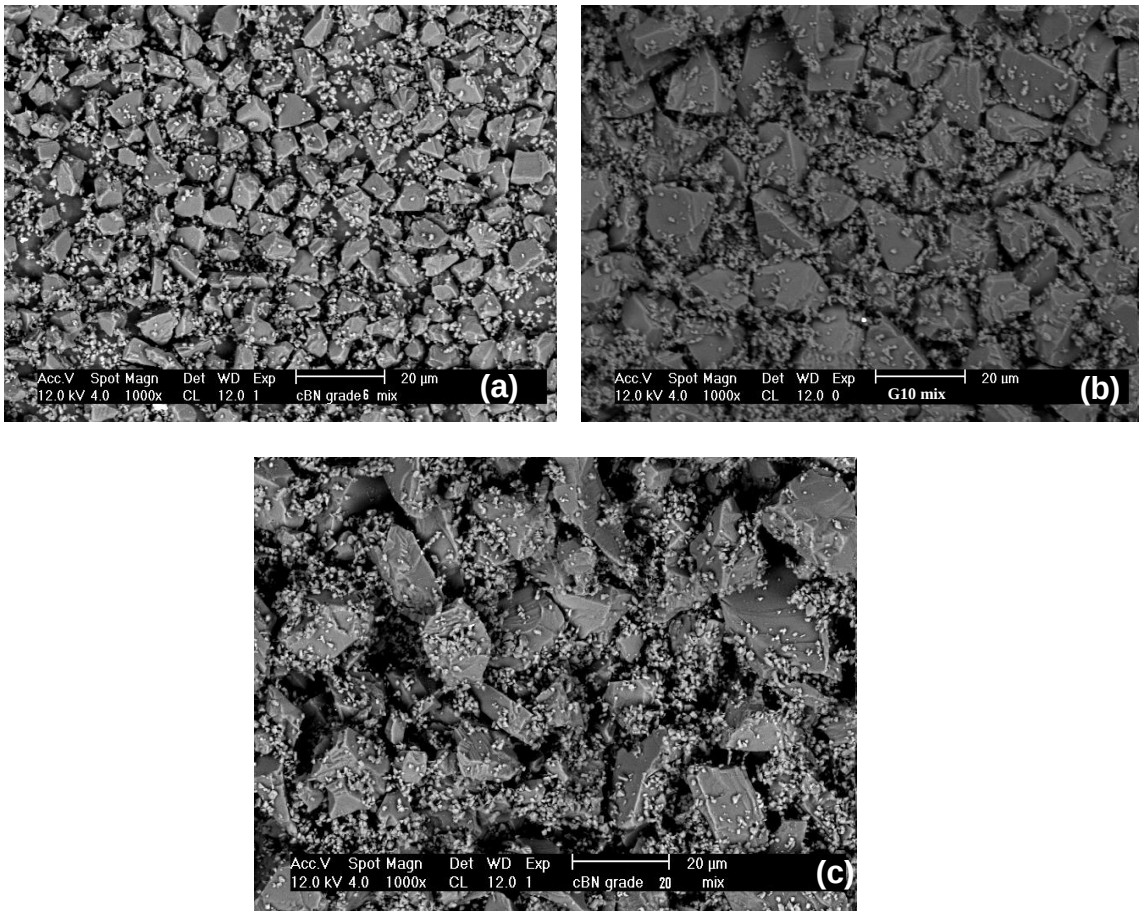

Figure 4. 8: SEM images of the mixed cBN powders; a) G6 cBN powder; b) G10 cBN powder and c) G20 cBN powder.

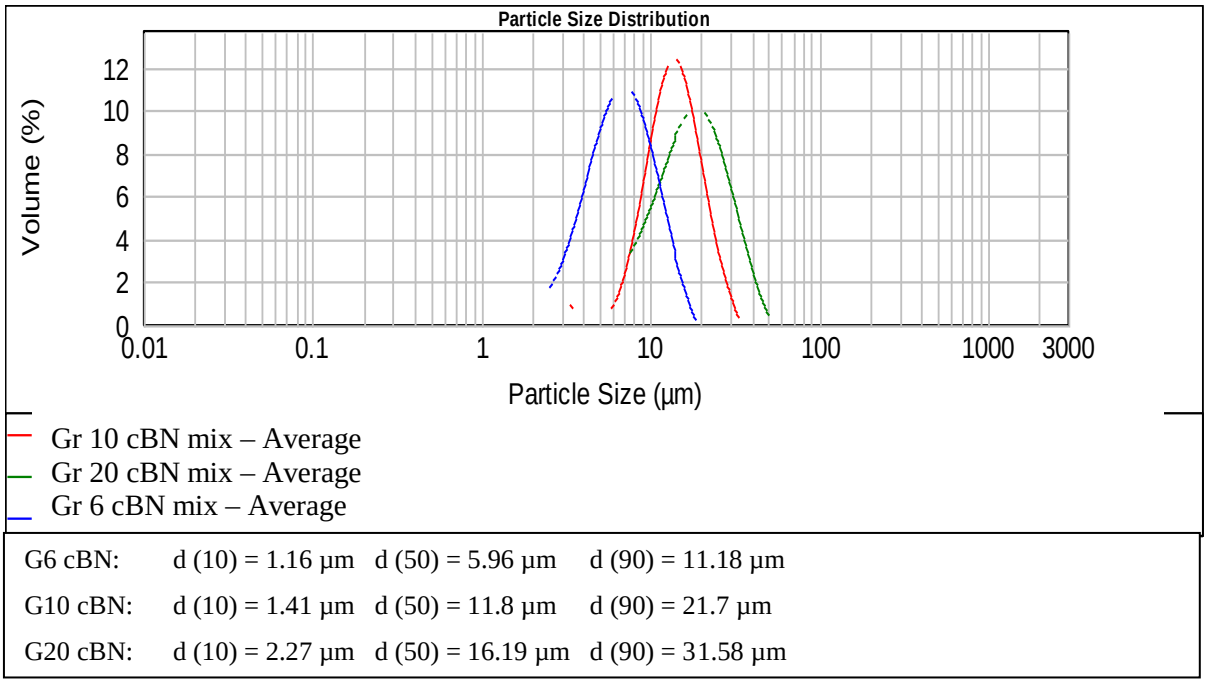

Figure 4. 9: Particle size distribution of the mixed cBN powders.

4.3.2. Preparation of the cBN-Al Powders

The 10 materials prepared for this study are given in Table 4.3. The samples were prepared in various cBN grade sizes and volume percentages of the Al binder phase. The names of the produced samples consisted in the name of the multimodal powders used, shown in Table 4.2, followed by the volume percentage of Al added.

The various cBN powders were mixed with the correct amount of Al to give a 15, 20 and 25 vol. % of Al. Table 4.4 shows the composition of the mixed cBN-Al powders used for the cBN-Al composites.

Table 4. 3: Sample materials.

Sample	G2	G6	G10	G20
Average grain size (µm) of cBN	**2.45**	**5.96**	**11.8**	**16.2**
Vol. % of Al binder phase				
15	X	X	X	X
20	X	X		X
25	X	X		X

Figure 4.10 – 4.11 shows the SEM images of the mixed cBN-Al powders of the different cBN grades. The white Aluminium particles were homogeneously distributed throughout the cBN powder. Some of the Aluminium powder particles were not spherical but slightly elongated. Although the Aluminium powder was wet sieved it can be seen from the figures that the process was not completely efficient as there were still some Al particles larger than 4 µm.

Table 4. 4: Composition of the mixed cBN-Al composite powders

Material	Super Hard Phase cBN			Binder Phase Al	
	Grade	Mass %	Volume %	Mass %	Volume %
G2 + 15% Al	M2-4	87.87	85	12.13	15
G2 + 20% Al	M2-4	83.64	80	16.36	20
G2 + 15% Al	M2-4	79.31	75	20.69	25
G6 + 15% Al	G2	17.57	17	12.13	15
	G4	70.29	68		
G6 + 20% Al	G2	16.73	16	16.36	20
	G4	66.91	64		
G6 + 25% Al	G2	15.86	15	20.69	25
	G4	63.45	60		
G10 + 15%Al	G2	17.57	17	12.13	15
	G9	70.29	68		
G 20 + 15% Al	G2	13.18	12.75	12.13	15
	G4	8.79	8.5		
	M20-40	65.9	63.75		
G 20 + 20% Al	G2	12.55	12	16.36	20
	G4	8.36	8		
	M20-40	62.73	60		
G 20 + 25% Al	G2	11.9	11.25	20.69	25
	G4	7.93	7.5		
	M20-40	59.48	56.25		

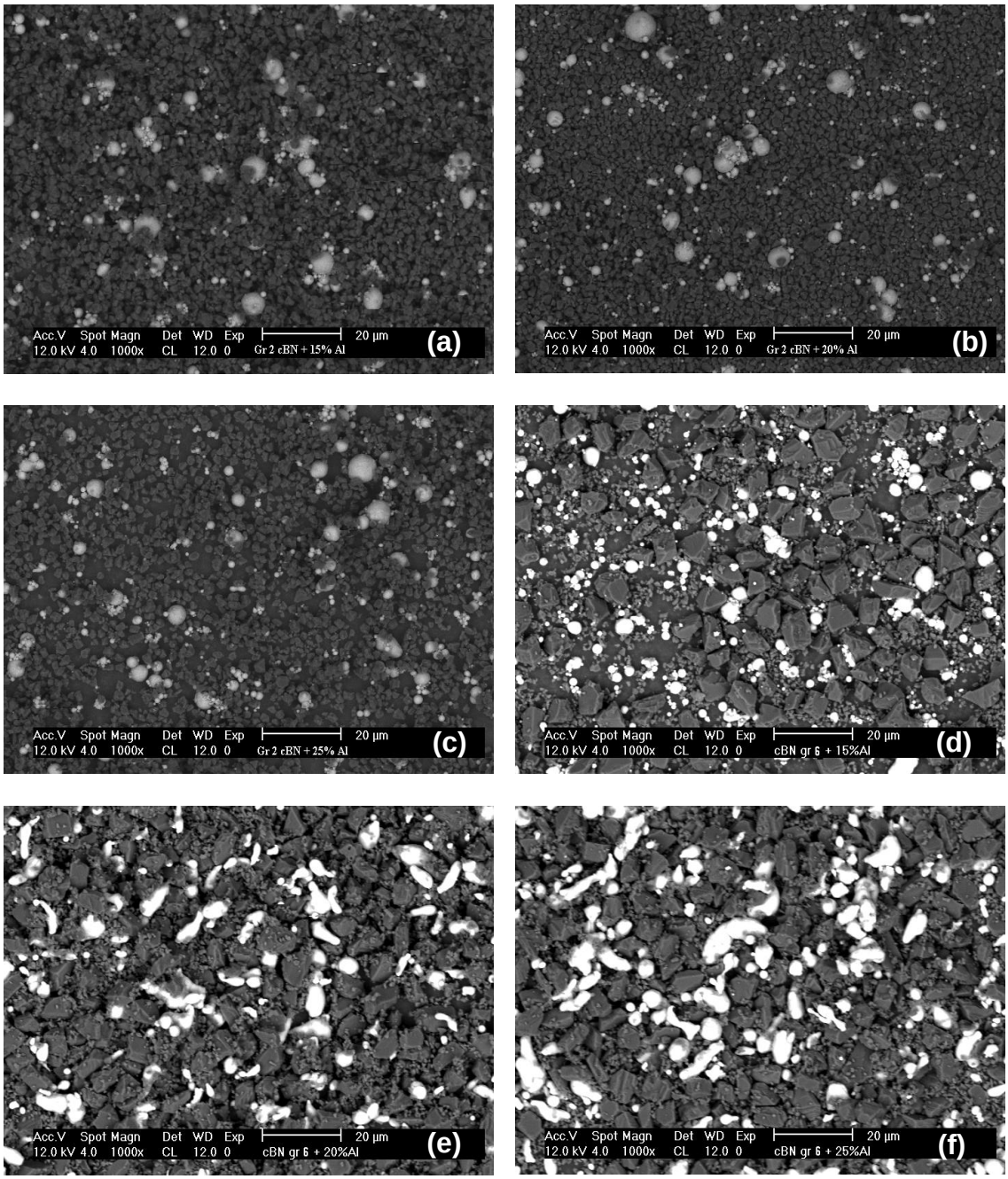

Figure 4. 10: SEM image of the grade G2 cBN-Al mixed powders; a) G2 cBN + 15 vol. % Al powder; b) G2 cBN + 20 vol. % Al powder; c) G2 cBN + 25 vol. % Al powder; d) G6 cBN + 15 vol. % Al powder; e) G6 cBN + 20 vol. % Al powder and f) G6 cBN + 25 vol. % Al powder.

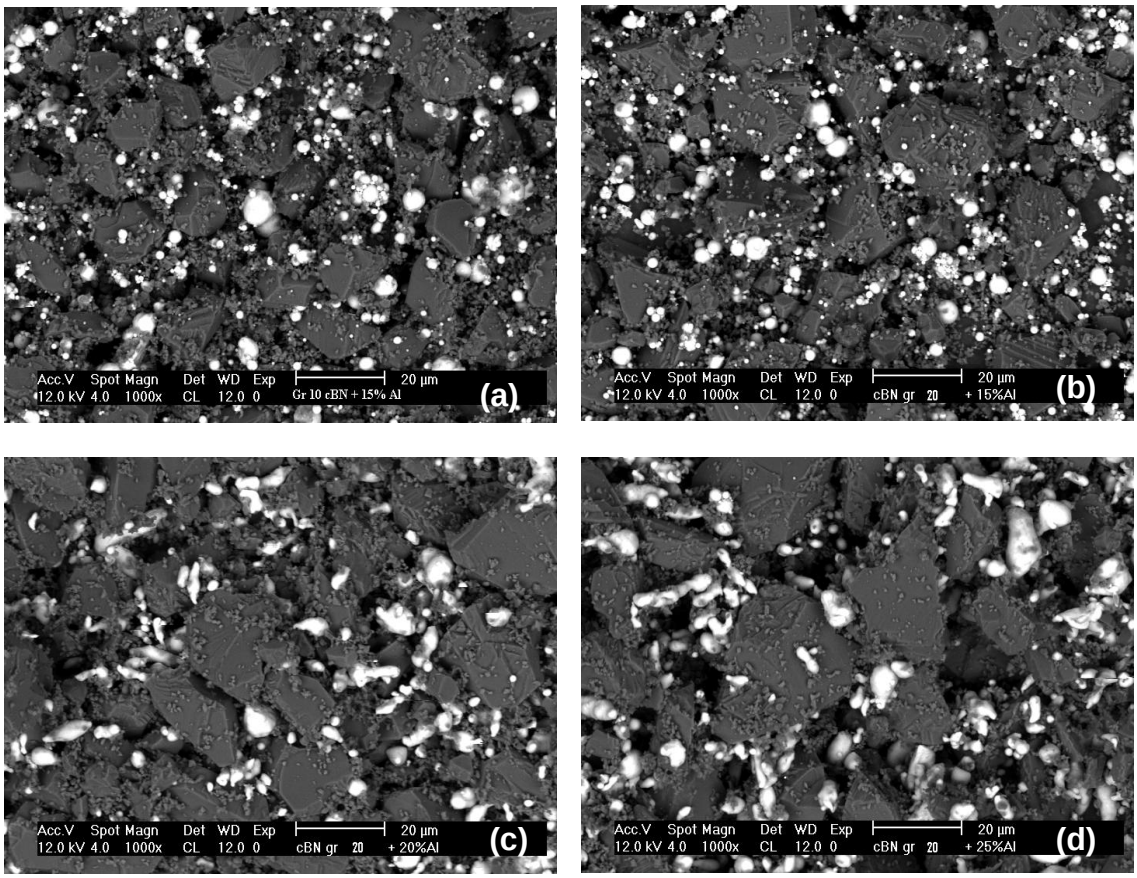

Figure 4. 11: SEM image of the G10 and G20 cBN-Al mixed powders; a) G10 + 15 vol. % Al powder; b) G20 cBN + 15 vol. % Al powder; c) G20 cBN + 20 vol. % Al powder and d) G20 cBN + 25 vol. % Al powder.

4.4. Characterisation and Analysis

4.4.1. Malvern Particle Size Analysis

The Malvern Mastersizer 2000 Particle Size Analyser (PSA) was used to determine the particle size distribution of all powders, raw and mixed, before use. The powders were suspended in a mixture of water and a dispersant (Sodium hexametaphosphate,

$(NaPO_3)_6$). A small amount of the suspended solution was poured into the PSA analysis tank where an ultrasonic probe was used to disperse the particles into the water. The PSA measures the light intensity as a function of the scattering angle of the suspended solution and determined the particle size and particle size distribution of the suspended powder particles. The particle size analysis of each powder was performed at least 3 times to obtain an average of the results.

4.4.2. XRD Phase Analysis

X-Ray diffraction (XRD) was used to qualitatively determine the phases present in the composite material. The samples were examined using a PW 1710 Philips powder diffractometer, using monochromatic Cu (K_α) radiation produced at 40 KV and 20 mA. Diffractograms were collected over a range of 2θ between 20º and 80º, with a step size of 0.02º 2θ, together with a scan step time of 4.0 s.

Sintered samples found to contain peaks of unreacted-Al were subjected to Rietveld refinement analysis to determine the amount of elemental Al left in the samples. Rietveld refinement was done using Topas A version 4.1, and structural models used were taken from the ICSD - version 1.4.4

Powder X-ray diffraction data were collected using a Bruker AXS D8 equipped with a primary beam Göbel mirror, a radial Soller slit, a VÅntec-1 detector and using Cu-K_α radiation (40kV, 40mA). Data were collected in the 2θ range of 5º to 100° in

0.021° steps, using a scan speed resulting in an equivalent counting time of 73.2 s per step.

4.4.3. Microstructural SEM and EDS Analysis

A Scanning Electron Microscope (SEM) (LEO1525FE) was used to study the microstructure of the composite materials. An EDX (energy dispersing X-ray) spectrometer was used to identify the elemental composition of the various phases in the microstructure. This was used to support the evidence of the XRD analysis and to find evidence of free aluminium that could not be found in the XRD analysis.

The samples were non-conductive; an acceleration voltage of 2 – 20 keV was used. A low voltage was used for the fracture surface analysis while high voltages were used for the study of the microstructure. Double-sided carbon tape was used to mount the samples onto the aluminium sample holders and also to provide the electrical conductivity. The samples were not coated. An assortment of magnifications of micrographs were taken ranging between 100 – 10 000X. SEM was also used in the fractographic analysis of the fracture surfaces.

4.4.4. Density

The density of the samples was measured using the Archimedes principle. The sample's dry weight, W_{dry}, was measured. The samples were immersed in water, and

boiled for 3 h in order to displace air from the pores in the samples. After boiling, the samples in the water were allowed to cool to room temperature.

The samples were then removed from the water and lightly dried using some cloth or tissue paper to remove excess water on the surface of the samples. The weight of the samples was measured and the saturated weight W_{isat} was recorded. The samples were then suspended in water and the weight of the saturated samples W_{susp} were measured. The temperature of the water was also measured to determine its density. These measured quantities were then used to calculate the densities of the samples. The sample density is determined through equation 4.1.

$$\rho = \frac{W_{dry}}{V} = \frac{W_{dry} \times \rho_{H2O\,@\,Temp\,of H2O}}{(W_{sat} - W_{sus})_i} \qquad (4.1)$$

$$\rho(H_2O @ 23^{\circ}C) = 0.99756\, g.cm^{-3}$$

The density was determined at least twice per sample. Between each measurement the samples were dried in an oven.

The theoretical density of a composite material depends on the amount of the phases present in it. In this work, the amount of aluminium added to the boron nitride ranged between 15 and 25 vol. %. The density of the cBN used for the calculation of the theoretical density of the composite was taken from the data in Table 2.1 in Section 2.2. The densities of Al (2.701 g/cm^3) and cBN (3.48 g/cm^3) were used for the calculation of the theoretical density.

Using the following equation:

$$\rho = \frac{100}{\sum \frac{m_i}{\rho_i}} \qquad (4.2)$$

Where ρ, ρ_i and m_i is the theoretical density of the composite, the density and mass % of each component *i* respectively.

This formula is based on the rule of mixtures. The masses of each starting component, as well as the calculated theoretical density are given in Table 4.5 and 4.6 for the powder mixture and sintered materials respectively.

Table 4. 5: The theoretical densities of the cBN-Al powder mixtures.

Vol. % of Al	mass % of Al	mass % of cBN	Density ρ (g/cm^3)
15	12.13	87.87	3.36
20	16.36	83.64	3.32
25	20.69	79.31	3.28

Table 4. 6: The theoretical densities of the cBN-Al sintered material.

Vol. % cBN	Vol.% AlN	Vol.% AlB_2	Density ρ (g/cm^3)
85	9.37	5.63	3.41
80	12.50	7.50	3.40
75	15.62	9.38	3.38

4.4.5. Grain Size and Phase Composition

Image analysis techniques were been used to quantify and characterise the microstructure of the sintered PCBN-Al composite materials. The microstructures of the sintered materials were looked at in a Phillips-ESEM XL30 and 10 SEM micrographs of the microstructure were taken. The magnification of the micrographs depended on the grain size of the cBN materials; a high magnification was used for G2 and G6 materials while a low magnification was used for G10 and G20 materials. The micrographs included in this work represented the average microstructure for each material.

Using the image analysis software program (AnalySIS "Pro") the grain size and the percentage of the binder and cBN phases were determined. In the micrographs analysed, areas with different light intensity were ascribed to different phases, thus allowing for a numerical determination of different phase constants. The cBN phase shows a lower light intensity than the binder phase.

The grain size and grain size distribution were determined by measuring the grain size for each grain and deriving a distribution. The data from the AnalySIS program was then processed automatically by using the Mathcad and Mathconnex programs. The program module was designed to calculate the grain size distribution and mean free path of both the cBN and binder phases for the PcBN materials. A detailed

analysis of the Image analysis techniques for the grain size and phase composition determination is given in Appendix A.

4.5. Mechanical Properties and Testing Techniques

4.5.1. Hardness

Hardness, H, is generally defined as a material's resistance to plastic deformation usually due to a static penetration by a harder material [(11)]. Hardness is an important parameter to describe the mechanical properties of a material, and can be determined by measuring the depth of penetration of a harder indenter, usually diamond. It influences a number of performance aspects of ceramics including compressive strength, wear, as well as machining and ballistics performance [(48)].

The indenter is loaded perpendicularly to the planar surface of the material, the area of indentation is measured and the hardness is thus related to the load divided by the area of plastic contact. Thus hardness can be defined as the ratio of the applied load P to the area of plastic contact A. The relationship defining hardness is given below [(55)]:

$$H = \frac{P}{A} = \beta \frac{P}{d^2} \qquad (4.3)$$

Where

H is the hardness

P – Applied load

A – Area of plastic contact

d – Characteristic size of the indentation impression

β – Constant dependent on the indenter geometry

The hardness testing of a material is an easy and simple way to determine the bulk mechanical properties of a material. The use of rigid indenters causes the material to have a highly strained crack system, which develops beneath the indentation. This could cause errors in the results.

There are various test techniques to determine the hardness of a material, namely the Vickers, Knoop, Brinell and Rockwell tests. They are all based on the penetration of indenter into a softer material, but differ in the indenter geometry. Hardness of a material depends on the test method and indenter geometry (i.e. Brinell, Vickers, Knoop), and varies with applied load, indenter shape and dimensions, as well as the microstructure of the material.

There are two major indenter geometries used widely for brittle materials like ceramics, namely Vickers and Knoop. The Vickers testing method is the standard method used to determine the hardness of various materials, especially those that have hard surfaces, as it is a reliable method of measuring the hardness and a type of indenter that can be used for various types of materials. Knoop testing can also be used for materials that are very brittle ceramics; it is used to define the relative microhardness of a material.

Knoop hardness measurements generally provide a lower value than the Vickers hardness. Vickers hardness H_V, is measured on the contact area of the indentation impression, while Knoop hardness H_K, is calculated on the projected area of the indentation impression. Equation 3.1 can be used to calculate the hardness for both methods with β corresponding to 1.8544 for Vickers and 14.229 for Knoop. The characteristic size of the resultant indentation d changes for the two methods, for Vickers d is defined as the average of the two diagonals of the resultant squared shaped impression, while for Knoop it is the length of the diagonal of the resultant rhombic impression.

4.5.1.1. Vickers Hardness

The Vickers method to determine the hardness of ceramic materials was used in this study. The Vickers indentation method uses a square based, pyramid shaped diamond indenter with 136° angle between the two opposite faces, as shown in Figure 4.12.

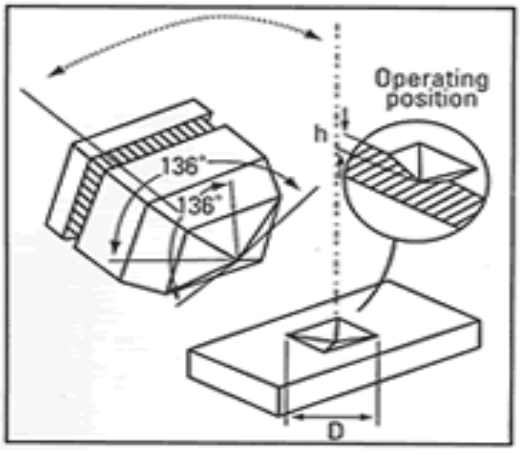

Figure 4. 12: The configuration of the Vickers diamond indenter.

A load is applied to the indenter which then causes an indentation in the sample material. After the load is removed, the two diagonals of the indentation left in the material are measured using a microscope and the averages are taken. The Vickers hardness, H_V, of the material can then be calculated by the following equation **(56)**:

$$H_V = 1.854 \times \frac{L}{d^2} \qquad (4.4)$$

Where L is the normal load (kgf) and d is the average length of the two diagonals (mm) of the Vickers indentation **(56)**. The Vickers hardness results are given in $kgmm^{-2}$, but are more commonly expressed in SI units, GPa.

4.5.1.2. Knoop Hardness

The Knoop testing method uses an elongated four-sided pyramid, with the angles between the two of the opposite faces being approximately 170º and the angle between the other two sides being 130º. The configuration of the Knoop diamond indenter is shown in Figure 4.13.

Similar to the Vickers method a load is applied to the indenter which causes an indentation in the sample material. After the load is removed, the longest of the two diagonals of the indentation left in the material is measured using a microscope. Knoop hardness, H_K, of a material can be calculated from the following equation **(57)**:

$$H_K = 14.229 \times \frac{L}{d^2} \qquad (4.5)$$

Where d is the length of the longest diagonal of the rhombic impression, which is approximately 7 times the width of the indentation, w.

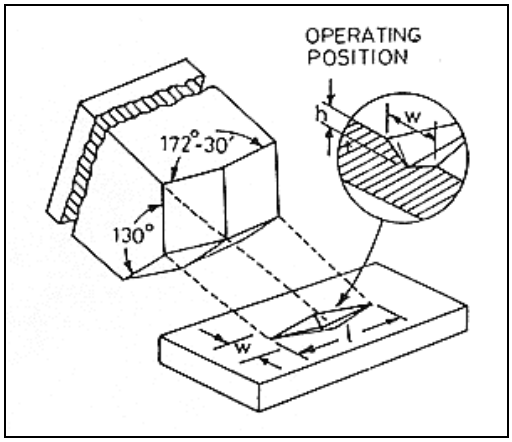

Figure 4. 13: The configuration of the Knoop Hardness indenter.

For this project the Vickers hardness technique was used to determine the hardness of the PcBN-Al composite materials. Samples need to be correctly polished so that the microstructure can be seen before hardness measurements can be done. The procedure for this is given in section 4.2.8. At least 10 hardness measurements were done per sample to get an average hardness value and a standard deviation. The loading conditions for the hardness measurements were a 5 kg load and a dwell time of 10 seconds. The average hardness and standard deviation for the hardness measurements were determined.

4.5.2. Fracture Toughness and R-curve Behaviour

There are a variety of different methods worldwide that can be used for measuring the fracture toughness of brittle materials and thus there is variability between the results of the various testing methods. The methods used for measuring the fracture toughness of brittle material range from indentation techniques to those involving crack propagation and the fracture of larger samples such as the double cantilever, double torsion, single edge notched beam, chevron notched beam or compression disk methods. The standard testing methods for fracture toughness of advanced ceramics is described in ASTM C1421-09 **(58)**.

The choice of an appropriate technique for PCBN materials is limited to the size of the sintered disk produced, which tends to be small. Preference of the fracture toughness test for this study was the single edge v-notch beam method (SEVNB) as it is a simple method based on the notch root radius, which gives relatively accurate results for all brittle materials, and samples can be made to the correct sample dimensions. The SEVNB technique has also been described in various standards and been subjected to extensive round robin practices **(59)**.

4.5.2.1.Single Edge V-Notch Beam (SEVNB)

The single edge V-notch beam method was used to determine the mode I fracture toughness, K_{Ic}, of the brittle materials made in this work. The test involved loading a

rectangular bar specimen which had a sharp V-shaped notch in one edge of the sample to failure. The test jig used for the SEVNB fracture toughness testing was the four-point flexure test jig. Figure 4.14 shows the four-point bend test jig and mechanical testing machine used for flexural testing. The samples' dimensions were 25 x 4 x 3 mm^3, thus the load and support span needed to be 10 and 20 mm apart respectively. The SEVNB method used is based on the fracture resistance method by Kübler (1999) **(59, 60)**.

The SEVNB samples were arranged so that the notched edge was in the tensile position (i.e. the notched surface opposite to the loading span) as seen in Figure 4.14. The samples were placed into the 4-point bend test jig and loaded to fracture in the universal servohydraulic testing machine MTS 810.22, 100 kN load frame, a 5 kN load cell being used to measure the load of fracture. The loading rate was 5 μm/s, equilvalent to ~ 100 N/s. TestStar was the control program used to measure the loading force; the maximum load to fracture was recorded. For fracture toughness 4 – 6 specimens were tested per materials composition.

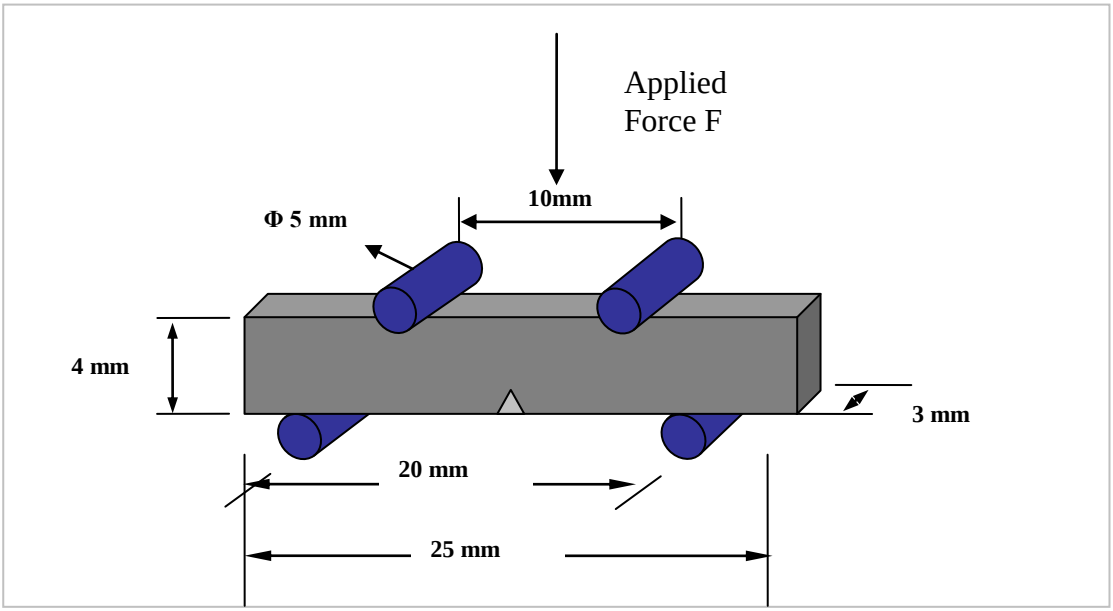

Figure 4. 14: The SEVNB arrangement in four-point bend configuration.

4.5.2.1.1. Machining of the V-Notch

Samples for the SEVNB fracture toughness testing required a 1 mm sharp V-shaped notch cut into the tensile surface. This was done in two stages; in the first stage 4 samples were aligned and glued onto a metal sample holder next to each other with the 3 mm tensile polished edge facing upwards. A 0.3 mm thick diamond saw was used to cut a 800 μm deep starter notch into the sample surface. The second stage involved cutting a sharp V-notch into the starter notch using a razor blade cutting machine. The razor blade edge in the razor blade holder was aligned with the middle of the starter notch and adjusted until it was straight and secured tightly in the holder. The notch was then filled with a fine diamond paste between 1 and 6 μm to facilitate cutting. The razor blade was put back into the starter notch and the blade was moved

backwards and forwards by a motor. The razor blade was changed every 30 minutes and extra diamond paste was used every 15 minutes. The larger size diamond paste was used first to facilitate the cutting process, followed by 3 and 1 μm paste to develop a sharp well-defined V-notch.

The sample was removed every 1 hour to measure the depth and sharpness of the V-notch by optical microscopic examination. The length of the notch was measured at three evenly spaced intervals across the sample width and then averaged. The relative deviations between the three measurements were not to exceed 0.1mm, to prevent a skew notch depth so as not to obtain inaccurate results. The notch tip radius needed to be between 10 – 30 μm and the total length of the notch 1 mm. Figure 4.15 shows the razor cutting machine and a V-notch cut into the PcBN-Al sample.

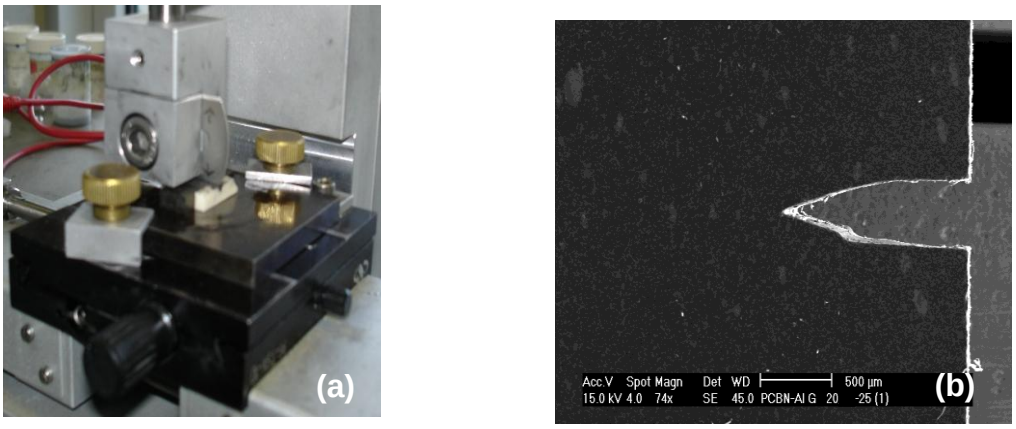

Figure 4. 15 a and b: a) The razor blade cutting machine to cut V-notches into the sample and b) a V-notch cut into the surface of the PcBN-Al sample.

The mode I fracture toughness, K_{1c} (MPa.$\sqrt{m}$) can be calculated for a 4-point flexure by the following equations [55, 59]:

$$K_{Ic} = \sigma\sqrt{a}Y = \frac{F}{B\sqrt{W}}.\frac{S_1 - S_2}{W}.\frac{3\sqrt{\alpha}}{2(1-\alpha)^{1.5}}Y \qquad (4.6)$$

With:

$$Y = 1.9887 - 1.326\alpha - \frac{(3.49 - 0.68\alpha + 1.35\alpha^2)\alpha(1-\alpha)}{(1+\alpha)^2} \qquad (4.7)$$

$$\alpha = \frac{a}{W} \qquad (4.8)$$

Where α is the relative notch depth, a is the average notch length (m), W is the specimen width (m), B is the specimen thickness (m), F is the fracture load (MN), Y stress intensity shape factor and S_1 & S_2 are the support spans (S_1>S_2).

The relative notch depth (α) is defined as the ratio of the notch length (a) to the width of the sample (W) and should be between $0.2 < \alpha < 0.3$.

4.5.2.2. R-curve Behaviour Compact Tension (CT)

Binders and other materials are used to improve the fracture toughness of brittle materials. These additives can provide toughening mechanisms, which will blunt the crack tip from the applied stress. Fracture toughness resistance is determined by the toughening mechanism of the material. Open displacement of the crack front can be

used to determine the toughening mechanisms of a composite material by looking at its R-curve behaviour.

The Compact tension (CT) method was used to determine the crack opening displacement for R-curve, v-K curve and fracture toughness, K_{IC}. The sample dimensions for the compact tension were 35 x 33.6 x 3 mm. A notch and 2 holes were laser cut into the surface of the sample. Figure 4.16 shows the sample dimensions of the CT sample.

A wire saw cut a diagonal cut into the end of the notch, such that the angle between the cut and the surface was approximately 30°. Figure 4.17 shows the cross section of the CT sample. A Knoop hardness indentation was positioned at the edge of the notch.

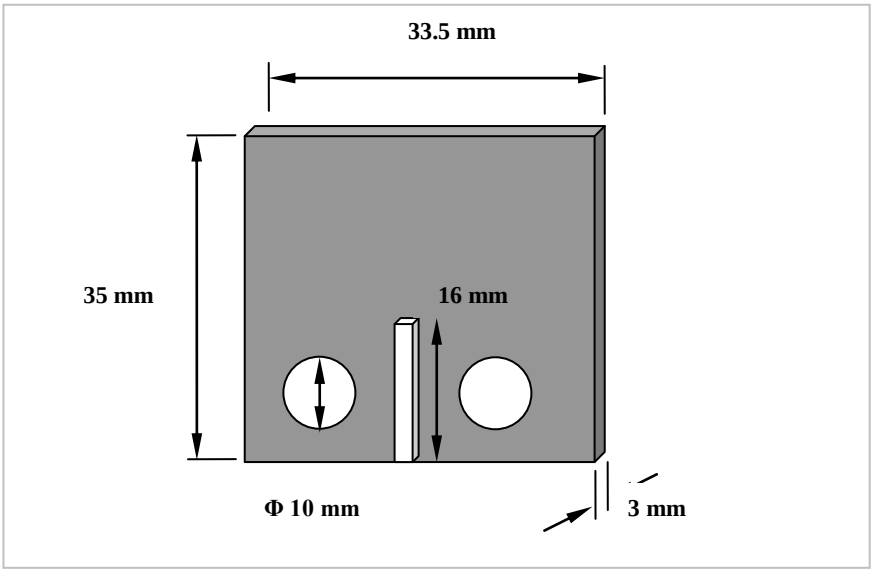

Figure 4. 16: The compact tension (CT) sample dimensions.

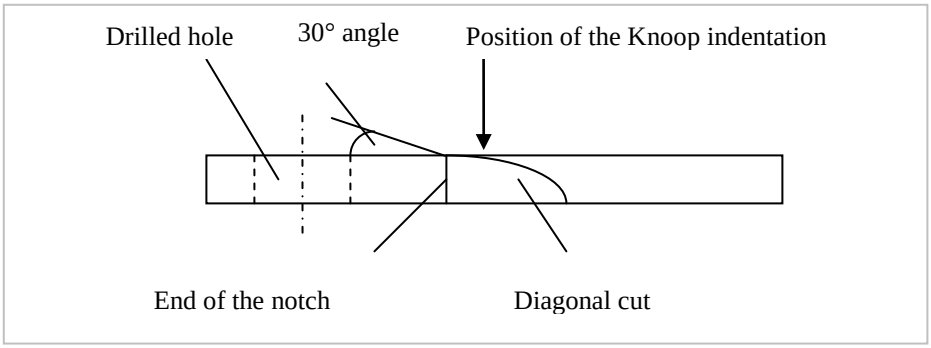

Figure 4. 17: Cross section of the CT sample

The Compact tension samples were carefully placed into the Compact Tension testing device as illustrated in Figure 4.18. A 1 kN load cell was used to measure the loading force. A preload of 20 N was applied to the sample to cause a crack to form from the end of the indentation; the crack was then propagated to a length of 1- 2 mm. The sample was removed from the CT device and a new cut was made horizontally such that the diagonal cut was removed, but not the tip of the crack. This would ensure the stable, symmetrical loading of the crack.

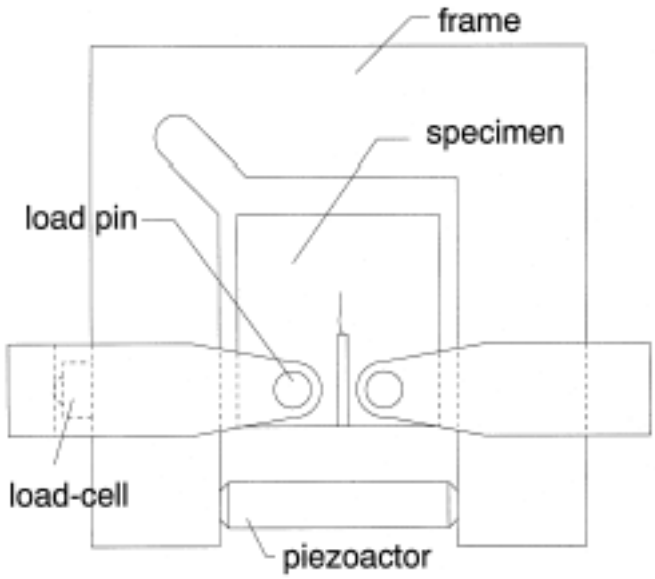

Figure 4. 18: Schematic of the testing device used for R-curve testing [61].

The sample was placed back into the CT device and a preload of 20 N was applied to the sample. The length of the crack was measured from the notch end to the crack tip. The sample was then loaded slowly until the crack started to grow at a steady rate and the crack length and load were also measured for every 0.2 mm. The load was applied until the sample broke.

The equation to calculate the fracture toughness resistance for the Compact Tension samples is given by [61]:

$$K_{IR} = \frac{F}{BW^{1/2}} f\left(\frac{c}{W}\right) \qquad (4.9)$$

$$f\left(\frac{c}{W}\right) = \frac{\left(2+\frac{c}{W}\right)\left(0.886+4.64\left(\frac{c}{W}\right)-13.32\left(\frac{c}{W}\right)^2+14.72\left(\frac{c}{W}\right)^3-5.6\left(\frac{c}{W}\right)^4\right)}{\left(1-\frac{c}{W}\right)^{3/2}} \qquad (4.10)$$

Where: $\frac{c}{W}$ is the ratio of the crack length to the width of the sample and is valid for:

$$0.2 < \frac{c}{W} < 1$$

4.5.3. Transverse Rupture Strength (TRS)

Transverse Rupture Strength (TRS) or Flexural strength is the property that determines the strength of a material. It is the maximum flow stress that occurs during the deformation, cracking and crack propagation process before the material fractures and is determined by measuring the flexural strength (the measure of the ultimate strength) of a bar of a material in bending.

The flexural strength of a material is dependent on both its inherent resistance to fracture and the presence of defects. The size of the flaws in the material can greatly decrease its strength. Failure in ceramic materials is caused by the extension of flaws, which are usually introduced in it during processing or surface treatment such as grinding and polishing. Flaws in the material can be inclusions, pores or cracks.

There are various internationally recognized standards that exist for the determination of flexural strength. The standard test method to determine the flexural strength of advanced ceramic materials at ambient temperatures is given in ASTM C 1161 **(62)** and ISO 14704:2000 **(63)**. The common specified dimensions for the 3PB and 4PB tests are 20, 40, 80 mm for the support span and 10, 20, 40 mm for the loading span

respectively. The dimensions used for this study were 25 x 4 x 3 mm with loading and support spans of 10 and 20 mm respectively.

The TRS of a material can be measured by flexural bend tests. These tests are easy to perform and they reveal selectively the worst flaws present in the stressed volume. Ultimately TRS is the stress required to make the longest crack in the sample propagate unstably and relate this to the statistical distribution of the stresses and flaws.

TRS is the stress calculated from the flexural formula required to break a specimen in the shape of a beam. The specimen is supported near its ends and a force is applied midway between the supports (in a 3 or 4-point bending test configuration). For this study a 4-point bend configuration was used and is illustrated in Figure 4.19. The sample dimensions were 25 x 4 x 3 mm and a 0.1 mm chamfer was machined into the edges of the sample to ensure that there were no machining defects at the edge of the sample to cause premature failure. The transverse rupture strength was determined using the standard methods for flexural testing as given in ASTM C 1161 **(62)** and ISO 14704:2000 **(63)**.

The bending tests were carried out on a universal servohydraulic testing machine MTS 810.22, 100 kN load frame and a load cell of 5 kN. The crosshead loading speed of 5 µm/s, equivalent to ~ 100 N/s was used. For the strength testing 20

samples per material composition were tested. The control program used to measure the loading force was TestStar; the maximum load to fracture was recorded.

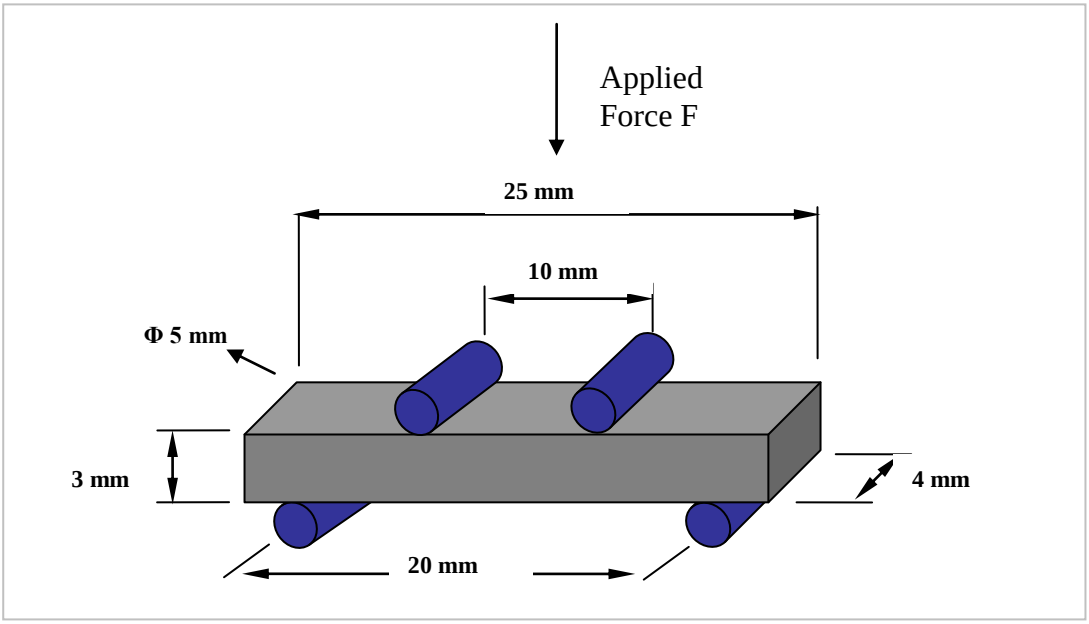

Figure 4. 19: The 4-point bend configuration for the Transverse Rupture Strength (TRS) tests.

TRS is determined by measuring the flexural strength of a material in a 4-point bending flexure, as shown in Figure 4.19. The flexural strength calculation can be determined from the ISO 14704:2000 [(63)] standards. Flexural strength is the measure of the ultimate strength of a specific beam in bending. The standard formula for the strength of a beam in a 4-point flexure is as follows [(63)]:

$$\sigma_f = \frac{3Fa}{bd^2} \qquad (4.11)$$

$$\text{Where } a = \frac{S_2 - S_1}{2}$$

Where:

F = load at failure (MPa),

a = length of the moment arm (mm)

S_1 and S_2 = outer and inner support span (mm),

b = specimen width (mm), and

d = specimen thickness (mm)

Since standard flexural strength data do not follow normal distribution, a statistical analysis of the strength data needs to be done to determine the statistical distribution. For the statistical analysis of the strength data the Weibull distribution approach was utilised. Section 4.5.3.2 details the use of the Weibull distribution.

4.5.3.1. Weibull Distribution

Brittle materials exhibit scatter of failure strengths. Thus with brittle materials, the strength property needs to be analysed using probabilistic approaches. The probability of existence of a critical crack size is higher in a larger volume of test specimen. Therefore brittle materials tend to exhibit a volume dependent strength behaviour; this means that the higher the loaded volume of test specimens the lower the strength.

Weibull (1939) **(64)** developed a relationship that would relate the probability of failure to the applied stress. In the Weibull analysis it is assumed that the material is

isotropic and statistically homogeneous and that the most critical flaw leads to failure. This implies that the probability of finding a flaw in the loaded volume of the material is equal in every direction. The second assumption is based on the concept of the 'weakest-link' theory; the largest flaw will cause failure. Weibull proposed a two-parameter distribution function, which would characterise the strength of brittle materials and relate it to the probability of failure.

The probability of an occurrence of a critical defect in a volume V is given by equation 4.12 **(54)**.

$$P(V) = 1 - \exp\left(-\frac{V}{V_O}\right) \qquad (4.12)$$

Where V_O is the mean volume occupied by a defect and thus $1/V_O$ is the concentration of the critical defects. The concentration of critical defects increases with increasing applied stress according to a powder law. Weibull developed an expression to relate the probability of occurrence of a defect with applied stress.

$$\frac{1}{V_O} = \left(\frac{\sigma}{\sigma_O}\right)^m \qquad (4.13)$$

$$P(V) = 1 - \exp\left[-V\left(\frac{\sigma}{\sigma_O}\right)^m\right] \qquad (4.14)$$

The probability of failure of a sample with a constant volume V is given by the following equation [(65)]:

$$P_f = 1 - \exp\left[-\left(\frac{\sigma}{\sigma_O}\right)^m\right] \quad \sigma > 0 \qquad (4.15)$$

Where σ_O is the Weibull characteristic strength (failure stress at 63.2% failure probability), σ is the applied uniaxial tensile stress and m is the Weibull modulus. The Weibull modulus m indicates the nature, severity and dispersion of the flaws; a low m value indicates a broad distribution of defects and therefore strength. A high m value indicates a narrow distribution of flaws with a narrower strength distribution [(66)]. Typically for ceramic materials m varies between 3 and 25 [(53, 66)], depending on the processing conditions. The minimum amount of valid tests that need to be performed to meet the statistic requirements is 20, although more should be used to get better statistics.

Weibull analysis of the strength data yields characteristic strength, σ_O, and Weibull modulus, m. These parameters were evaluated by the Maximum Likelihood method according to the European Standard EN 843-5 [(67)]. The 80% confidence intervals of σ_O and m were determined according to a study on the "Interferences on the parameters of the Weibull distribution" by Thoman (1969) [(68)].

Chapter 5: Results of High Pressure High Temperature Sintering

This chapter describes the results of the characterisation of the sintered PcBN-Al composite materials. The characterisation of the PcBN-Al composites includes SEM micrographs, XRD scans and density measurements. The grain size distribution and phase composition of these composites is also described in this chapter.

5.1. G 2 cBN – Al Materials

5.1.1. Microstructure

The cBN-Al powders were sintered using the HTHP method as explained in chapter 4.2.5. The sintered materials were then cut and polished according to the procedures described in Chapter 4. The microstructure of the polished sintered cBN-Al materials were examined in the SEM at various magnifications. Figure 5.1 shows the SEM images of the microstructure of the sintered G2 cBN-Al composites. The SEM images of show that these materials were nearly fully densified. The microstructures were homogeneous although larger binder pools can be seen in both the 20% and 25%Al materials. These binder pools were in the region of 5-10 μm and 10-20 μm respectively.

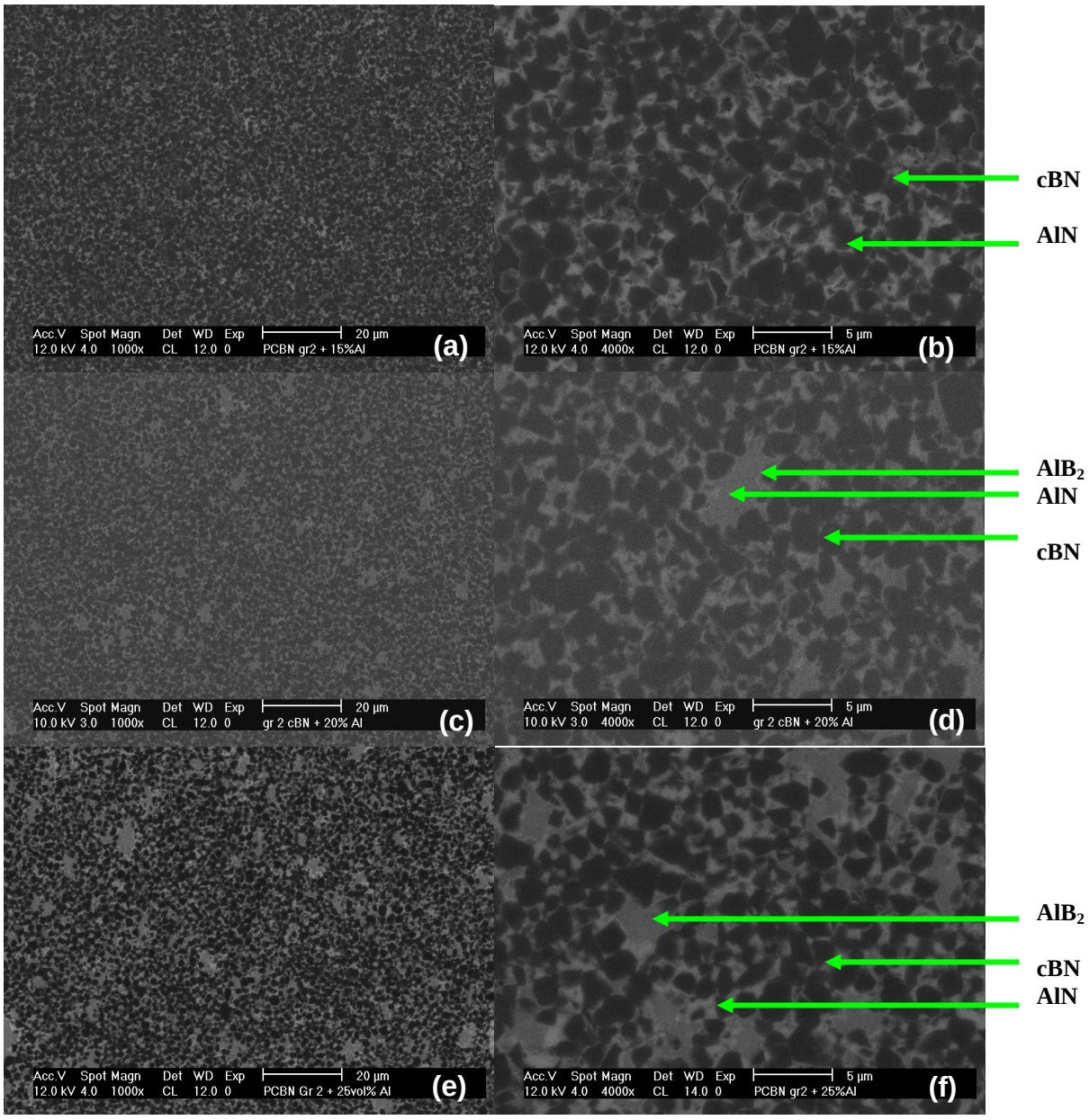

Figure 5. 1: Microstructure of the G2 cBN-Al sintered materials. a and b) G2 cBN+15vol.% Al; c and d) G2 cBN+20vol.% Al; and e and f) G2 cBN+25vol.% Al.

The microstructure of the G2 cBN-Al composite materials consisted of cBN grains (dark phase) surrounded by the residual binder phase. The binder phase consisted of aluminium nitride (AlN) and aluminium boride (AlB_2). The AlN phase is the lighter phase while the AlB_2 is the darker grey phase. These phases are confirmed by XRD

scans shown in Figures 5.2-5.4. These phases are consistent with Walmsley (1987) [(1)] and Zhao (2007) [(27)].

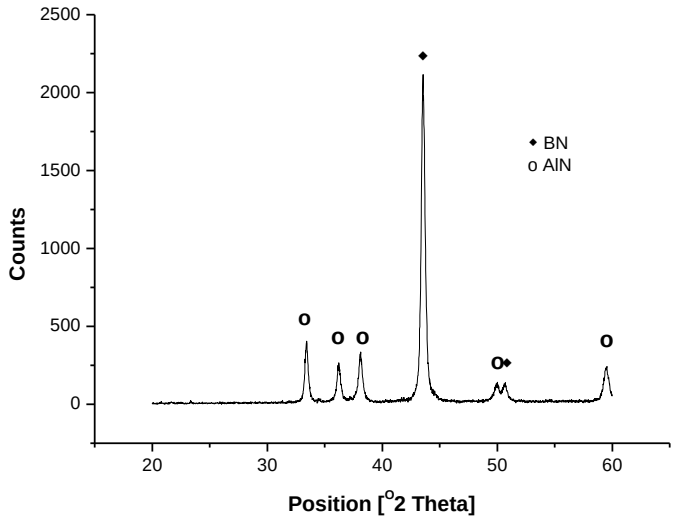

Figure 5. 2: XRD scan of the PcBN G 2 + 15 vol. % Al sintered material.

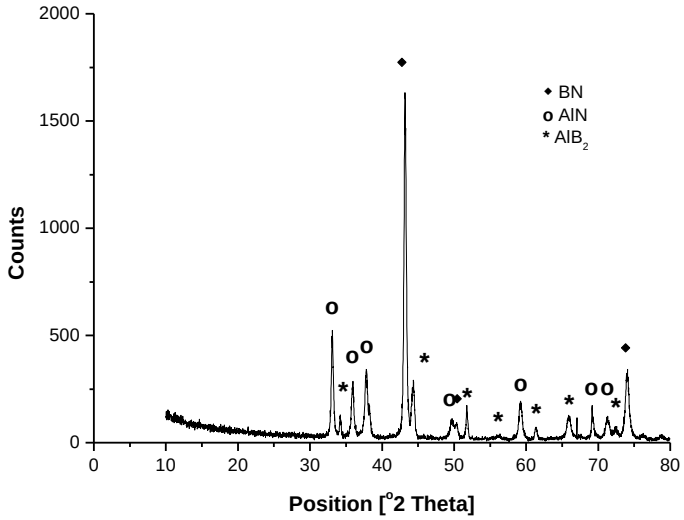

Figure 5. 3: XRD scan of the PcBN G 2+ 20 vol. % Al sintered material.

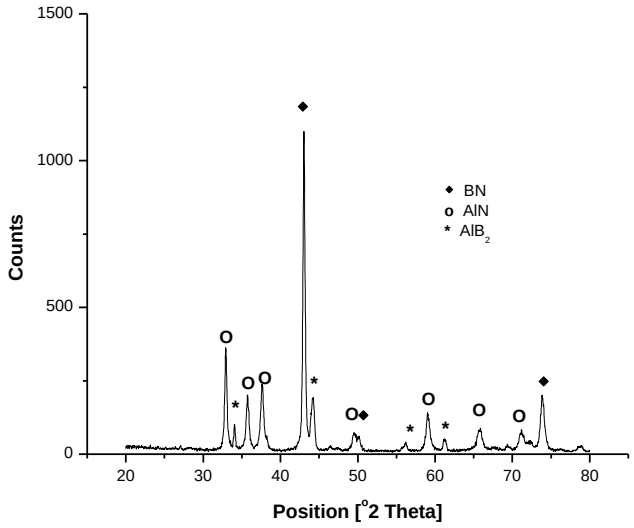

Figure 5. 4: XRD scan of the PcBN G 2 + 25 vol. % Al sintered material.

Tests were done to try to reduce the size of the binder pools for the G 2 + 25%Al; this was done by increasing the energy of mixing. Turbula mixing was carried out for longer time periods ranging from 1 – 10 hours and also increasing the number (10 balls) and/or size of the steel balls (20 mm). The increase in the energy intensity of mixing was used to deform the aluminium particles and to increase the contact area between the cBN grains and the aluminium particles. The intention was to decrease the size of the pools through this process.

After turbula mixing of the cBN and Al powders for 2, 4, 6, 8, and 10 hours, SEM analysis was done on the mixed powders. The results show very little difference in the cBN-Al contact. Two materials were then sintered with the 6-hour and 10-hour mixed powders to determine whether there was any change of obtaining an improved microstructure with increased mixing time. Both sintered materials showed only a

small reduction in the binder pool size and population as can be seen in Figure 5.5 a and b, compared with the 1 hour mixed sample in Figure 5.5 c. Increasing the number and size of the steel balls also had very little effect on the reduction of the binder pools. The reduction of the binder pools could be achieved by changing the mixing process to a wet mixing process like attrition milling, but wet milling contains its own problems like contamination of the powders from the milling media and the oxidation of the Aluminium powder.

It was thus decided to keep the original 1-hour mixing time and maintain the large binder pools. When amount of binder phase was too large, there was insufficient space between the cBN grains for the binder to infiltrate into the green compact when melting, thus causing large build-ups of the binder phase. All materials made with a binder content of 25 vol. % Al would suffer from these large binder pools.

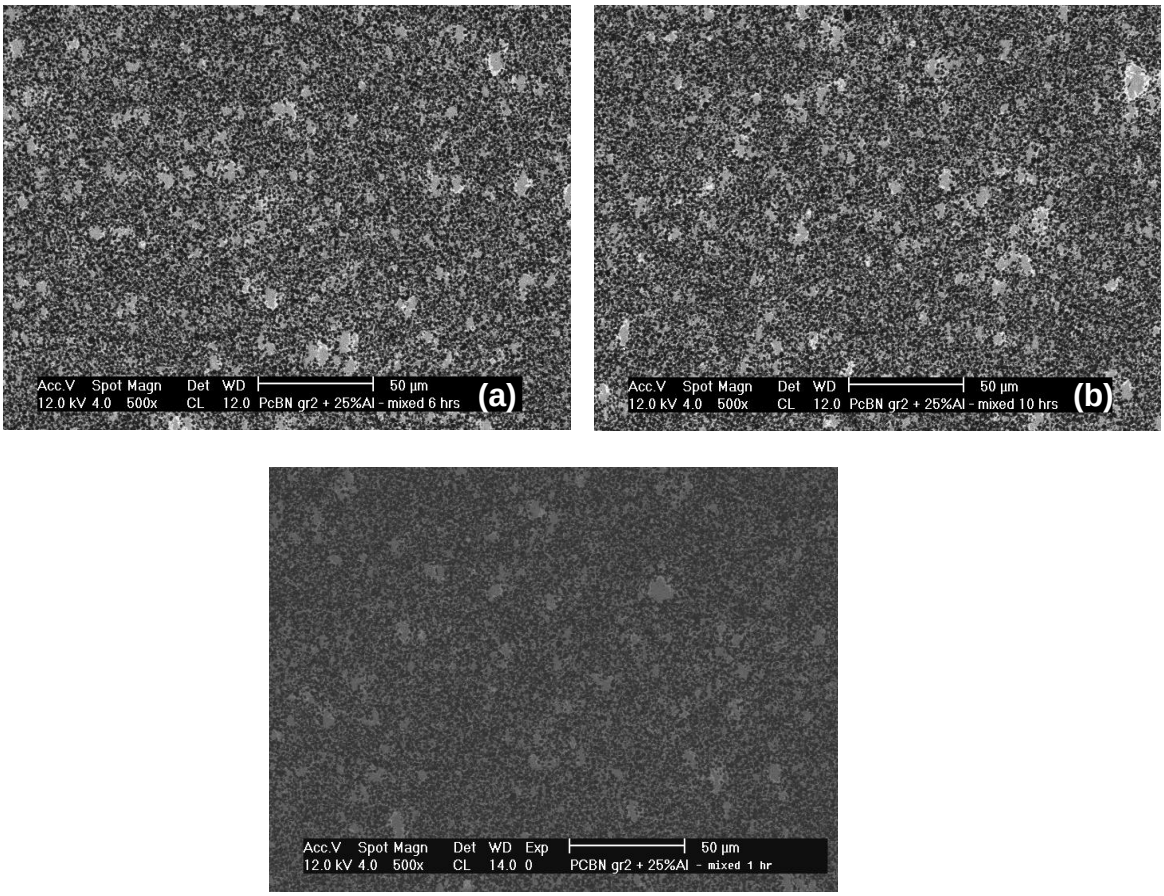

Figure 5. 5: SEM micrograph of the G 2 cBN + 25 vol. % Al sintered material turbula for a) 6 hours, b) 10 hours and c) 1 hour.

5.2 G 6 cBN – Al Materials

5.2.1. Microstructure

The microstructure of the polished sintered G6 cBN-Al materials were examined in the SEM at various magnifications. Figures 5.6 – 5.7 show the SEM images of the microstructure of the sintered G6 cBN-Al composites. The SEM images of the

microstructure of the G6 cBN-Al materials show that they were almost fully densified. The microstructures were homogeneous although an increase in the size and amount of the larger binder pools can be seen in both the 20 and 25%Al materials. The binder pools for the G6 cBN + 15%, 20% and 25% Al materials were in the region of 3-5 μm, 5-15 μm and 10-20 μm respectively.

The microstructure of the G6 cBN-Al composite materials consisted of cBN grains (dark phase) surrounded by the residual binder phase. The binder phase consists of aluminium nitride (AlN) and aluminium boride (AlB_2). The AlN phase is the lighter phase while the AlB_2 is the darker grey phase. These phases are confirmed by XRD traces shown in Figures 5.8-5.10. The free Al was confirmed in the XRD scan although the quantity was very small. These phases were consistent with the findings of Walmsley (1987) [(1)] and Zhao (2007) [(27)]. A small amount of free (unreacted) aluminium was found in the G6 cBN + 25vol.% sample with EDS, Figure 5.7 d. The amount of unreacted Aluminium was determined to be approximately 1.3 wt.%, determined by Rietveld refinement analysis outlined in chapter 4.4.2. The result of the Rietveld analysis is shown in Appendix B.

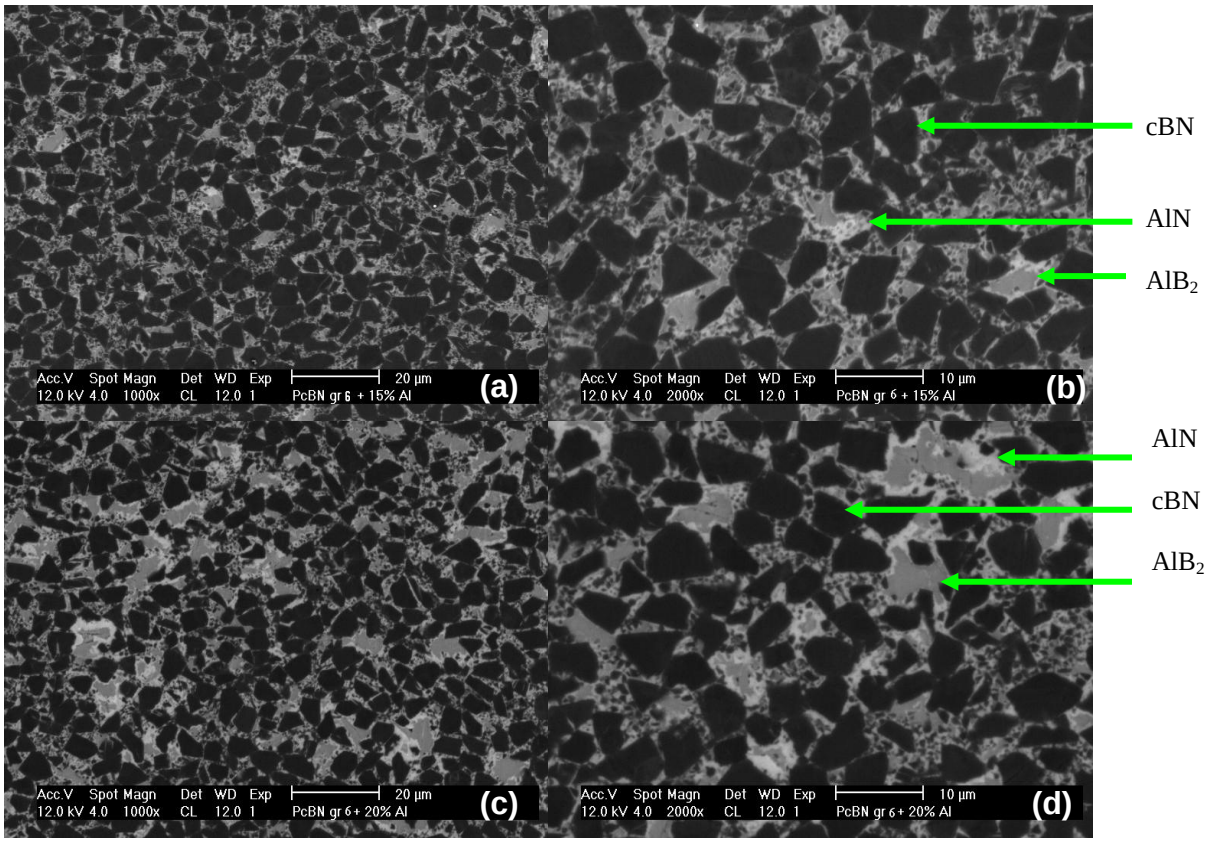

Figure 5. 6: SEM images of the microstructure of the PcBN G 6 –Al composite materials: a) and b) G6 cBN+15% Al; c) and d) G6 cBN+20% Al;

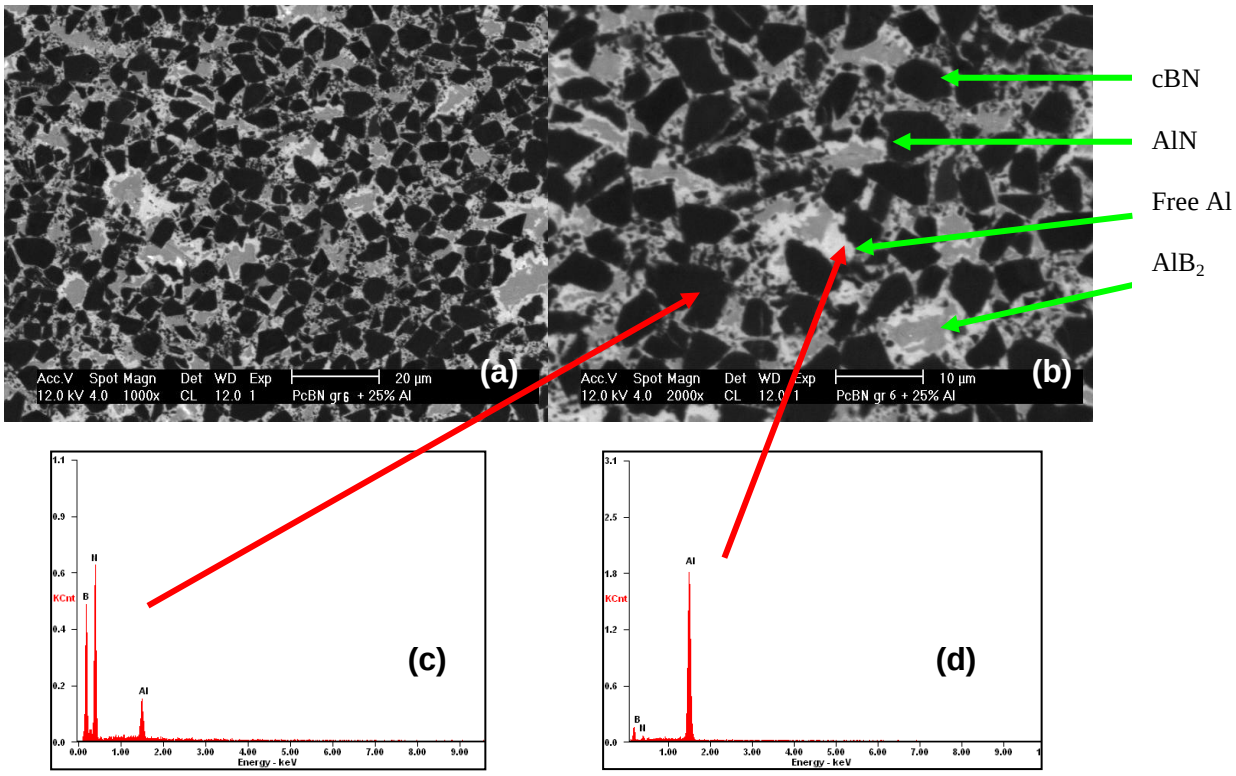

Figure 5. 7: SEM images of the microstructure of the PcBN G 6 +25vol.%Al composite materials: a) and b) micrographs c) EDS of a cBN grain and d) EDS image showing unreacted Aluminium.

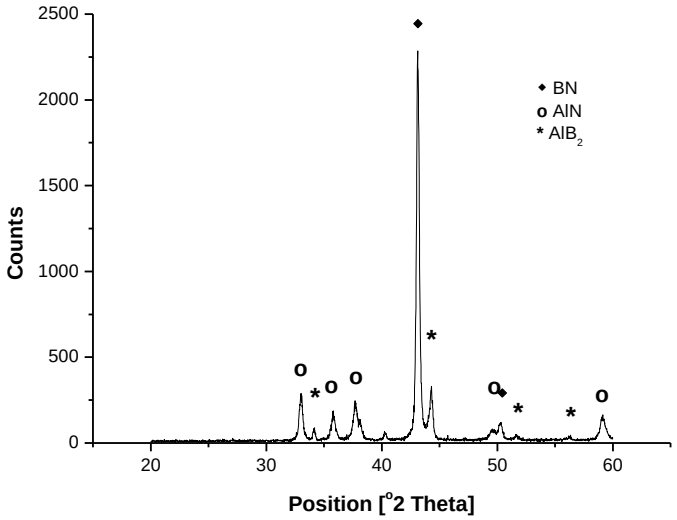

Figure 5. 8: XRD scan of the G 6 cBN + 15 vol. % Al sintered material.

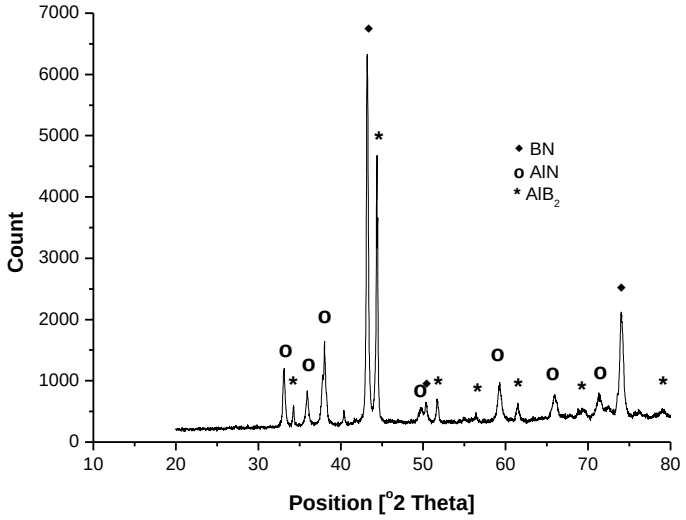

Figure 5. 9: XRD scan of the G 6 cBN + 20 vol. % Al sintered material.

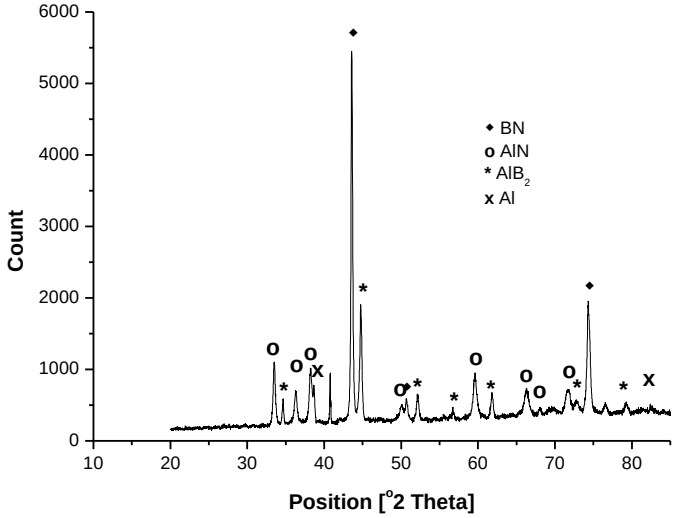

Figure 5. 10: XRD scan of the G 6 cBN + 25 vol. % Al sintered material.

5.3. G 10 cBN – Al Materials

5.3.1. Microstructure

The microstructure of the sintered G 10 cBN + 15 vol. % Al material can be seen in Figure 5.11. This shows that the microstructure was almost fully densified and had a homogeneous structure. The average binder pool was about 3-8 μm. The microstructure consisted of cBN grains (dark phase) surrounded by aluminium nitride (AlN) (lighter phase) and aluminium boride (AlB_2) (grey phase). This was confirmed by XRD phase analysis as seen in Figure 5.12. These phases were consistent with Walmsley(1987) [(1)] and Zhao (2007) [(27)]. No traces of unreacted Aluminium were found in XRD scans suggesting that all the Aluminium had reacted.

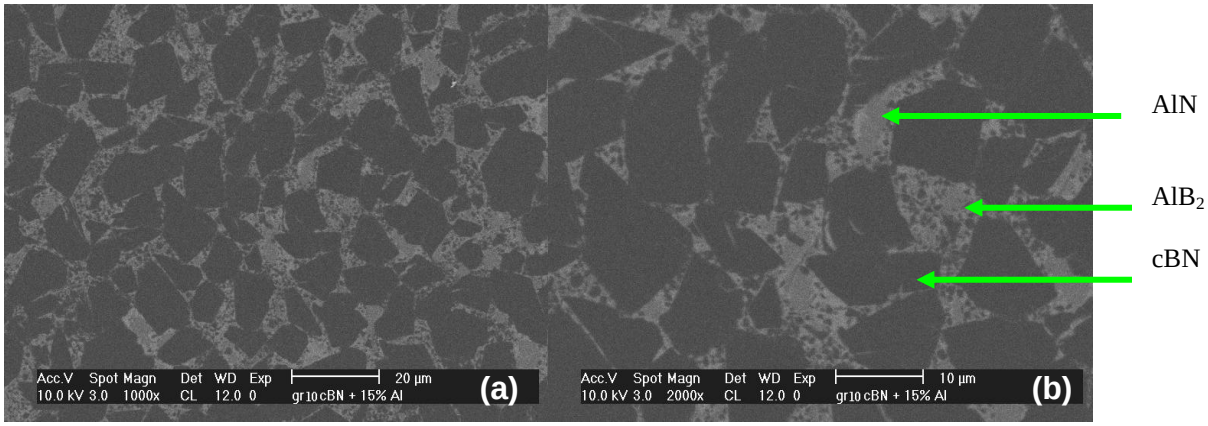

Figure 5. 11: SEM micrograph of the G 10 cBN + 15 vol. % Al sintered material.

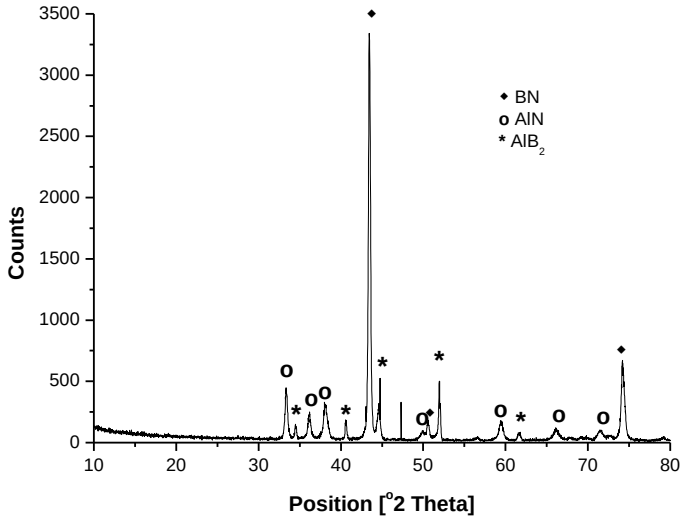

Figure 5. 12: XRD scan of the G 10 cBN + 15 vol. % Al sintered material.

5.4. Grade 20 cBN – Al Materials

5.4.1. Microstructure

The microstructure of the polished sintered G20 cBN-Al materials was examined in the SEM at various magnifications. Figures 5.13-5.14 show the SEM images of the microstructure of the sintered G20 cBN-Al composites. The SEM images of these materials show that they had been sintered to full density. The microstructures were homogeneous although an increase in the size and amount of the larger binder pools can be seen in both the 20 and 25%Al materials. The binder pools for the G20 cBN + 15%, 20% and 25% Al materials were in the region of 5-10 μm, 8-13 μm and 12-20 μm respectively.

The microstructure of the G20 cBN-Al composite materials consisted of cBN grains (dark phase) surrounded by the residual binder phase. The binder phase consisted of aluminium nitride (AlN) and aluminium boride (AlB_2). The AlN phase is the lighter phase while the AlB_2 is the darker grey phase. These phases were confirmed by XRD scans shown in Figures 5.15-5.17. These phases were consistent with Walmsley (1987) [(1)] and Zhao (2007) [(27)].

A small amount of free Al was found by SEM in combination with EDS and would be seen in the G20 cBN + 20vol.% and 25vol.%Al composite materials. Figure 5.14 c shows the unreacted Al in the G20 cBN + 25vol.% Al sample. The amount of unreacted Aluminium was determined using Rietveld refinement analysis (Chapter 4.4.2) and was approximately 1.1wt.% and 2.7 wt.% for the 20vol.% and 25vol.% respectively. The result of the Rietveld analysis is shown in Appendix A.

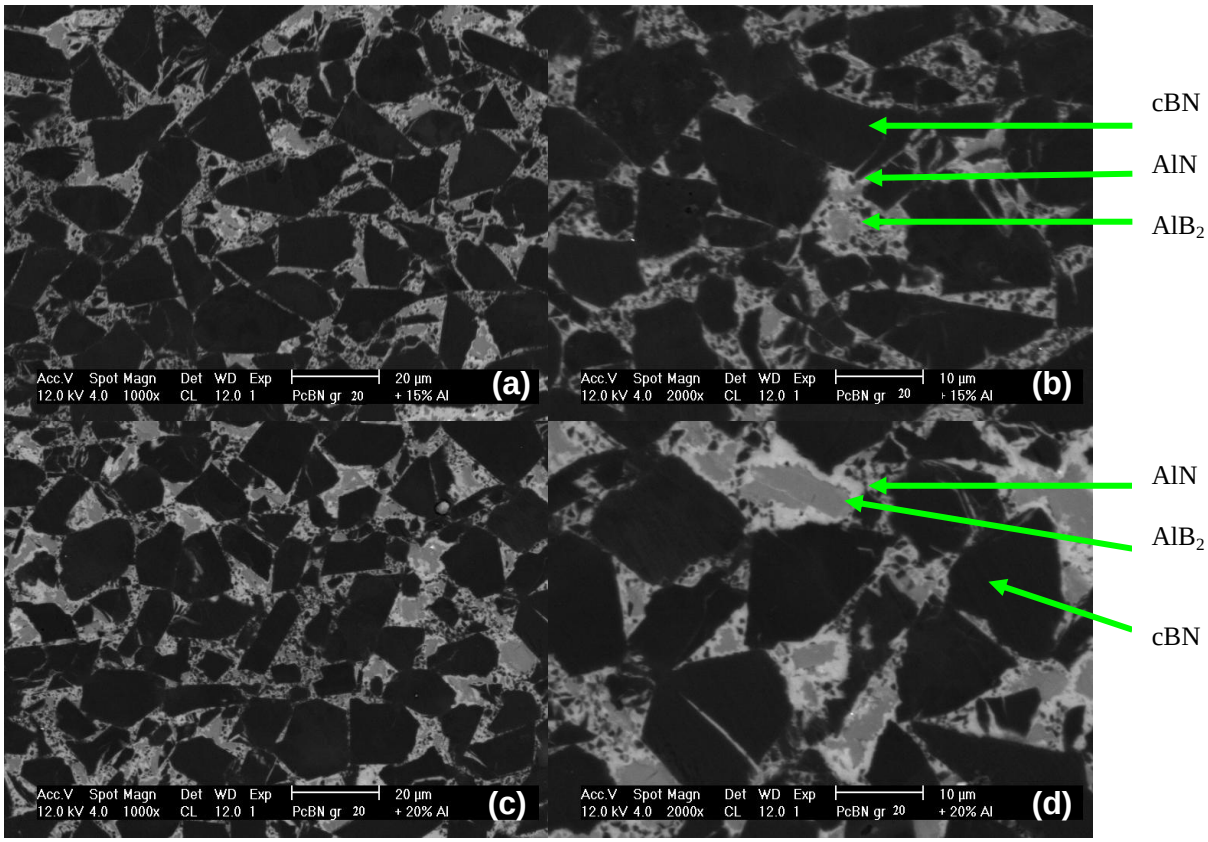

Figure 5. 13: SEM images of the microstructure of the PcBN G 20 –Al composite materials: a and b) G20 cBN+15vol.% Al; c and d) G20 cBN+20vol.% Al.

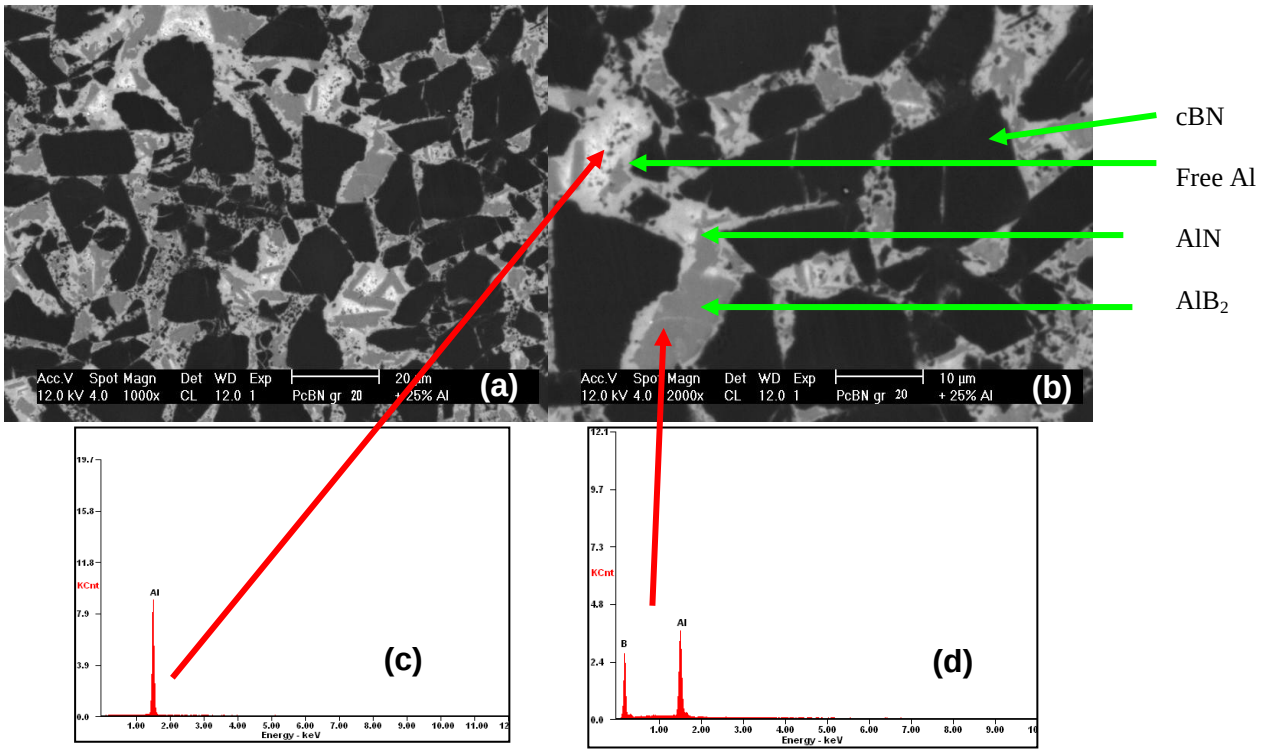

Figure 5. 14: SEM images of the microstructure of the PcBN G 20 + 25vol.% Al composite materials: a and b) microstructure, c) EDS of unreacted Aluminium and d) EDS of AlB_2.

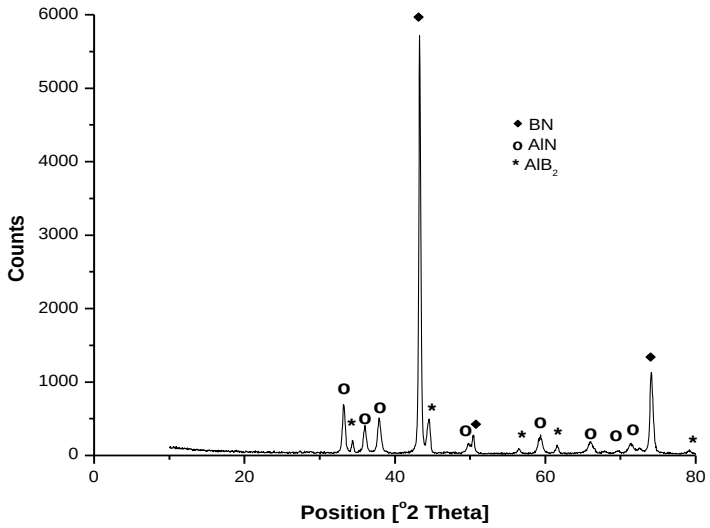

Figure 5. 15: XRD scan of the G 20 cBN + 15 vol. % Al sintered material.

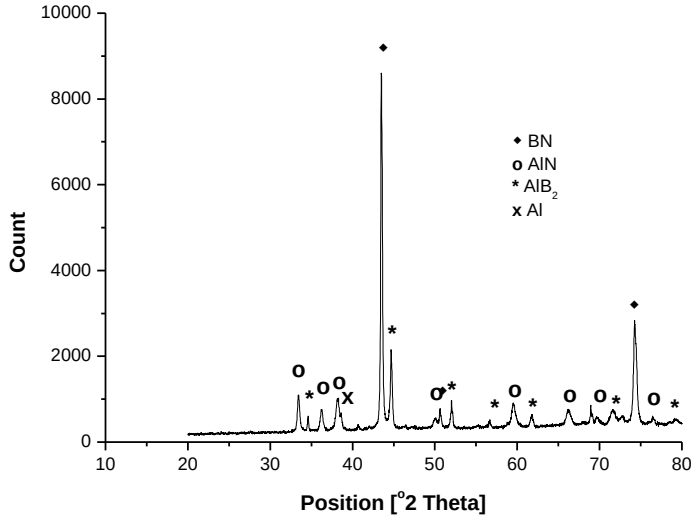

Figure 5. 16: XRD scan of the G 20 cBN + 20 vol. % Al sintered material.

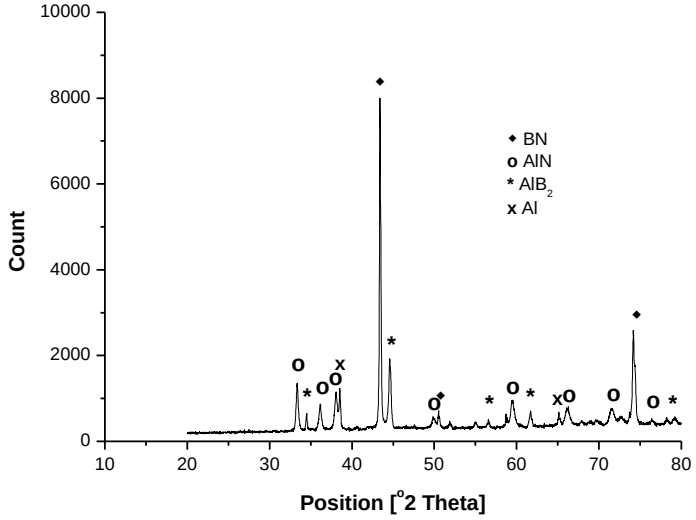

Figure 5. 17: XRD scan of the G 20 cBN + 25 vol. % Al sintered material.

5.5. Grain Size and Composition

The grain size distribution, volume fraction and mean free path of the cBN and binder phases, as well as the size of the Al pools were determined using image analysis as described in Appendix B. The maximum grains sizes as well as the d(10), d(50) and d(90) of the phases present in these composites were measured. Table 5.1 shows the predicted volume % of the binder and cBN phases for the PcBN-Al composite materials based on the mass balance calculation using cBN-Al reaction 1 (Section 2.4). Table 5.2 shows the composition and grain size of the PcBN-Al composites. The phase composition was very close to the predicted values. A detailed table of the cBN grain size, binder size and mean free paths (MFP) of both the cBN and binder phases is shown in Appendix B.

Table 5. 1: Predicted volume % of the binder and cBN phases for the PcBN-Al composite materials.

Volume % Of Al Added	Predicted Volume % of the binder phase	Predicted Volume % of the cBN hard phase
15	20.86	79.14
20	27.98	72.02
25	35.18	64.82

Table 5. 2: Composition and grain size of PcBN-Al composite materials.

Sample	Volume % cBN phase	Volume % Binder phase	cBN grain Size (Mean d_{50}) (μm)
G2 cBN+15%Al	82.1 ± 1.5	17.9 ± 1.5	1.5 ± 0.3
G2 cBN+20%Al	70.2 ± 1.8	29.8 ± 1.8	1.7 ± 0.3
G2 cBN+25%Al	60.0 ± 1.7	40.0 ± 1.7	1.8 ± 0.3
G6 cBN+15%Al	74.3 ± 1.9	25.70 ± 1.9	4.7 ± 1.2
G6 cBN+20%Al	67.9 ± 3.0	32.0 ± 3.0	4.7 ± 1.1
G6 cBN+25%Al	59.3 ± 4.1	40.7 ± 4.1	4.7 ± 0.9
G10 cBN+15%Al	80.7 ± 1.4	19.3 ± 1.4	10.8 ± 3.0
G20 cBN+15%Al	75.1 ± 2.3	24.9 ± 2.3	12.5 ± 3.2
G20 cBN+20%Al	70.5 ± 2.3	29.5 ± 2.3	13.2 ± 2.4
G20 cBN+25%Al	60.2 ± 2.7	39.8 ± 2.7	12.8 ± 2.8

5.6. Density Measurements of PcBN-Al Composite Materials

Density measurements were done on the sintered PcBN-Al composites. The Archimedes principle was used as described in Chapter 4.4.4. Table 5.3 shows the results of the density measurements. It can be seen that all the sintered materials were fully densified, with a density of 98.7-99.6% of the theoretical.

Table 5. 3: The density of the PcBN-Al composite materials.

Sample	Grain size of cBN	Density	
	(μm)	(g/cm^3)	(%)
Gr 2 cBN + 15 % Al	1.5	3.360	99.2
Gr 2 cBN + 20 % Al	1.7	3.350	99.6
Gr 2 cBN + 25 % Al	1.8	3.345	99.6
Gr 6 cBN + 15 % Al	4.7	3.392	99.6
Gr 6 cBN + 20 % Al	4.7	3.356	99.5
Gr 6 cBN + 25 % Al	4.7	3.347	99.7
Gr 10 cBN + 15 % Al	10.8	3.388	99.5
Gr 20 cBN + 15 % Al	12.5	3.362	98.7
Gr 20 cBN + 20 % Al	13.2	3.358	99.5
Gr 20 cBN + 25 % Al	12.8	3.308	99.1

Chapter 6: Results of Mechanical Properties of cBN-Al Composites

This chapter describes the results of the measurement of mechanical properties of the sintered PcBN-Al composite materials. The mechanical properties results described are hardness, fracture toughness, R-curve behaviour, transverse rupture strength and strength distribution. A discussion of the results will be given in Chapter 7.

6.1. Hardness

Details of the sample preparation for the hardness testing are described in Chapter 4.5.1. The hardness measurements were carried out using a Vicker's hardness indenter with a load of 5 kgf (49 N) and a dwell time of 10 s. The results of the Vicker's hardness measurements are given in Table 6.1, all data from the hardness measurements in Appendix D.

The results from Table 6.1 show that the hardness ranges between 15.6 ± 0.38 – 40.7 ± 1.2 GPa. G2 cBN + 15%Al had the highest hardness of 40 ± 1.2 GPa, while G20 cBN + 25 % Al had the lowest hardness of 15.6 ± 0.38 GPa.

Table 6. 1: The Vickers Hardness measurements results for PcBN-Al composite materials.

Sample	Grain Size (µm)	Hardness H_{V5} (GPa)	Standard deviation
G2cBN + 15%Al	1.5	40.7	1.20
G2cBN + 20%Al	1.7	33.5	1.15
G2cBN + 25%Al	1.8	32.0	1.65
G6cBN + 15%Al	4.7	36.0	1.39
G6cBN + 20%Al	4.7	27.2	0.38
G6cBN + 25%Al	4.7	22.0	1.47
G10cBN + 15%Al	10.8	35.8	2.51
G20cBN + 15%Al	12.5	23.2	1.74
G20cBN + 20%Al	13.2	19.8	1.50
G20cBN + 25%Al	12.8	15.6	0.38

6.2. Fracture Toughness

The details of the sample preparation and test procedure for the SEVNB fracture toughness measurements are described in Chapter 4.5.2. The results of the SEVNB average fracture toughness measurements for the cBN-Al composite materials and the grain size of the cBN particles and binder content are shown in Table 6.2; Appendix E contains all the SEVNB fracture toughness results. The fracture toughness for the cBN-Al composite materials was in the range of between 6.4 – 8.0 MPa.m$^{1/2}$. G10 cBN + 15vol.% Al had the highest fracture toughness of 8.0 ± 0.05 MPa.m$^{1/2}$, while G2 cBN + 15vol.% Al had the lowest fracture toughness of 6.4 ± 0.4 MPa.m$^{1/2}$.

Table 6. 2: SEVNB fracture toughness measurements results for PcBN-Al composite materials.

Sample	Grain Size (µm)	Fracture Toughness K_{IC} [MPa.m$^{1/2}$]	Standard deviation
G2cBN + 15%Al	1.5	6.4	0.4
G2cBN + 20%Al	1.7	7.0	0.5
G2cBN + 25%Al	1.8	7.1	0.2
G6cBN + 15%Al	4.7	7.6	0.7
G6cBN + 20%Al	4.7	7.6	0.3
G6cBN + 25%Al	4.7	7.0	0.3
G10cBN + 15%Al	10.8	8.0	0.1
G20cBN + 15%Al	12.5	7.9	0.2
G20cBN + 20%Al	13.2	7.8	0.3
G20cBN + 25%Al	12.8	6.9	0.1

6.3. R-Curve Behaviour (Compact Tension Measurements)

The details of the sample preparation and testing procedure for the R-curve behaviour measurements are given in Chapter 4.5.2.2. Table 6.3 shows the K_{IR} results of the CT measurements for R-curve behaviour. The results show that K_{IR} ranges between 3.8 – 9.1 MPa.m$^{1/2}$. The detailed results of the CT measurements are given in Appendix F. There could be inaccuracies with the resultant data from the CT measurements, due to large pre-cracks in the material, which were initiated in the materials during the laser machining of the notch and holes into the materials. These pre-cracks caused difficulty in initiating the crack used for the R-curve behaviour as described in Chapter 4.5.2.2. The pre-cracks were situated along the notch tip thus the pre-cracks

were used as the R-curve crack. The material was also brittle and once force was exerted to lengthen the crack, the crack propagated extremely quickly resulting in only a few data points per experiment. For some of the sample materials no data points could be extracted as the crack propagated too quickly through the material resulting in premature failure.

Table 6. 3: The K_R results for the R-curve behaviour.

Sample	K_{IR} (MPa.m$^{1/2}$)
G2cBN15Al	5.1 – 8.7
G2cBN20Al	6.5 – 7.6
G2cBN25Al	5.5 – 6.5
G6cBN15Al	3.8 – 7.6
G6cBN20Al	5.8 – 8.3
G6cBN25Al	5.0 – 9.1
G10cBN15Al	4.6 – 5.1
G20cBN15Al	5.8 – 9.5
G20cBN20Al	4.8 – 9.0
G20cBN25Al	5.3 – 8.6

Figures 6.1 – 6.3 show the R-curve behaviour with increasing crack lengths for the G2, G6 and G10 and the G20 PcBN-Al composite materials respectively. The cracks propagated stably for approximately 2-5 mm before unstable propagation occurred and the samples fractured.

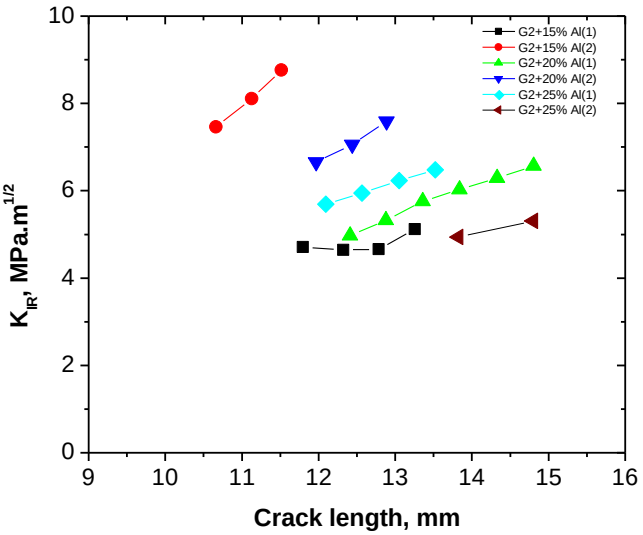

Figure 6. 1: R-Curve behaviour with crack length for G2 PcBN-Al composite materials.

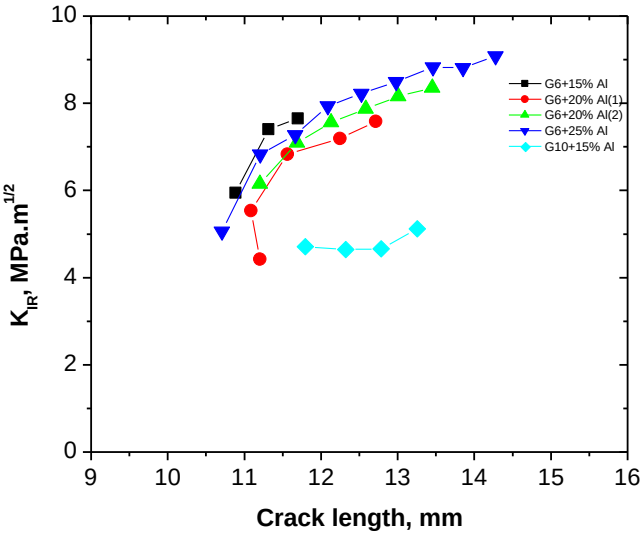

Figure 6. 2: R-Curve behaviour with crack length for G6 and 10 PcBN-Al composite materials.

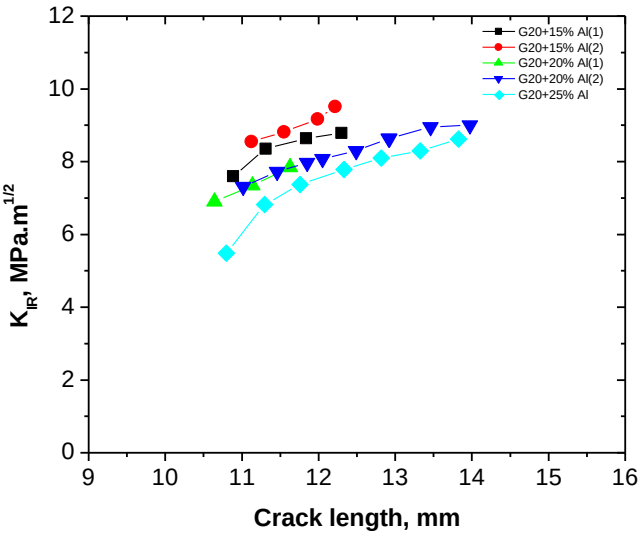

Figure 6. 3: R-Curve behaviour with crack length for G20 PcBN-Al composite materials.

6.4. Transverse Rupture Strength (TRS) Measurements

6.4.1. Strength Results

The details of the sample preparation and testing procedure for the transverse rupture strength measurements are given in Chapter 4.5.3. The samples were loaded to failure at a rate of 0.05 mm/min under a 4-point bend loading. The average flexural strength and standard deviation results for the PcBN-Al composite materials are shown in Table 6.4. These values were in the region of between 346.7 ± 19.7 – 443.9 ± 22.7 MPa. All the results of the flexural strength tests are given in Appendix G.

Table 6. 4: Average flexural strength results for the PcBN-Al composite materials.

Sample:	Grain Size (µm)	Mean Flexural Strength (MPa)	Standard Deviation
G 2 cBN + 15 % Al	1.5	372	41
G 2 cBN + 20 % Al	1.7	406	61
G 2 cBN + 25 % Al	1.8	426	42
G 6 cBN + 15 % Al	4.7	380	72
G 6 cBN + 20 % Al	4.7	382	30
G 6 cBN + 25 % Al	4.7	418	23
G 10 cBN + 15 % Al	10.8	444	23
G 20 cBN + 15 % Al	12.5	384	25
G 20 cBN + 20 % Al	13.2	347	20
G 20 cBN + 25 % Al	12.8	380	23

6.4.2 Weibull Analysis

The results of the Weibull analysis on the bending strength measurements are shown in Table 6.5, which shows the characteristic strength values (σ_o), the Weibull modulus (m), the 80% confidence intervals and the average flaw size of the composite materials. All the Weibull statistical data results per material can be seen in Appendix H.

The average characteristic strength values for the cBN composite materials were in a narrow range between 354 – 454 GPa. The G10 + 15 vol.% Al material had the highest average characteristic strength value of 454 GPa, while the G20 + 20 vol.%

Al material had the lowest average characteristic strength of 355 GPa. The strength values for the cBN-Al composite materials were low compared to other commercially available PcBN materials. The range of the Weibull moduli between 6.1 - 24.9 was quite big.

Table 6. 5: Characteristic strength σ_o, Weibull modulus m, 80% confidence intervals (C.I) and average flaw size of the PcBN-Al composite materials.

Sample	Characteristic Strength σ_O (MPa)	80% C.I	M	80% C.I
G2cBN+15%Al	390	377 – 405	9.8	7.2 – 11.7
G2cBN+20%Al	433	413 – 454	7.0	5.3 – 8.3
G2cBN+25%Al	445	431 – 459	10.7	8.1 – 12.7
G6cBN+15%Al	409	389 – 432	6.1	4.7 – 7.3
G6cBN+20%Al	395	386 – 403	15.7	11.8 – 18.7
G6cBN+25%Al	429	420 – 438	16.2	12.3 – 19.3
G10cBN+15%Al	454	448 – 460	24.0	18.2 – 28.5
G20cBN+15%Al	396	388 – 404	16.6	12.6 – 19.8
G20cBN+20%Al	355	250 – 340	24.9	18.9 – 29.6
G20cBN+25%Al	390	383 – 396	19.9	14.9 – 23.7

Chapter 7: Discussion of Results

Hardness

The results show high hardness values in the expected range with a standard deviation of less than 10%. Expected hardness values can be calculated by using the assumption of the rule of volume mixtures using equation 3.2, section 3.4.1. The results can be viewed in Appendix C. Figure 7.1, 7.2 and 7.3 shows the results of the Vickers hardness measurements of the sintered polycrystalline cBN-Al composites at room temperature plotted against the grain size of the cBN hard phase, the inverse of the square root of cBN grain size and the binder content respectively. This shows the effect the grain size and binder content had on the hardness values.

The hardness of the PCBN-Al composite materials produced from Table 6.1 ranges between 15.6 ± 0.38 – 40.7 ± 1.2 GPa. Compared to other PcBN materials these values are quite reasonable. The hardness of single crystal cBN grains is 43 GPa [(7)] and Amborite [(11)] (Element Six (Pty) Ltd commercially produced material which contains 90vol.% of cBN with aluminium nitride and aluminium borides as the binder phases) has a Knoop hardness of 31.5 GPa. Rong and Funkunaga (2002, 1994) [(6, 26)] measured the Knoop hardness of their cBN-Al composite to be between 15 – 35 GPa. Comparisons with results obtained by Rong and Funkunaga [(6, 26)] are limited, as different hardness measurement tests have been done (i.e. Knoop and Vickers). A conversion between the Knoop and Vickers methods can be done, but there will still

be an error associated with it. Hardness results of cBN-Al composites obtained by Li [8] showed 20 - 32.7 GPa for 70 - 95 wt.% cBN.

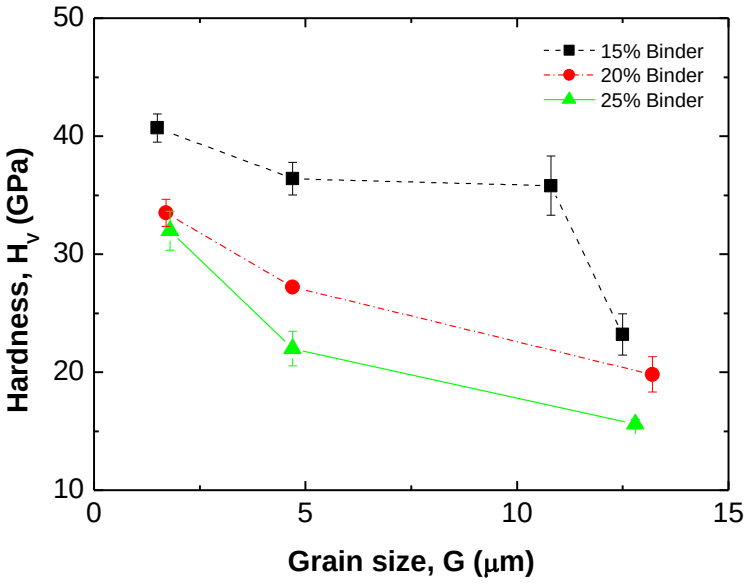

Figure 7. 1: Hardness as a function of the grain size of the cBN particles.

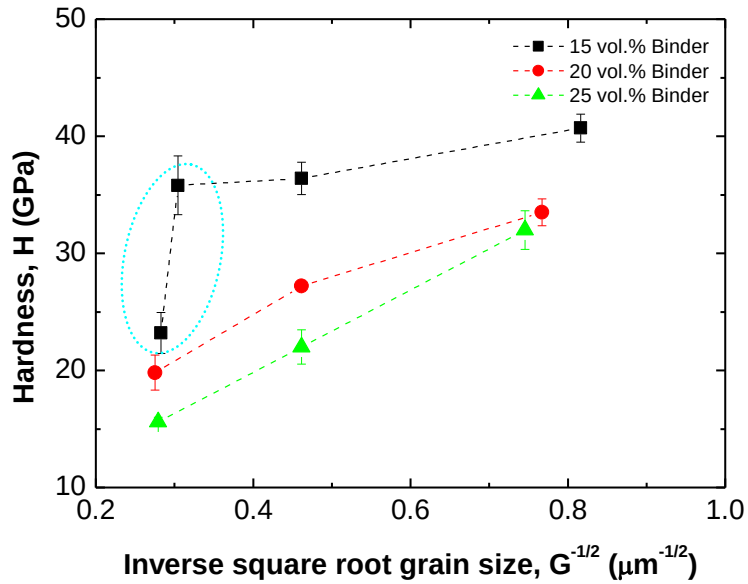

Figure 7. 2: Hardness as a function of the inverse square root of the cBN grain size.

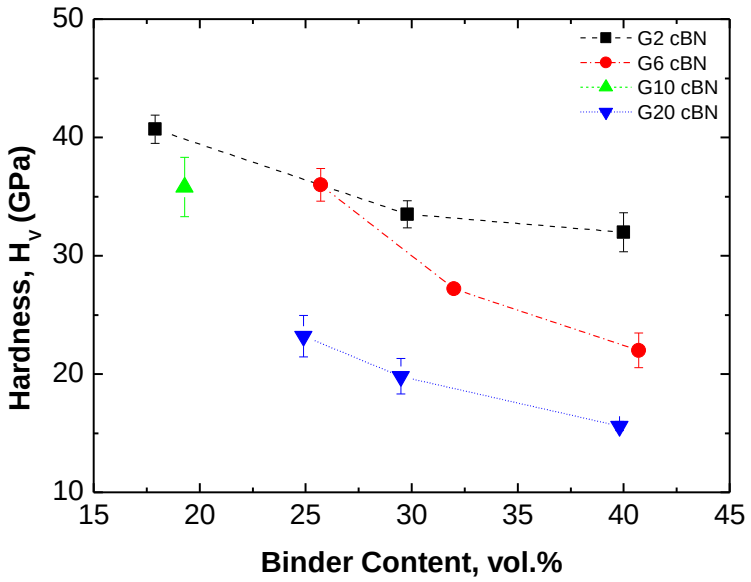

Figure 7. 3: Hardness as a function of the binder content.

From Figures 7.1 – 7.3 it can be seen that hardness decreases with increasing cBN grain size and increasing binder content. This is expected since the hardness of the material is dependent mainly on the hardness of the ultra-hard phase. Since the binder, consisting of AlN and AlB_2, is softer than cBN there will be weaker phases bridging the cBN grains, thus reducing the hardness of the material. At lower binder content there is more cBN-cBN contact, giving rise to a rigid mechanically locked skeleton which leads to higher hardness values.

The hardness also decreases with the increasing cBN grain size as predicted by the Hall-Petch relationship [48] (i.e. $H \propto 1/\sqrt{d}$ given in equation 3.3 in Chapter 3.4.1). Except for the lowest binder content where it deviates for the largest grain size, as

seen in Figure 7.2 (shown by circle), the reason for this behaviour is probably that the materials consisting of larger grains have poorer sinterability and some residual porosity. The slope of the lines $H \propto 1/\sqrt{d}$ reduces with reducing binder content.

The decrease in hardness with increasing grain size suggests that the hardness is dependent on the grain size of the cBN particles. The smaller the cBN grains the larger the grain boundary area, therefore there is less slip between the grains. The decrease in hardness with increasing binder phase per material grade is not quite linear, also the hardness doesn't decrease linearly with increasing grain size.

A statistical study into the effect of both the grain size and binder content has been carried out. Minitab, a statistical software program, was used to determine the correlation between each of the properties and the affected parameters. Appendix J shows the results of the General linear model and the Two-Way ANOVA tests.

The results of the Hardness measurements as a function of both the cBN grain size and the binder content are shown in Figure 7.4, while in Figure 7.5, the main effects of the hardness measurements are shown. It is clear that Hardness decreases with increasing binder content and cBN grain size, although there is a maximum observed at G10. It is unclear whether the maximum at G10 is real or is a result of error in the statistics.

The contributions of each effect on the hardness were determined using a general linear model and the Two-way ANOVA model, shown in Appendix J. The results from the Two way ANOVA model shows the grain size had a 67% effect on the hardness and the binder content had a 28%, which shows that the grain size had a larger effect on the hardness than the binder content in the investigated concentration range of the binders.

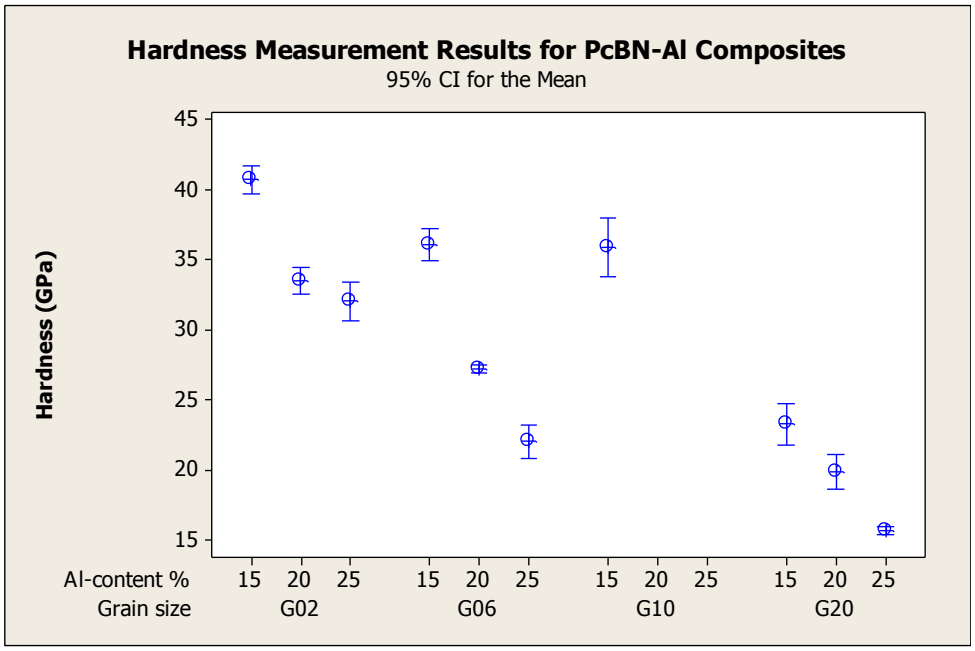

Figure 7. 4: Hardness as a function of the cBN grain size and the binder content.

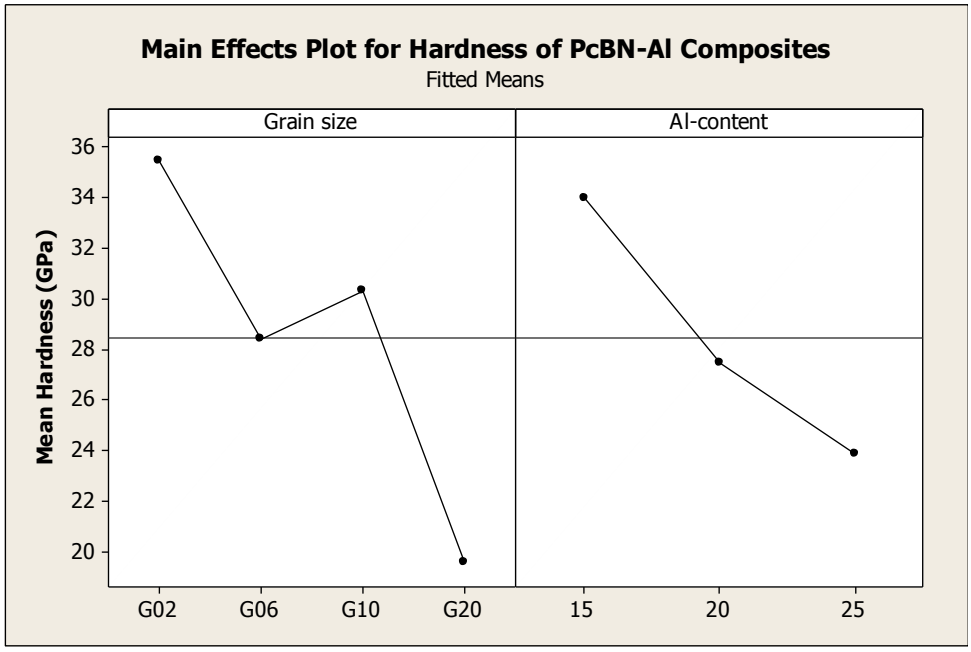

Figure 7. 5: Main effect plot of the Hardness with cBN grain size and Al content.

Fracture Toughness

The fracture toughness for the cBN-Al composite materials is in the range between 6.4 – 8.0 MPa.m$^{1/2}$ (Table 6.2). The measured fracture toughness values are above those reported for commercially available PcBN materials of 3.5 – 6.6 MPa.m$^{1/2}$ **(11)**, and are also mostly higher than the values reported for Amborite, with a fracture toughness of 6.4 MPa.m$^{1/2}$ **(11)**. It is difficult to directly compare the data of the PcBN-Al composite and the data from literature as they were determined by different testing methods (i.e. SEVNB and indentation methods). The results obtained for the PcBN-Al composite materials exhibit a low standard deviation, less than 10 %. Figure 7.6, 7.7 and 7.8 show the plots of the SEVNB fracture toughness results as a

function of grain size of cBN particles, the inverse of the square root of cBN grain size and binder content respectively.

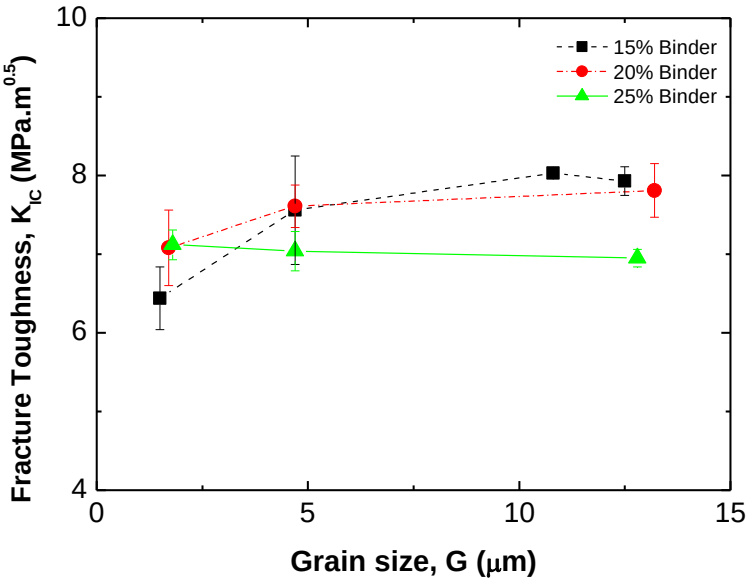

Figure 7. 6: Fracture toughness of the PcBN-Al composite materials as a function of grain size of cBN, using SEVNB method.

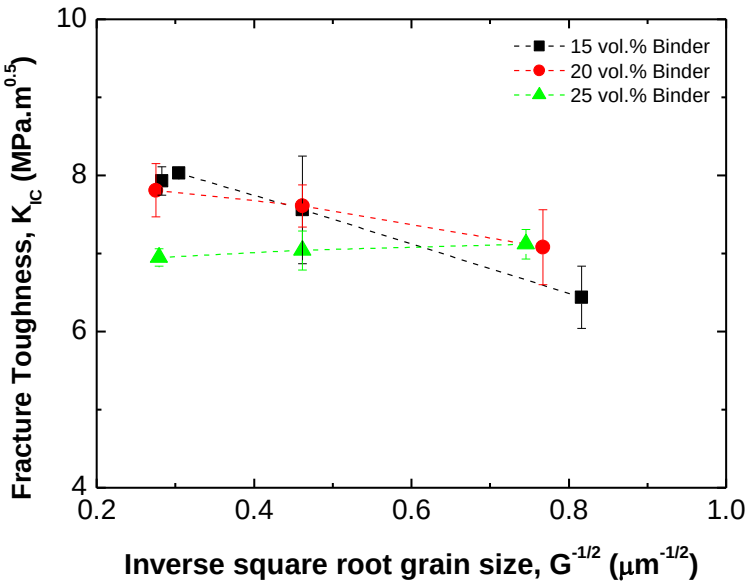

Figure 7. 7: Fracture toughness of PcBN-Al composite materials as a function of the inverse square root of the cBN grain size.

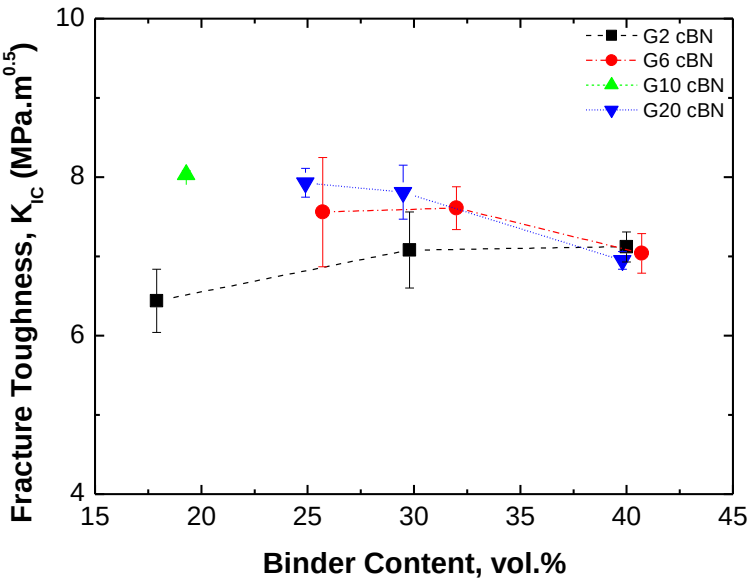

Figure 7. 8: Fracture toughness of the PcBN-Al composite materials as a function of binder %, using SEVNB method.

The fracture toughness for all composite materials studied in this work generally increases with increasing cBN grain size, except for the composites with 25vol.% binder where the K_{IC} is constant within the errors of the determinations (Figure 7.6 and 7.8). The increase in fracture toughness with increasing grain size is consistent with work done on Al_2O_3 materials [70, 71, 72]. There is no significant grain size dependence on the fracture toughness, although larger grains act as crack deflection sites resulting in a higher fracture toughness.

Considering the binder content, the fracture toughness of the batches with 6 and 20 µm cBN grain size does not show a significant dependence on binder content at 15 – 20vol.%, but decreases at 25vol.%. However, at low binder level, the batches with 2

µm grain size show a slight increase of fracture toughness with increasing binder content. The toughness generally decreases with increasing binder content, except for the G2 cBN composites where the opposite trend can be seen, although these values are within the experimental error, suggesting constant values or a slight increase. This suggests that at fine grain size the material is very brittle due to a higher cBN-cBN contact. Increasing the binder content provides the material with more weaker phases is more prone to plastic deformation. The distance between the particles is influenced by the amount of binder content; for smaller particles the distance between the grains is smaller than for larger particles. If the distance between the particles is too high (i.e. high binder content) a negative effect results due to the weakness of the binder phases, as seen from the decrease in fracture toughness for the higher binder contents.

At larger grain sizes there is a high amount of crack deflection, by increasing the binder content to 25vol.%, a decrease in the fracture toughness occurs. As the distance between two grains increases the less stress is required for crack propagation therefore cracking is easier long the binder phase with fewer grains providing crack deflection.

Analysis of the crack path and fracture surfaces of the PCBN-Al composites was done. Figure 7.9 and 7.10 show crack propagation paths through a G20 cBN + 25vol.% Al composite material and fracture surfaces of fracture toughness samples of G2cBN + 15vol.% Al and of G20 cBN + 25vol.% Al respectively. The fracture mode

is transgranular, both in the cBN phase and in the binder. From the crack path in Figure 7.9, a tendency of predominant crack propagation in the binder phase might be deduced; this is valid at least for that material composition and microstructure. The crack propagates mostly through the binder, and along the grain boundaries between the different binder phases.

The high fracture toughness values obtained was substantiated by crack deflection/bridging observed during crack propagation, Figure 7.9. Crack deflection/bridging is generally associated with R-curve behaviour, i.e. increase of fracture resistance with increasing crack length. The fracture toughness values determined in this study were calculated from maximum stress and notch depth. Crack deflection can lead to a small increase in the crack tip toughness, such as was determined in the studies of whisker-reinforced alumina by Rödel (1991) **(73)**, but mainly aids in setting up efficient crack bridges leading to R-curve behaviour **(74)**. Unreacted aluminium may lead to further ductile bridging, but this effect will be minimal due to the low amount of residual Al (up to 2.7 wt.%). Samples with residual Al (G 6 cBN + 25vol.% Al, G20 cBN + 20 vol.%Al and G20 cBN + 25vol.% Al) show a lower toughness because the amount of binder content between the grains for these materials has exceeded the limit (maximum 20vol.% shown in Figure 7.12) which leads to easier crack propagation between grains. G20 cBN + 25vol.%Al has the lowest fracture toughness and the highest amount of residual Al, showing that the effect of aluminium on the fracture toughness is not a major one.

At low binder content the grain size has a larger effect on the toughness, but at higher binder content it appears that there is no sensitivity to grain size and the binder starts controlling the toughness. Crack propagation is generally affected by the residual stress state in the material. In multi-phase materials with phases of different thermal expansion residual stresses always occur [(49)]. Internal stresses exist in all polycrystalline materials that include a secondary phase of different thermal expansion coefficient. The height of residual stresses and their local distribution is determined by the volume ratio of the two phases and their thermal and elastic constant. At cBN grain sizes of 6 – 20 µm and a binder content of 15 – 20vol.% the residual stresses are obviously in an optimum range with regard to fracture toughness. At low binder content there is more cBN-cBN contact and the material is more brittle. Increasing the amount of binder will provide more opportunities for crack deflection and prevent crack propagation, thus increasing the fracture toughness. Further consideration on fracture toughness, based on real and estimated flaw sizes will be made after discussions of strength and strength limiting flaws.

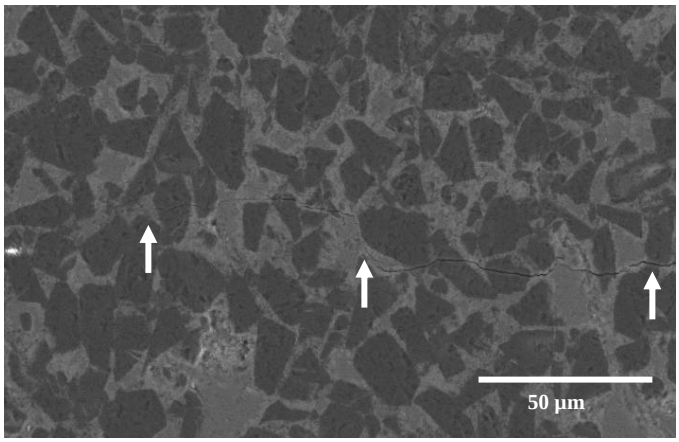

Figure 7. 9: Crack propagation in fracture toughness tests showing the fracture path on polished G20 cBN + 25 vol.% Al sample exhibiting slightly dominant crack propagation in the binder phase and transgranular fracture through the cBN phase.

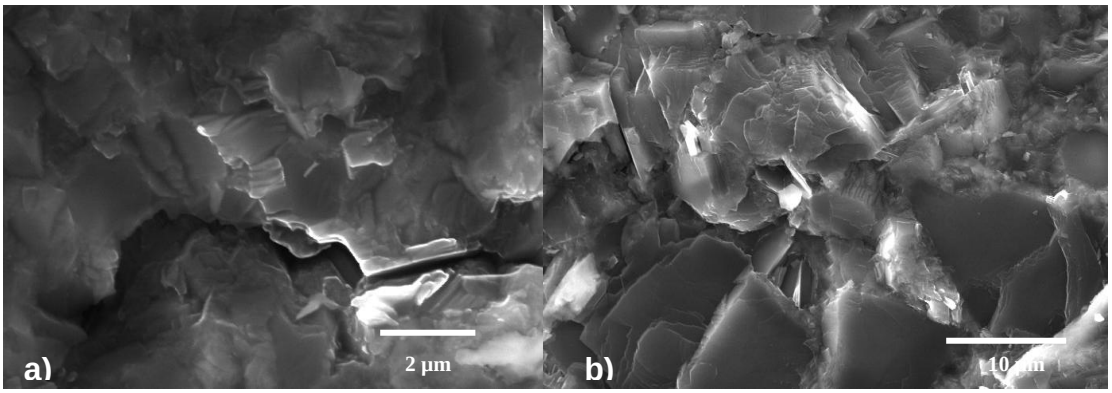

Figure 7. 10: Crack propagation in fracture toughness tests. Fracture surface of a) G2 cBN + 15 vol.% Al and b) G20 cBN + 25 vol.% Al, exhibiting mostly transgranular crack propagation in the cBN and binder phase.

The results of the fracture toughness measurements as a function of both the cBN grain size and the binder content are shown in Figure 7.11, while in Figure 7.12, the main effects of the hardness measurements are shown. It is clear that fracture toughness increases with increasing cBN grain size until 10 µm and then decreases, which suggests that 10 µm is the optimum grain size for toughening. The fracture toughness also increases with increasing binder content up until 20vol.% then

decrease below the 15vol.% level for the 25vol.% material, which suggests that 20vol.% binder is the maximum binder content; anything higher will result in a decrease in the fracture toughness.

The contributions of each effect on the fracture toughness were determined using a general linear model and the two-way ANOVA model, shown in Appendix J. The results from the two-way ANOVA model show that the grain size had a 27% effect on the fracture toughness and the binder content had 13%, which means that there was no clear dependence on the fracture toughness with both cBN grain size and binder content, although it does show that the grain size had a larger effect than the binder content. From the statistical results it can be deduced that the optimal composition for the fracture toughness would be G10 cBN and 20vol.% Al, although this theory could not be proved due to experimental time constraints.

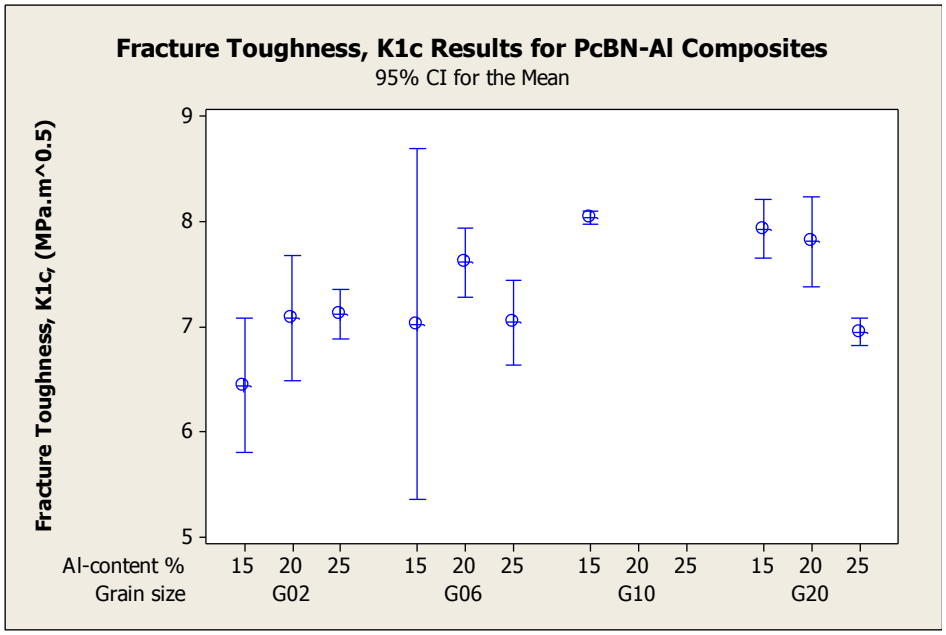

Figure 7. 11: Fracture toughness as a function of the cBN grain size and the binder content.

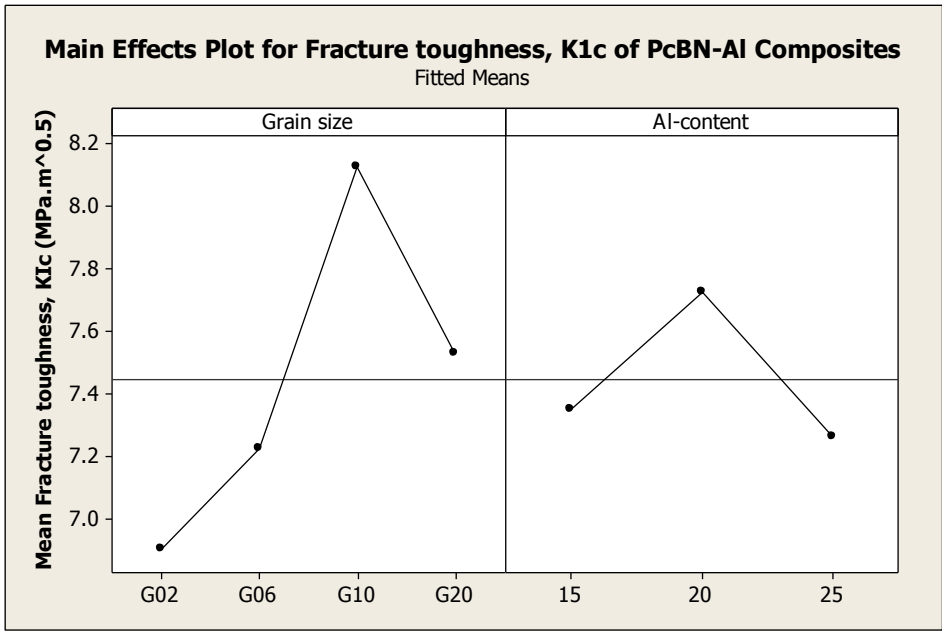

Figure 7. 12: Main effects plot of the fracture toughness with cBN grain size and Al content.

R-curve Behaviour

The results of the R-curve behaviour tests done using the Compact tension (CT) method described in Chapter 4.5.2.2 are shown in Chapter 6.3. Figure 7.13 and 7.14 show the R-curves of the PcBN-Al composite materials. The R-curve starts approximately at K_{IO}, which is the crack tip toughness (i.e. the onset of crack growth) **(69)** and extends with increasing crack length. Due to measurement errors it was difficult to determine the correct value of K_{IO} for each material. The K_{IO} was taken as the point in the data where constant crack growth resulted.

Sample data for the R-curve behaviour had a very low reproducibility; variability in the data could have been due to measurement errors as explained in Chapter 6.3.

Figure 7.13 shows the R-curves for the G2 and G6 PcBN-Al materials where the K_{IR} rises to between 3.8 and 9.1 MPa.m$^{1/2}$, these values being higher than the K_{Ic} for these materials. There was a large difference in the K_{IO} for the different materials of the G2 family of materials, the difference being attributed to errors in measurement. The K_{IR} for most of the samples was not the same for each material. The K_{IR} for the G2+15vol.%Al was between 5.1 – 8.7 MPa.m$^{1/2}$, the K_{IR} for the G2+20vol.%Al between 6.5 – 7.6 MPa.m$^{1/2}$ and the K_{IR} for the G2+25vol.%Al is between 5.5 – 6.5 MPa.m$^{1/2}$, shows that the material had no toughening before failure as it was below the K_{IC} values. The K_{IR} for the G6+15vol.%Al was between 3.8 - 7.6 MPa.m$^{1/2}$. It can also be seen that the second sample showed no rise in toughness. The K_{IR} for the

G6+20vol.%Al was between 5.8 – 8.3 MPa.m$^{1/2}$ and the K_{IR} for the G6+25vol.%Al 5.0 – 9.1 MPa.m$^{1/2}$.

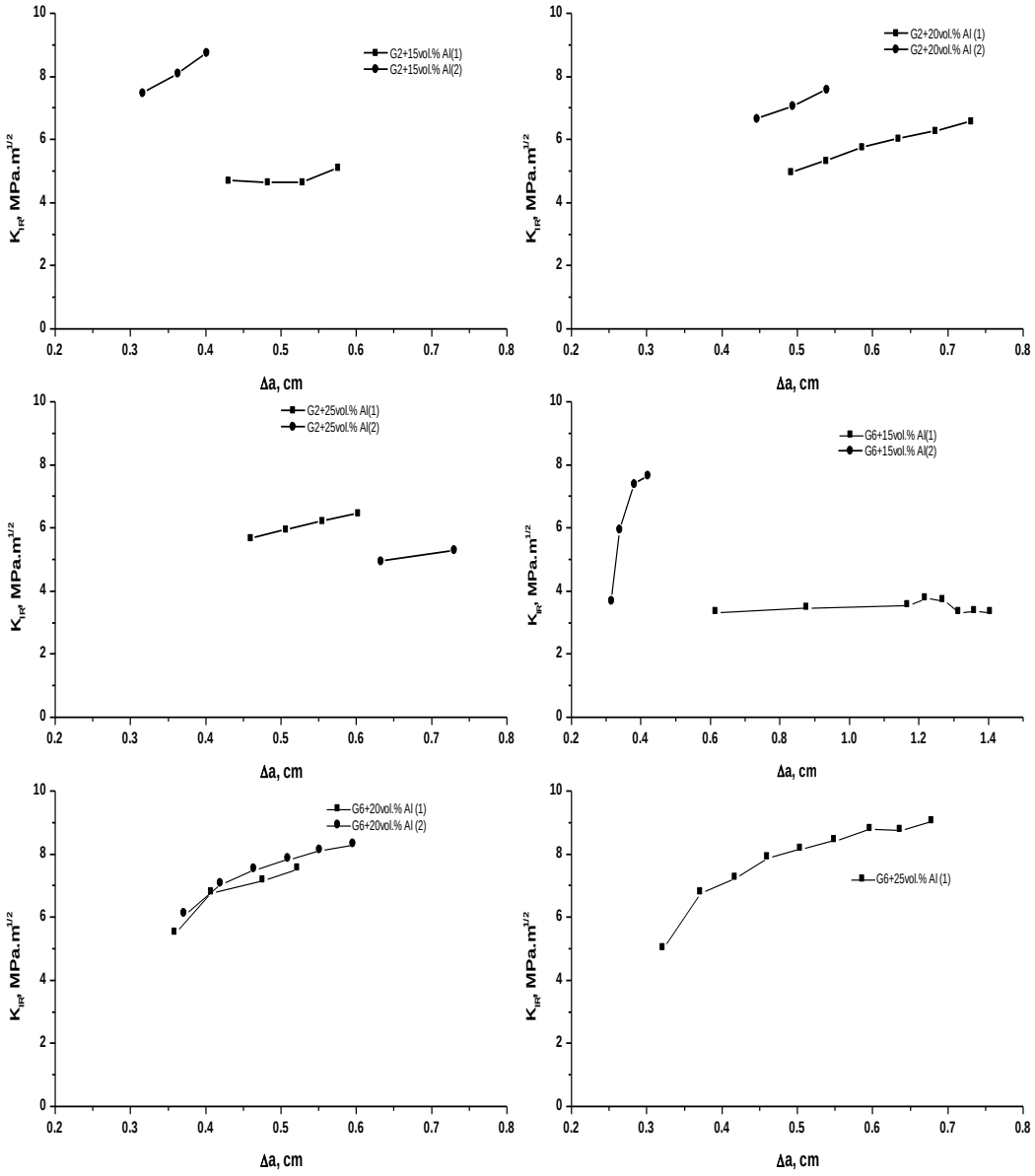

Figure 7. 13: R-curves of the G2 and G6 PcBN-Al composite materials.

Figure 7.14 shows the R-curves for the G10 and G20 PcBN-Al materials, the K_{IR} rises to between 5.3 and 9.5 MPa.m$^{1/2}$, these values are higher than the K_{Ic} for these materials. The K_{IR} for G10+15vol.%Al was 4.6 – 5.1 MPa.m$^{1/2}$, which shows that there was no toughening. While the K_{IR} for the G20+15vol.%Al was between 5.8 - 9.5 MPa.m$^{1/2}$, the K_{IR} for the G20+20vol.%Al between 4.8 - 9.0 MPa.m$^{1/2}$ and the K_{IR} for the G20+25vol.%Al 5.3 – 8.6 MPa.m$^{1/2}$.

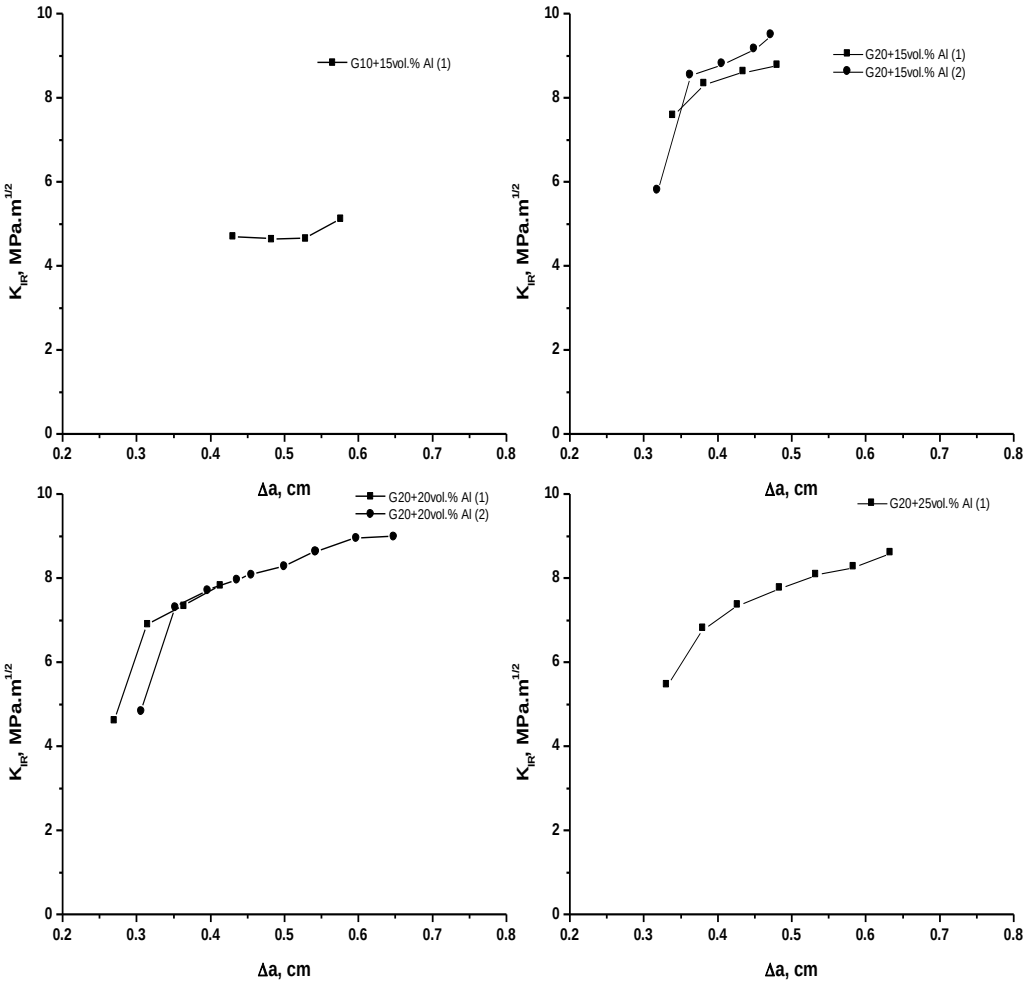

Figure 7. 14: R-curves of the G10 and G20 PcBN-Al composite materials.

Table 7.1 shows the comparisons between the K_{IC} and the K_{IR} values. It can be seen that the compared results show similar toughness values. There are a few exceptions such as G10 cBN + 15vol. % Al which has a lower K_{IR} value than the K_{IC} value or G6 cBN + 25vol.% Al has a lower K_{IC} value than K_{IR}. These discrepancies would have been a result of the errors explained in the beginning for the CT measurements. Although it does show that samples with a small amount of unreacted Al left in the material (e.g. G6 cBN + 25 vol.% Al, G20 cBN + 20 vol.% Al and G20 cBN + 25 vol.% Al) had a higher K_{IR} than K_{IC} values, this could suggest that unreacted Al will increase the R-curve behaviour of the material, but only for long crack lengths.

Table 7. 1: Comparison of K_{IC} and K_{IR} values for the PcBN-Al composite materials.

Sample	K_{IC} (MPa.m$^{1/2}$)	K_{IR} (MPa.m$^{1/2}$)
G2cBN15Al	6.4 ± 0.4	5.1 – 8.7
G2cBN20Al	7.1 ± 0.5	6.5 – 7.6
G2cBN25Al	7.1 ± 0.2	5.5 – 6.5
G6cBN15Al	7.6 ± 0.7	3.8 – 7.6
G6cBN20Al	7.6 ± 0.3	5.8 – 8.3
G6cBN25Al	7.0 ± 0.3	5.0 – 9.1
G10cBN15Al	8.0 ± 0.1	4.6 – 5.1
G20cBN15Al	7.9 ± 0.2	5.8 – 9.5
G20cBN20Al	7.8 ± 0.3	4.8 – 9.0
G20cBN25Al	6.9 ± 0.1	5.3 – 8.6

The R-curve behaviour of the PCBN-Al composites was compared with some common ceramic materials (Al_2O_3, Si_3N_4, SiC and ZrO_2). Table 7.2 shows the R-

curve results of these ceramic materials. Al_2O_3, Si_3N_4 and SiC have R – curves with K_{IR} between 2 – 9 MPa.$m^{1/2}$, while ZrO_2 doped materials have a K_{IR} between 5 – 16 MPa.$m^{1/2}$.

The increasing fracture toughness of Al_2O_3 was caused by crack tip shielding by microcracking and crack bridging and grain bridges **(70),** while Si_3N_4 exhibited crack bridging effects. The increase in fracture toughness of ZrO_2 ceramics was due to transformation toughening brought about by stresses around the crack tip due to the transformation from the tetragonal to the monoclinic form.

Table 7. 2: R-curve results of some common ceramics materials (41, 70).

Sample:	**K_{IR} (MPa.$m^{1/2}$)**	**K_{IC} (MPa.$m^{1/2}$)**
Al_2O_3 (depends on grain size)	2.3 – 7	3 – 4
Si_3N_4 (elongated grains)	5 – 11	4 – 7
SiC (elongated grains)	2 – 8	2 – 3
ZrO_2 (Mg, Ce doped)	5 – 16	7 – 10

There was a small amount of toughening over a small section of the measured samples, 0.2 – 0.8 cm extension, as can be seen in the R-curves. The slight rise in R-curve behaviour could be attributed to crack deflection, observed during crack propagation in the material. Crack deflection can also cause partial bridging by grains and secondary phase and is a prerequisite in the setting up of crack bridging effects **(68)**. Crack bridging and frictional grain bridging toughening mechanisms can also play a role in increasing the toughening mechanisms. Crack deflection/bridging are

generally associated with R-curve behaviour, i.e. increase of fracture toughness with increasing crack length.

The fracture toughness from the SEVNB and R-curve behaviour tests both show a slight toughening caused by crack deflection which as stated in the SEVNB fracture toughness section can lead to a small amount of crack tip toughness and thus assist in setting up crack bridging leading to R-curve behaviour. Unreacted aluminium can further lead to ductile bridging, thus increasing toughness. In the samples which contained the unreacted Al, the amount of binder was too high causing a deterioration of the properties. Frictional grain bridges also result in the toughening of the materials.

Transverse Rupture Strength

Chapter 6.4 shows the results of the transverse rupture strength tests. Table 6.5 gives the characteristic strength, Weibull modulus and 80% confidence intervals for the PcBN-Al composite materials. The strength ranges from 355 – 454 MPa. Strength values for commercially available PcBN cutting tools are in the region of about 600 - 800 MPa [(11)]. The strength values for the PcBN-Al composites are lower than those found in literature and for similar tool materials as shown in Table 7.3.

The range of the Weibull moduli between 6.1 - 24.9 is quite large. However, considering the strength distributions of the batches with low Weibull moduli more

closely, the strength data of these batches more or less clearly show signs of bimodal distributions (two different m slopes), whereas the strength data of the batches with high m values belong to monomodal distributions, see Figure 7.15. Figure 7.15a shows the two different m slopes for the G2 cBN +15vol.%Al and G6 cBN+15vol.%Al bimodal distribution. G6 cBN + 15vol.%Al shows a more pronounced bimodal distribution, exhibiting different fracture origins for the various m slopes. The differences in the fracture origins can be seen in the Fractography section: Figure 7.28 shows the fracture origins for the low and high strength distributions for the G2 cBN + 15vol.%Al samples; Figure 7.27a shows the fracture origin of a G6 cBN + 15vol.%Al sample with a high strength (binder phase) and Figure 7.29a and 7.30a shows the fracture origins of samples with a low strength (large pores) for the G6 cBN +15 vol.%Al samples. Therefore the statistical parameters σ_O and m of the batches with low m values need to be considered with caution.

Table 7. 3: Transverse rupture strength for commercially available cutting tool materials [76, 77].

Material:	**Transverse Rupture Strength (MPa)** **(3 point bend test)**
AMBORITE (AMB90)	664
AMBORITE (DBC50)	570
Polycrystalline diamond tools (PCD)	750 – 1000
WC-Co tools	1000 – 2500

Figure 7.16 – 7.18 shows the Weibull plots for the 15, 20 and 25 vol.% binder materials respectively. These results show the probability for each material to fail.

Refer to Appendix H for the full range of characteristic strength and Weibull moduli for various confidence intervals.

Figure 7.16 shows that the G 10 cBN + 15vol.% Al material had the highest strength values and the least amount of scatter, while G 6 cBN + 15vol.% Al had the highest amount of scatter which could have been due to its bimodal distribution. This suggests that the strength results were low and the material could have contained a high amount of flaws in this material. Both G 10 and G 20 cBN + 15vol.% Al materials had very little scatter and corresponding graphs were relatively straight.

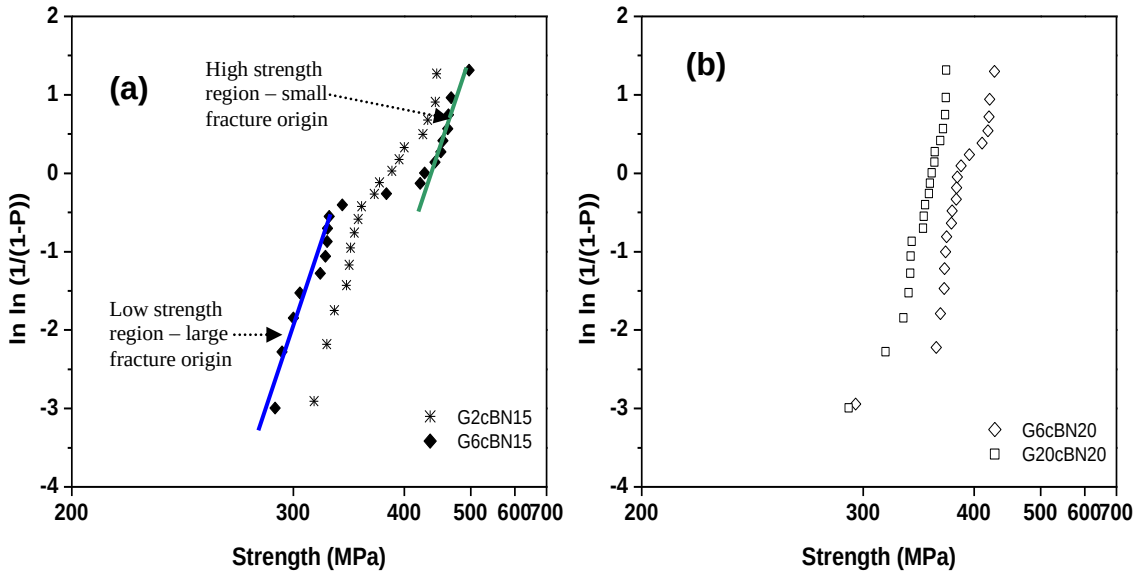

Figure 7. 15: Weibull distributions of bending strength data (a) showing more or less signs of bimodal distributions, batches G2 cBN+15vol.%Al, G6cBN+15vol.%Al (b) showing monomodal distributions of the batches G6cBN+20vol.%Al and G20cBN+15vol.%Al with Weibull moduli of 15 and 25.

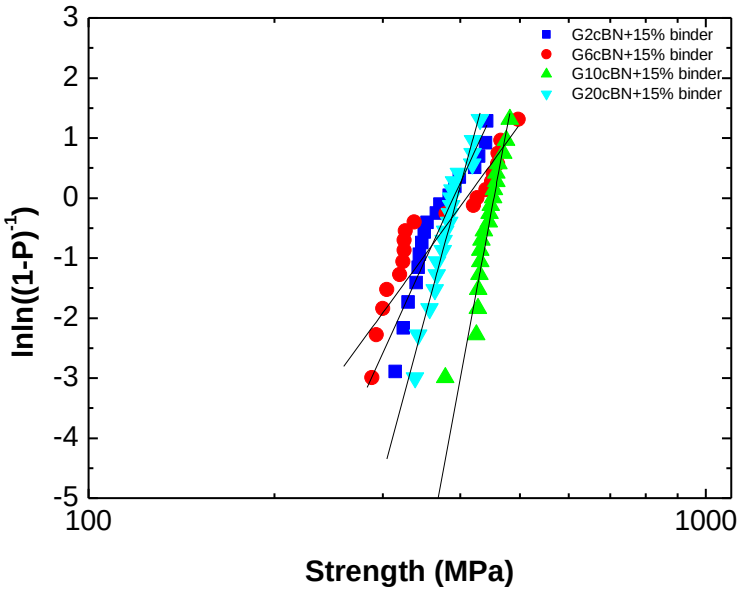

Figure 7. 16: Weibull plots of the 15 vol.% binder PcBN-Al composite materials.

Figure 7.17 shows that G 20 cBN + 20vol.% Al had the lowest strength values and lowest amount of scatter. G 2 cBN + 20vol.% Al materials had a high amount of scatter and the highest strength values also showing a bimodal distribution, while G 6 cBN + 20vol.% Al had a moderate amount of scatter. Figure 7.18 shows that there was a very low amount of scatter for the 3 materials made with 25% Al. G 20 cBN has the lowest strength values, G 2 cBN + 25vol.% Al had the highest strength values and G 6 cBN + 25vol.% Al had the least amount of scatter.

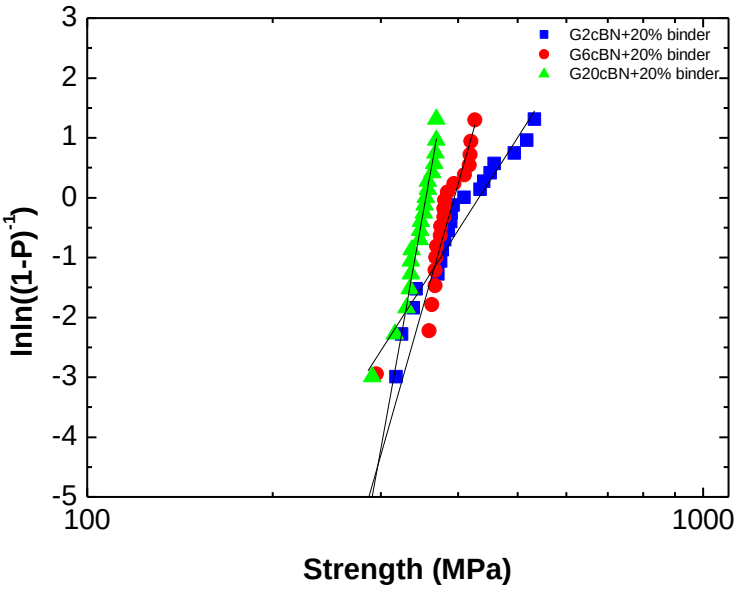

Figure 7. 17: Weibull plots of the 20 vol.% binder PcBN-Al composite materials.

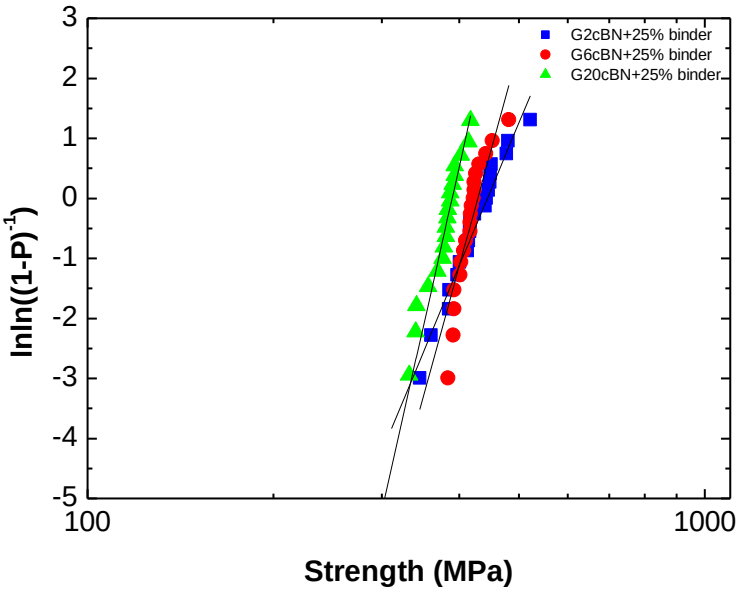

Figure 7. 18: Weibull plots of the 25vol.% binder PcBN-Al composite materials.

Figure 7.19 and 7.20 show the variation of the characteristic strength values of the PcBN composite materials as a function of the grain size of the cBN phase and binder content with 80% confidence intervals. The strength generally decreased with increasing grain size. It was observed that both the 20 and 25vol.% Al composites had characteristic strength values which decreased with increasing grain size. This decrease with grain size is a common feature for most ceramics [(74)] and is related to the size of the initial flaw which is related to the grain size [(75)]. With the 15vol.% Al there was no clear trend. Also there were no clear trends of strength dependence on binder content. The increase in binder content increased the strength of the G2 cBN, while for G6 and G20 cBN the strength decreased to a minimum at 20 vol.% and then increased.

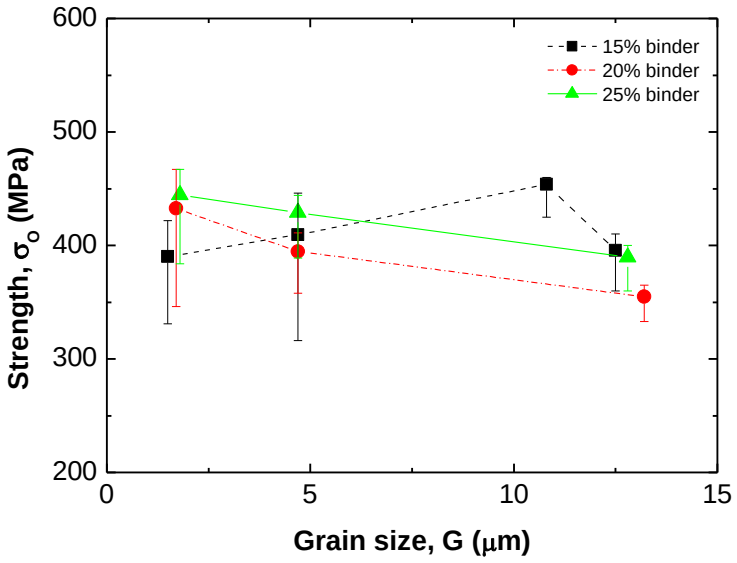

Figure 7. 19: Characteristic strength plot of the PcBN-Al composite materials with cBN grain size. Error bars show the 80% confidence intervals.

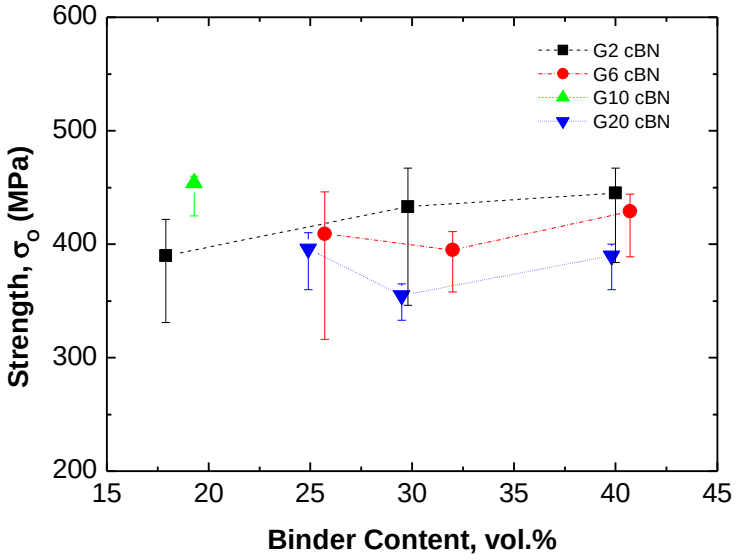

Figure 7. 20: Characteristic strength plot of the PcBN-Al composite materials with binder %. Error bars show the 80% confidence intervals.

The results of the strength measurements as a function of both the cBN grain size and the binder content are shown in Figure 7.21, while in Figure 7.22, the main effects of the hardness measurements are shown. Figures 7.21 and 7.22 reveal the strength increased with increasing binder content, except for the G20, while there is no clear trend with grain size.

The contributions of each effect on the strength were determined using a general linear model and the Two-way ANOVA model, shown in Appendix J. The results of the two-way ANOVA model showed that the grain size had a 9% effect on the strength and the binder content had a 10%, which means that there was only a weak dependence of the strength on either cBN grain size or binder content.

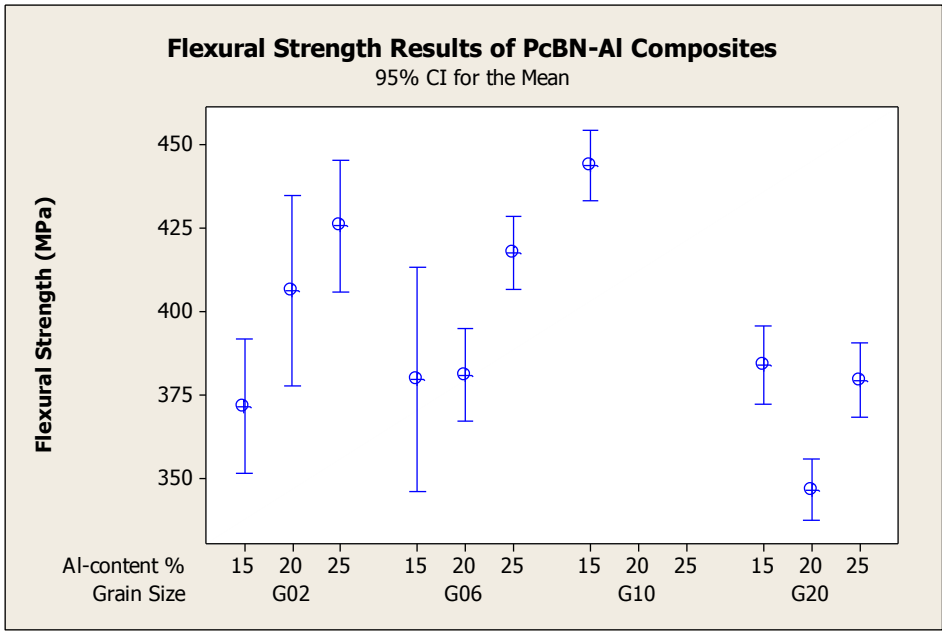

Figure 7. 21: Flexural Strength as a function of the cBN grain size and the binder content.

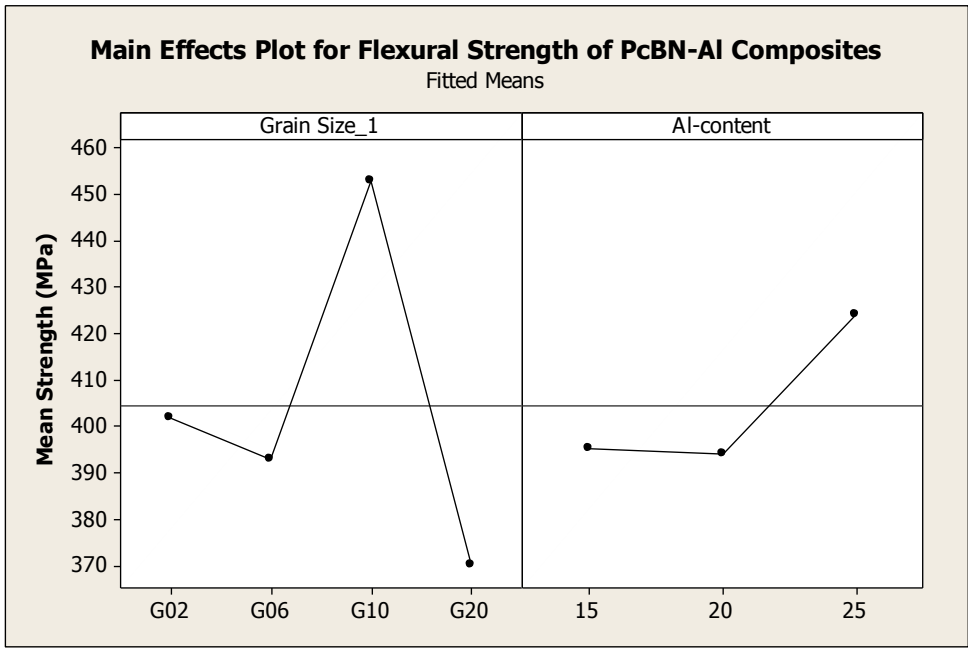

Figure 7. 22: Main effects plot of the flexural strength with cBN grain Size and Al content.

Comparisons of the hardness, fracture toughness and strength results with each other were also done. This was done in order to determine whether there were any correlations between each of the properties. Figure 7.23 – 7.25 show the correlations between the tested mechanical properties with grain size and binder content.

Figure 7.23 shows the correlation between fracture toughness and hardness. For the G20 samples the fracture toughness increased with increasing hardness, while for the G2 samples the fracture toughness decreased with increasing hardness. There was no real correlation between fracture toughness and hardness dependence on binder content, although there was a slight increase in the fracture toughness with increasing hardness for 25vol.%, while there was a decrease in fracture toughness with increasing hardness for 20vol.% binder. This suggests that the materials with the highest hardness have the lowest K_{IC}.

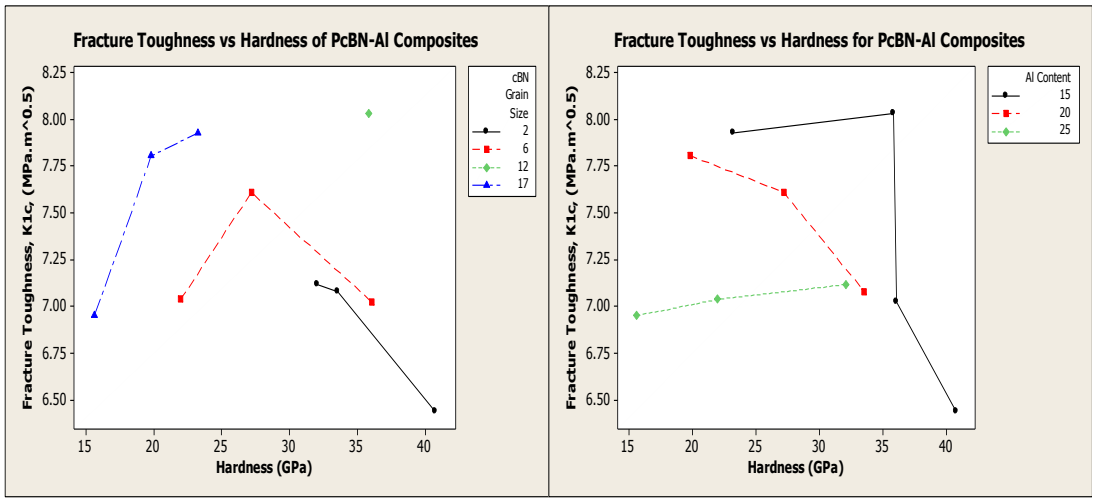

Figure 7. 23: Comparisons between the fracture toughness and hardness, and their dependence on grain size and binder content.

Figure 7.24 shows that there was no correlation between strength and hardness dependence on grain size, except at G2, where the strength decreased with increasing hardness. Strength increased with increasing hardness for both the 20 and 25vol.% binder content. Figure 7.25 shows that there was no trend in the strength and fracture toughness comparisons with both dependence on grain size and binder content, although for G2 strength increased with increasing fracture toughness. The strength for 20 vol.% binder decreased with increasing fracture toughness, while for 25vol.% binder the strength increased with increasing fracture toughness.

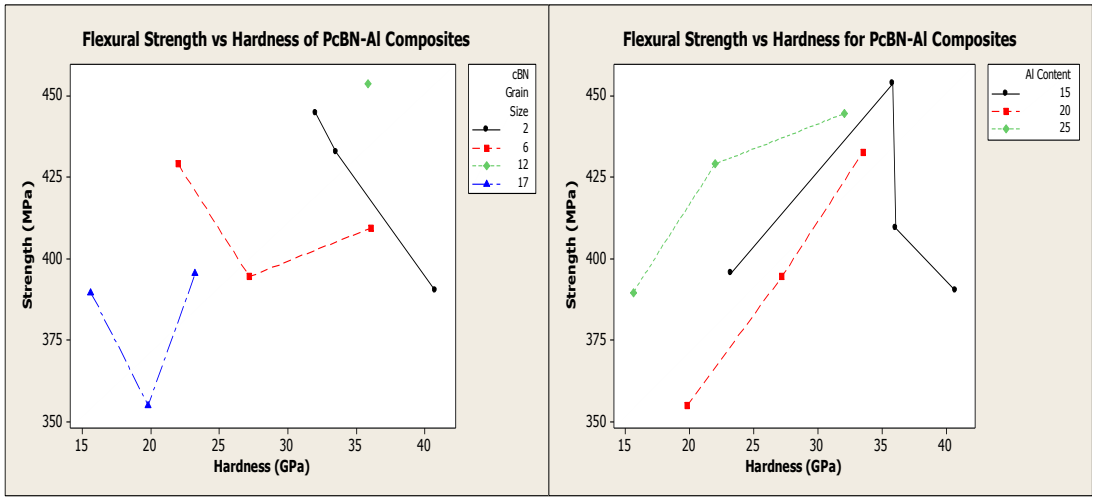

Figure 7. 24: Comparisons between strength and hardness, depending on grain size and binder content.

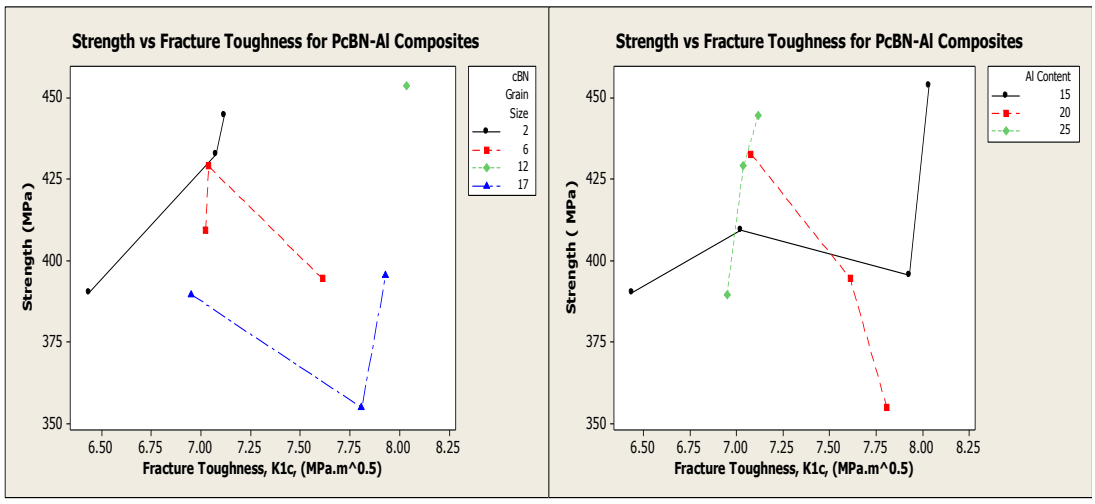

Figure 7. 25: Comparisons between strength and fracture toughness, depending on grain size and binder content.

Fractography

It has been well established that strength depends on the size, shape and surface finish of the specimens i.e. the flaw distribution in the material. It is thus important to determine the size, shape and type of the flaws present in the material. This will help to determine the failure behaviour of the material and to determine strategies for its improvement.

The flaw size of the various materials can be estimated using the Griffiths equation (equation 3.1 in Chapter 3) relating the strength and fracture toughness of the material to the flaw size of failure. Based on the fracture toughness, K_{Ic}, the size of a crack initiating flaw can be calculated for a definite strength value σ_f according to [(32)]

$$a = \left(\frac{K_{Ic}}{\sigma_f \cdot Y} \right)^2 , \qquad Y = \sqrt{\pi} / 2 \ , \ a \ = \text{radius of flaw}$$

This can be used to determine whether the results obtained from the strength and fracture toughness measurements are in the correct range by comparing them with the results of the actual flaw size measured by microscopy. The size of the flaws in each material will be determined using optical microscopes or scanning electron microscopes to determine the accuracy of the estimated results.

Using equation 3.1 and the strength and fracture toughness data, an estimation of the flaw size can be made (refer to Appendix I). The estimated average flaw size for each material calculated from both the average strength values and the measured flaw size is given in Table 7.4. The results show the flaw sizes for the PcBN-Al composite materials in the range between 300 - 650 μm.

Crack initiating flaws were representative of 10 - 15 % of the tested specimens of each batch, from specimens of low, medium or high strengths. The reason for this was that only 10-15% of the samples were fractographically examined. In most cases the crack initiating flaws were clearly identified. As far as they were identified the flaws were quite big, of 100 – 500 μm maximum diameter (Figure 7.26). These large flaws were responsible for the low strength measured. Based on the Griffith's equation, 3.1, the comparison between the size of the calculated cracks and crack

initiating flaws shows a close agreement, Figure 7.27. This clearly affirms the fracture toughness values tested by the SEVNB tests.

The initiating flaws were elongated in an aspect ratio from 1.5 to 5, as shown in the examples in Figure 7.26, the largest diameter always oriented perpendicularly to the specimen length. They either exposed features of ductile rupture or contained very large grains of the binder phase (either AlN or AlB_2), sometimes showing features of powder granules not fully sintered together. These characteristics were observed irrespective of the location of the flaws, in the bulk or at the tensile surface of the specimens. They clearly pointed to deficiencies in the powder processing. The flaws exhibiting ductile fracture obviously originated from big particles or agglomerates of unreacted Al binder as proven by EDX analysis.

Table 7. 4: The estimated average flaw size, characteristic strength and SEVNB fracture toughness for the PcBN-Al composite materials.

Sample	Estimate Flaw Size (µm)	Measured Flaw Size (µm)
G2 cBN + 15% Al	382	100 – 400
G2 cBN + 20% Al	386	100 – 420
G2 cBN + 25% Al	356	85 – 280
G6 cBN + 15% Al	505	200 – 490
G6 cBN + 20% Al	506	200 – 500
G6 cBN + 25% Al	361	140 – 400
G10 cBN + 15% Al	417	200 – 420
G20 cBN + 15% Al	543	150 – 300
G20 cBN + 20% Al	646	200 – 370
G20 cBN + 25% Al	427	100 – 250

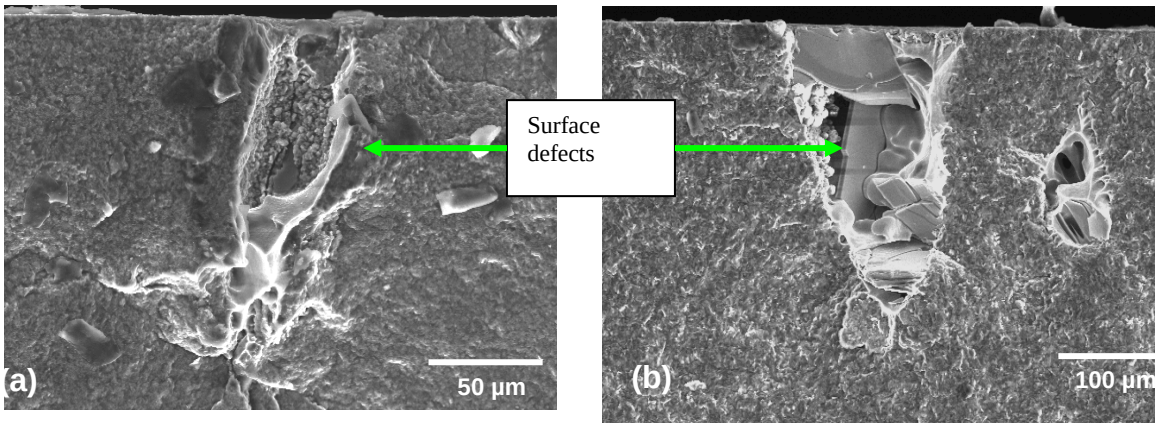

Figure 7. 26: Typical flaws (a) with features of ductile fracture, sample from batch G2cBN+15vol.%Al, (b) with very large grains of binder phase, sample from batch G6cBN+20vol.%Al.

The microstructure and size of the flaws indicate poor deagglomeration and homogenization of cBN and the binder powder during powder processing. The high aspect ratio and parallel orientated of the flaws point out that they originate before the hot pressing step and underscored the attribution to powder processing.

The poor correlation of strength and cBN grain size and binder content was mainly due to the very broad scatter of flaw sizes and poor correlation to the processing of the individual material batches. A more complete characterisation of the size and nature of the crack initiating flaws might elucidate the flaw size distribution of the individual materials and thus allow a better correlation of strength and material microstructure. However, the effort of such investigations is probably not appropriate at the current state of processing.

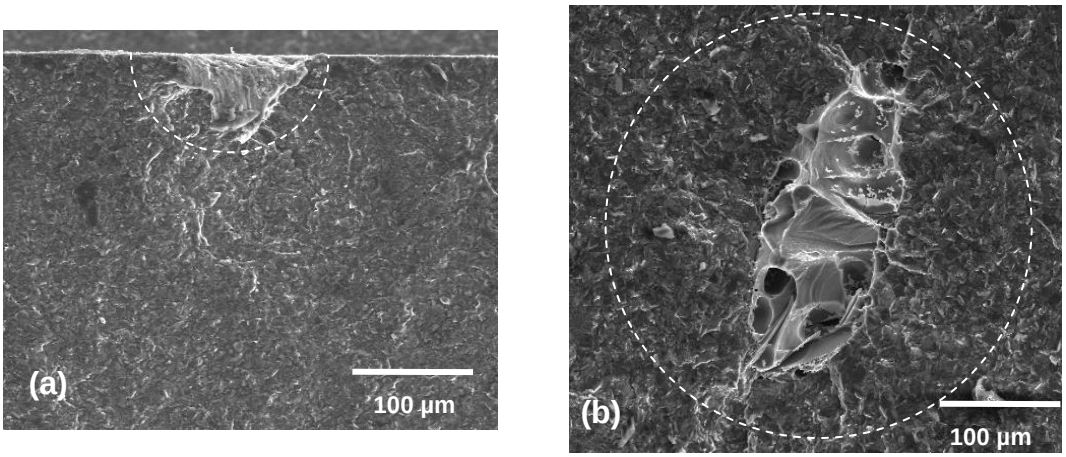

Figure 7. 27: Model crack size calculated from fracture toughness and strength limiting flaws; (a) G6cBN+15vol.%Al, and (b) G10cBN+15vol.%Al.

As mentioned in the discussion G2 cBN +15vol.%Al and G6 cBN +15 vol.%Al had bimodal strength distribution (see Figure 7.15). Figure 7.28 shows the flaw origins of the low and high strength distribution regions for the G2 cBN +15vol.%Al sample. Figure 7.27a, 7.30b and 7.31a show G6 cBN + 15vol.%Al samples with high strength. The results show flaw size and type differences between the samples in the low and high strength distribution regions within the samples materials showing bimodality. At low strength regions there were very large flaws mainly characterized by large surface defects (pores or large binder pools). While in the high strength distribution regions the flaws are smaller and were characterized by defects near the surface (binder pools or pores). The bimodality of these materials indicated that better processing technology was needed.

Figure 7.26a and b, Figure 7.28a and Figure 7.29 show flaws from materials with low strength, flaws that are mainly large surface defects containing large cBN grains or

binder pools, while Figure 7.27b and 7.30 show flaws from materials with high strength. The flaws consist mainly of smaller binder pools and pores.

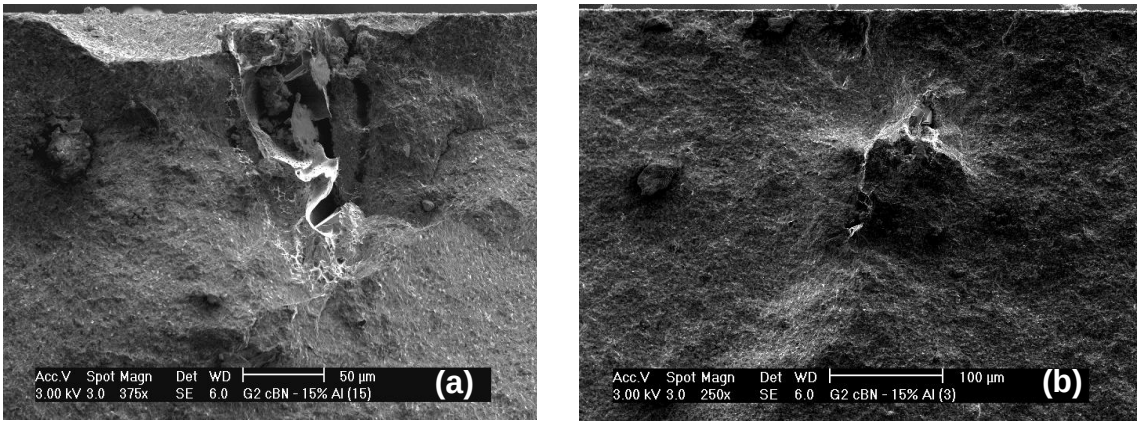

Figure 7. 28: Flaws in G2 cBN +15vol.%Al composite: a) large surface flaw resulting in low strength and b) small binder flaw resulting in high strength.

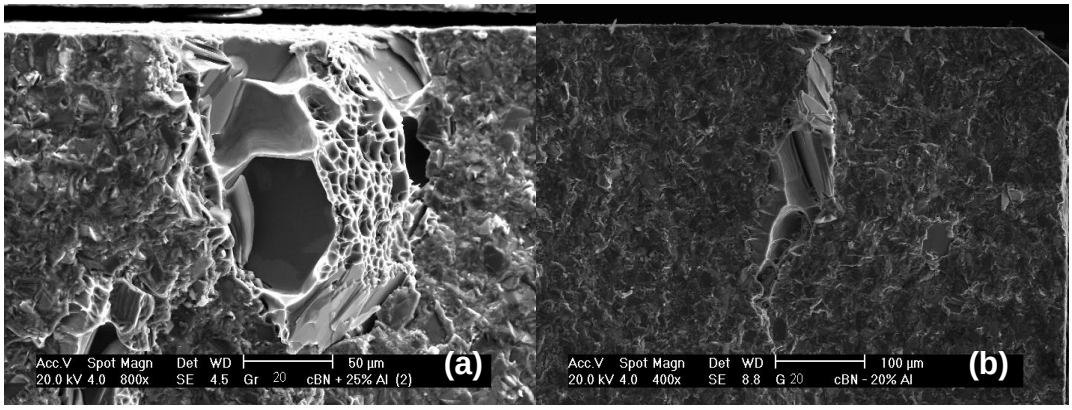

Figure 7. 29: Flaws from materials with low strength, a) G20 cBN+25vol.%Al showing large surface defect with large cBN grain and b) G20+20vol.%Al showing binder surface defect.

Figure 7.31 shows SEM images of internal cracking in the PcBN-Al composite materials indicating high internal stresses in the material. Figure 7.26 and 7.33 show

images of the failure originating flaws of some of the PCBN-Al composites. The flaw sizes in the materials were quite large (100-500 µm), confirming the lower strength values. Various flaw types were evident in the composite materials; large surface flaws can be seen in Figure 7.26 and 7.28a; flaws containing large cBN grains can be seen in Figure 7.32a.

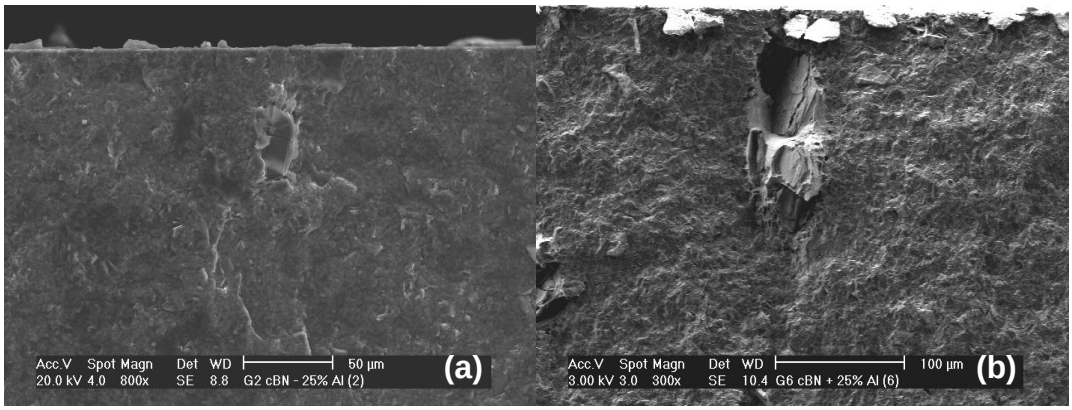

Figure 7. 30: Flaws from materials with high strength, a) G2 cBN+25vol.%Al showing a smaller binder pool and b) G6cBN+25vol.%Al showing a small pore.

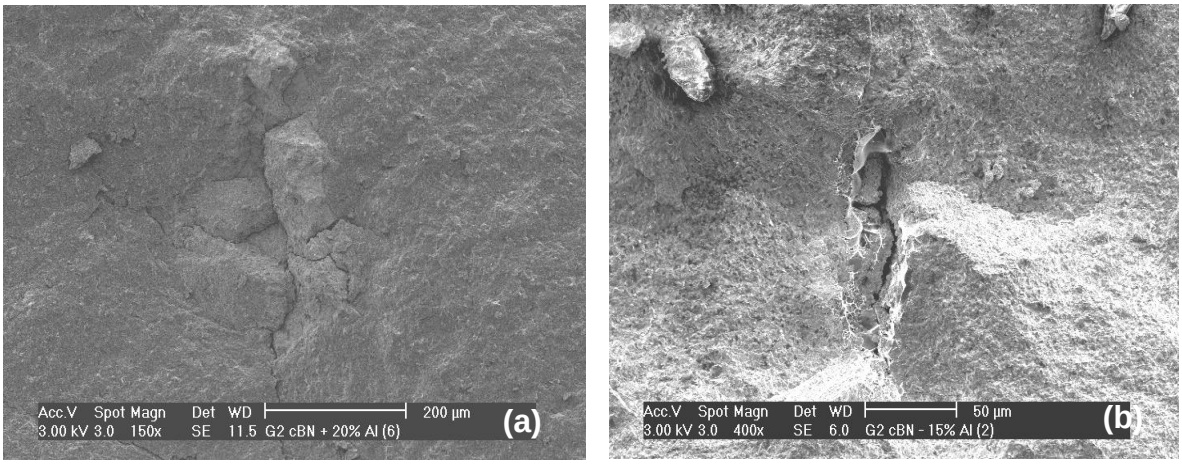

Figure 7. 31: SEM images of internal cracking in the PcBN-Al composite materials; a) G2 cBN + 20vol.% Al and b) G2 cBN + 15vol.% Al.

Figures 7.32b and 7.33a and b show flaws containing large pores surrounded by binder phase. Figure 7.32c shows a large binder pool consisting of a brittle oxide. EDS shows an oxidized layer on Al in binder phase, (Figures 7.32 c and d,) which could have come from oxidation of the aluminium powder before sintering.

Flaws consisting of larger binder pools are evident in Figure 7.33 d and e. These binder pools also consisted of smaller pores. The appearance of ductile dimple ruptures can be seen in Figures 7.30 a and 7.32 a, b and Figure 7.33 signifying plastic deformation around the edges due to small amounts of free Aluminium within the binder phase found through EDS analysis.

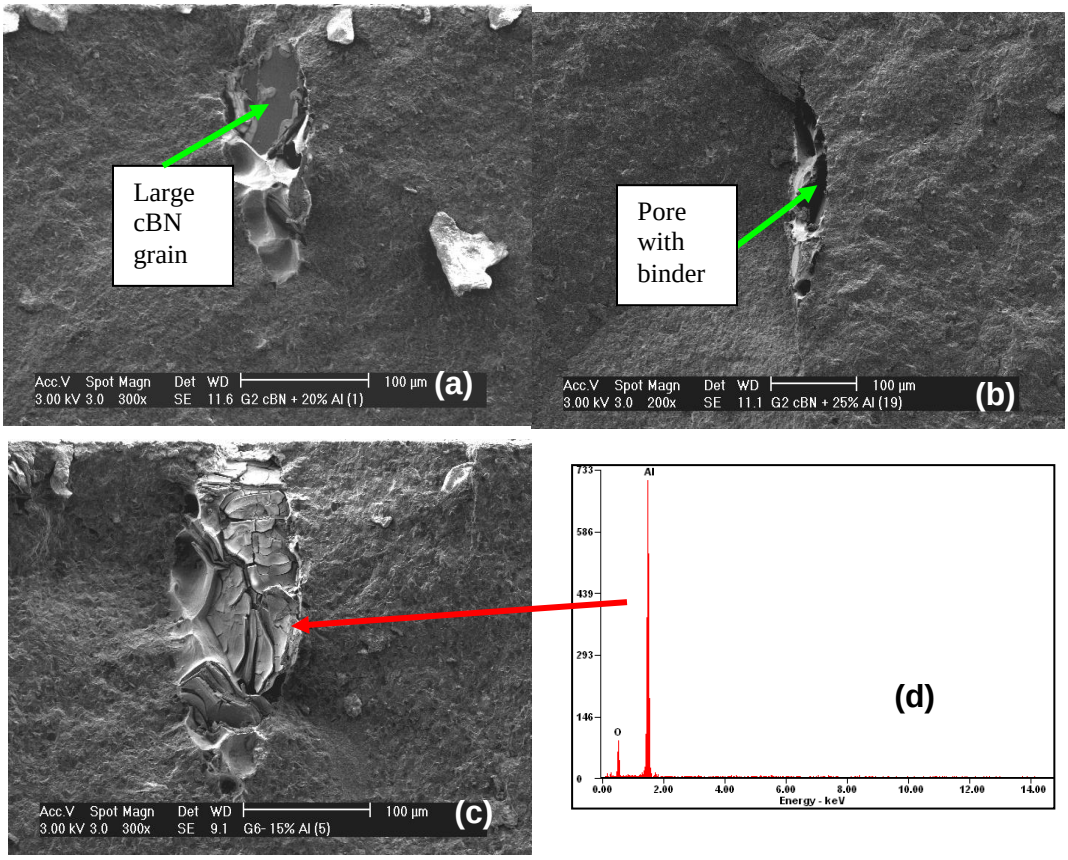

Figure 7. 32: SEM images of various types and sizes of flaws in the PcBN-Al composite materials; a) large grain; b) elongation of binder with pore; c) larger binder pool with oxidized brittle layer and d) EDS showing O and Al.

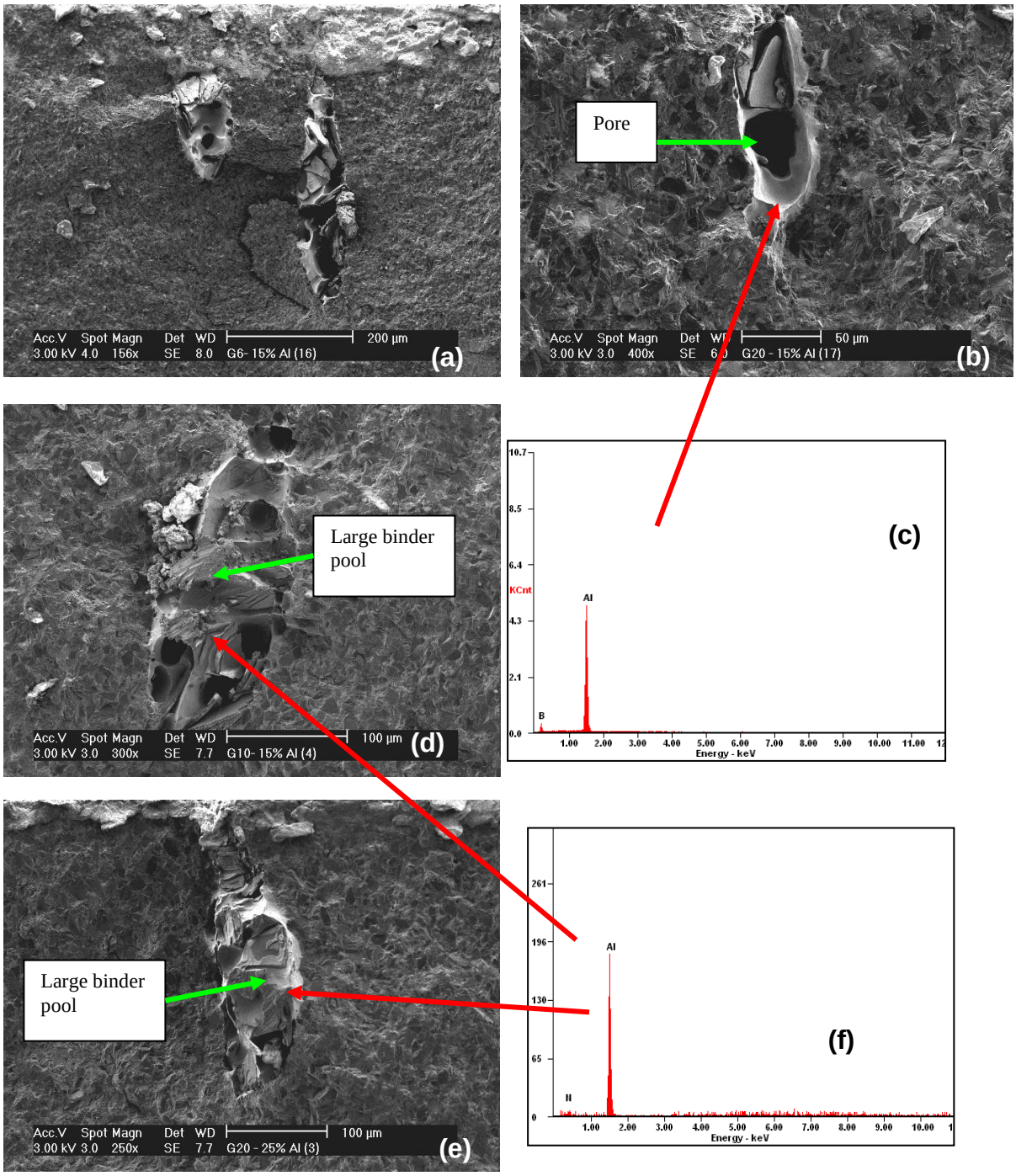

Figure 7. 33: SEM images of various types and sizes of flaws in the PcBN-Al composite materials; a and b) binder pool with pore; c) EDS showing ductile Al; d and e) larger brittle binder pool; and f) EDS showing binder is AlN.

Chapter 8: Conclusion

A study into the mechanical properties of PcBN-Al materials was conducted in this project. Materials of high content cBN with an Aluminium binder phase were sintered using High Pressure High Temperature methods. The grain size and binder content were varied to determine the effects each parameter had on the mechanical properties. These materials were fully densified and contained residual binder consisting of AlN and AlB_2. Some unreacted aluminium was also found in some of the samples with large amount of additives.

The PcBN-Al composite materials made and tested in this study reveal the following in respect of the structure to properties relationships:

The hardness of the PcBN materials prepared with Al binder is high as expected due to the hard cBN phase. It decreases with increasing cBN grain size and increasing binder content. From the statistical analysis of the hardness data, the grains size of the cBN particles has a larger effect on the hardness than the binder phase. For an optimum material in reference to hardness, a small cBN grain size and low binder phase content should be used.

Fracture toughness is high compared with other PcBN materials [2,11]. Fracture toughness also depends on grain size and binder content, but to a much lesser extent

than hardness and with less clear tendencies. Contrary to the hardness, high values of the fracture toughness are associated with larger grain sizes and medium binder content (20 vol.%).

The cracks propagate mostly through the binder; there are signs of crack deflection and crack bridging, as well as grain bridging. Crack deflection may be associated with residual stresses in the constituent phases. The high fracture toughness values are in good correlation with the observed sizes of fracture origins and the corresponding strength values.

R-curve behaviour was found, but the data scatters strongly. Crack deflection, grain bridging and crack bridging caused toughening in the materials. Unreacted aluminium in samples with high binder content (up to 2.7 wt.%) can act as a ductile bridging phase, but despite this possible additional toughening mechanism these samples showed low fracture toughness.

Strength values are low compared to literature values for commercially available PcBN cutting tools. They show no clear dependence on grain size and binder content. This is due to very large strength limiting flaws (100-500μm) in the materials. These large flaws prevent us from accurately determining the effect of the grain size and binder content on the strength.

Fractography showed that the materials consisted of various types of flaws, the flaws varying between large binder pools to small pores surrounded by large binder segregations. Some flaws exposed features of ductile rupture (presumably due to unreacted aluminium in the materials) or contained large grains some of which showed features of powder granules not fully sintered together. Surface defects were also found. The largest flaws were the large binder pools that were formed due to the agglomeration of powder particles that had not been properly distributed in the system. These flaws originated from poor powder processing, i.e. poor deagglomeration and homogenization.

Better powder processing techniques need to be used to prevent agglomeration and to improve homogenization and to reduce the size of the binder pools which are the largest flaws leading to failure. The technique of attrition milling can be used to improve homogenization and deagglomeration. To achieve this however, it would be necessary to use non-water-based milling fluids with surfactants which would be impossible to burn-out prior to sintering.

Comparisons between each of the mechanical properties reveal little correlation between them.

References:

1. Walnsley, J.C. and Lang, A.R. A transmission electron microscope study of a cubic boron nitride-based compact material with AlN and AlB_2 binder phases, Journal of Materials Science, 22, (1987) pp. 4093.
2. Pipkin, N.J, Roberts, D.C and Wilson, W.I, Amborite – A remarkable new cutting material, Advances in Ultrahard Materials Applications Technology, Vol. 1, edited by Paul Daniel, DeBeers Industrial Diamond Division, Hornbeam Press limited, (1982), pp. 72 – 80.
3. Benko, E, et al, BN Sintered with Al: Microstructure and Hardness, Ceramics International, 23, (1997), pp. 89-91
4. Benko, E, et al, cBN-metal/metal nitride composites, Ceramics International, 26, (2000) pp. 639-644
5. Sumiya, H et al, Mechanical properties of high purity polycrystalline cBN synthesized by direct conversion sintering method, Journal of Material Science, 35, (2000), pp. 1181 – 1186.
6. Rong, X.Z. and Fukunaga, O. High-pressure sintering of cBN-TiN-Al composite for cutting tool application, Diamond and Related Materials, 11, (2002), pp. 280- 286
7. Harris, T.K,, Brookes, E.J, Taylor, C.J, The flow stress of PcBN cutting tool materials at high temperatures, International Journal of Refractory Metals and Hard Materials, 19 (2001), pp. 267 – 273.

8. Li, Y et al, Study of high-pressure sintering behaviour of cBN composites starting with cBN-Al mixtures, Journal of Materials Research, 23 (9), (2008), pp. 2366 – 2372
9. Pauleau, Y, Materials surface processing by direct energy techniques, European Materials Research Society, Elsevier Science and Technology, (2005), pp. 375.
10. Eichler, J and Lesniak, C, Boron nitride (BN) and BN composites for high-temperature applications, Journal of the European Ceramics Society, 28, (2008), pp. 1105 - 1109.
11. Riedel, R. Handbook of Ceramic Hard Materials, Wiley-VCH, 2002, Vol 2.
12. Casanova, C.A.M, et al, Experimental study of plastic deformation during sintering of cubic boron nitride compacts, Diamond and Related Materials, 8 (1999), pp. 1451 – 1454.
13. Crystal structure of Boron Nitride allotropes, Courtesy of Michigan University, Materials Science Department, www.eecs.umich.edu/USL/MaterialScience/MotivationBN.html
14. Wentorf, R. H., Jr., Journal of Chemical Physics, 26, (1957), pp. 956
15. Wentorf, R. H., Jr., Sintered Superhard Materials, Science, 208, (1980), pp. 880-812
16. Wada, T and Yamashita, N, Formation of cBN films by ion beam assisted deposition, Journal of Vacuum Science and Technology, A 10 (3), (1992), pp. 515 – 520.

17. Benko, E, et al, Microstructure and Hardness of cBN-Zr Composite, Journal of European Ceramics Society, 18, (1997), pp. 389-393.Benko, E, CBN-TiH_2 composites: chemical equilibria, microstructure and mechanical testing, Diamond and Related Materials, 6, (1997), pp. 1192-1197
18. Sithebe, H. S. L, The preparation and characterisation of cBN ceramics with Al-based binder phase, Thesis, University of the Witwatersrand, Johannesburg, South Africa, (2006).
19. Sithebe, H. S. L, McLachlan, D, Sigalas, I and Herrmann, M; Pressure infiltration of boron nitride performs with molten aluminium, Ceramics international, (2007), article in press.
20. Wentorf, R. H., Jr. and Rocco W. A, Method Converting Hexagonal BN into cubic BN, Japan. Patent Applied. No. 65392 (1972)
21. Wentorf, R. H., Jr., Synthesis of Cubic Form of Boron Nitride, Journal of Chemical Physics, vol. 34 (3), (1961), pp. 809-812
22. Hibbs L E, Jr, Wentorf, R H, Jr, Borazon and diamond compact tools, High Temperature – High Pressures, 6, (1974) pp. 409 – 413
23. Sumitomo Electric Industries, Ltd. patented (US Patent 4 334 063, 1982)
24. Hara, A. and Yazu, S. Sintered Cutting Tool and Manufacturing Process, Japan Patent Application Number 21633 (1979).
25. Yazu, S., Kohno, Y., Satu, S. and Hara, A. New cBN-TiN composite sintered under ultra high pressure, Sumitomo Electric Industries limited.

26. Rong, X.Z. and Fukunaga, O. Sintering of cubic boron nitride with added aluminium at high pressure and high temperatures, Transactions: Materials Research Society of Japan, 14B, (1994), pp. 1455.
27. Zhao, Yu-Cheng and Wang, Ming-Zhi, Cubic BN with Al under High Temperature and High Pressure, Chin. Phys. Lett., Vol. 24, No. 8, (2007), pp. 2412- 2414.
28. Rong, X.Z. and Fukunaga, O. Cubic BN-WC-Co composite sintered at high pressures and high temperatures, Diamond Film Technology, 3, (1993) pp. 65.
29. Morgiel, J and Benko, E, Microstructure of boron nitride sintered with titanium, Materials Letter, 25, (1995) pp .49-52
30. Wakatsuki M et al, Synthesis of Polycrystalline Cubic BN, Mater. Res. Bull. 7 (9), (1970), pp. 999 – 1004
31. Benko, E, et al, CBN-$TiSiC_2$ composites, Diamond and Related Materials, 13, (2004), pp. 521-525
32. Munz, D, What can we learn from R-curve Measurements? Journal of American Ceramics Society, 90[1], (2007), pp 1-15.
33. Types of Fracture modes of crack deformation, University of Santa Cruz, earth 150 lecture notes, http://ic.ucsc.edu/~casey/eart150/Lectures/Joints/joints.htm
34. Broek, D, Elementary Fracture Mechanics, 4th edition, (1986) Nijhof, The Hague
35. Hübner and Jillek, Subcritical crack extension and crack resistance in polycrystalline alumina, Journal of Materials Science, 11 (1976), pp.

36. Knehans and Steinbrech, Quantitative Correlation of Acoustic Emission to the Brittle Fracture of Porous Sintered Glass, Materials Science and Engineering, 61 (1983), pp. 17 – 22.
37. Evans, A.G and Marshall, D.B, Mechanical Behaviour of Ceramic Matrix Composites, In: Fibre Reinforce Ceramic Composites: Materials, Processing and Technology, edited by K.S. Mazdiyasni, Noyes Publications (1990), pp. 1 - 38
38. Sarkar, D, R-curve behaviour of Ti_3SiC_2, Ceramics International, 2006.
39. Evans, A.G, Perspective on the Development of High-Toughness Ceramics, Journal of American Ceramics Society, 73 [2] (1990) pp. 187 – 206
40. Meguid, S.A, Mechanics and Mechanisms of Toughening of Advanced Ceramics, Journal of Materials Processing Technology, 56, (1996), pp 978 – 989
41. Steinbrech, R.W, Toughening Mechanisms for Ceramic Materials, Journal of the European Ceramics Society, 10, (1992), pp. 131 – 142
42. Wang, Z.Y, et al, J-Integral analysis of PcBN tool crack propagation in hybrid machining of advanced materials, Journal of Manufacturing Processes, vol. 6 [2] (2004), pp. 196 – 200.
43. Lammer, A. Mechanical Properties of polycrystalline diamonds, Materials Science and Technology, 4, (1988), pp. 949 – 955.
44. Meiss, D and Rai, G, Fracture toughness and thermal resistance of polycrystalline diamond compacts, Materials Science and Engineering A, 209, (1996), pp. 270 – 276.

45. Huang, B. L, et al, Fracture toughness of Sintered Polycrystalline Diamond (PCD), Int. Conf. on Advanced Particulate Materials and Processes, 5th, (1997), pp. 431 – 438.
46. Hooper R.M and Brookes C.A, Microstructure and wear of cubic boron nitride aggregate tools. In: Almond AE, Brookes CA, Warren R, editors. Science of Hard materials. Institute of Physics Conference Series No 75. Bristol: Adam Hilger; 1986, pp. 907 – 917.
47. Hooper, RM, Guilliou, MO, Henshall, JL, Indentation studies of cBN-TiC Composites, J. Hard Mater, 2 (1991), pp. 223 – 231.
48. R. Rice, Hardness – Grain-Size Relationship in Ceramics, Journal of American Ceramics, Vol 77 [10], (1994), pp. 2539 – 2553
49. Rice, R.W, Effect of Stresses from Thermal expansion Anisotropy, Phase transformation and Second Phases on the Strength of Ceramics, Journal of American Ceramics Society, 63, (1979), pp 703 – 710.
50. Ishizaki, K; Yanai, T, Si_3N_4 Grain Boundary Reinforcement by SiC Nanocomposites, Silicates Industrials, 7-8 (1995), pp. 215 - 222.
51. Materials for High-temperature Semiconductor Devices, National Research Council (U.S.), Committee on Materials for High temperature semiconductor devices, Commission on Engineering and Technical Systems, National Academies Press, (1995), pp. 25.
52. Valley design Corp., Properties of Aluminium nitride substrates, http://www.edgepolishing.com/aluminum-nitride.htm

53. Sung-Tag Oh, et al, Effect of particle size distribution and mixing homogeneity on microstructure and strength of alumina/copper composites, NanoStructured Materials, vol. 10 [2] 1998, pp. 327 – 332.
54. Warren, R, Ceramic-Matrix Composites, Chapman Hall, New York, 2007, pp. 4-7, 66-69.
55. Gong, J et al, A comparison between Knoop and Vickers hardness of silicon nitride ceramics, Materials Letters, 56, (2002), pp. 941-944
56. ASTM C1327 -08: Standard Test Method Vickers Indentation Hardness of Advanced Ceramic Materials. Annual Book of ASTM Standards, American Society for Testing Materials, Pennsylvania (2008).
57. ASTM C1326 -08e1: Standard Test Method Knoop Indentation Hardness of Advanced Ceramic Materials. Annual Book of ASTM Standards, American Society for Testing Materials, Pennsylvania (2008).
58. ASTM C1421-09: Standard Test Method for Fracture Toughness of Advanced Ceramics at Ambient Temperatures. Annual Book of ASTM Standards, American Society for Testing Materials, Pennsylvania (2009)
59. Kübler, J, Fracture toughness of Ceramics using the SEVNB Method; Round Robin, VAMAS Report No. 37 (1999)
60. Moon, R, K, Bowman, Trumble, K and Rödel, R; A comparison of R-curves from SEVNB and SCF Fracture Toughness Tests Methods on Multi-layered Alumina-Zirconia Composites, Journal of the American Ceramics Society, 83 [2] (2000), pp. 445 – 447

61. Raddatz, O, Modeling of R-curve behaviour in Ceramic/metal Composites, Acta mater. Vol 46 [8] (1998), pp. 6381 – 6395.
62. ASTM C1161 - 02c: Standard Test Method for Flexural Strength of Advanced Ceramics at Ambient Temperature. Annual Book of ASTM Standards, American Society for Testing Materials, Pennsylvania (2002).
63. ISO 14704:2000 (2000): Fine ceramics (advanced ceramics, technical ceramics) Test methods for flexural strength of monolithic ceramics at room temperature.
64. Weibull, W, The Phenomenon of Rupture of Solids, Ingeniors Ventenskaps Akademien, No. 153 (1939)
65. ASTM standard C 1239 – 95: Standard Practice for reporting Uniaxial strength data and Estimating Weibull Distribution Parameters for Advanced Ceramics. Annual Book of ASTM Standards, American Society for Testing Materials, Pennsylvania (1995).
66. Basu, B et al, Is Weibull distribution the most appropriate statistical strength distribution for brittle material, Ceramics International, (2008), Article in press.
67. European Standard EN 843-5: Advanced Technical Ceramics – Monolithic Ceramics Mechanical Properties at Room Temperature – Part 5: Statistical evaluation of strength values, 1997.
68. Thoman, D.R, C.J. Bain, C.E. Antle, "Interferences on the parameters of the Weibull distribution," Technometrics, **11,** [3], (1969), pp. 445-460

69. Wachtman, J, Mechanical Properties of Ceramics, Wiley & Sons, (1996), pp.159 – 175, 357 –366.

70. Munz, D, Fett, T, Ceramics: Mechanical Properties, Failure Behaviour, Materials Selection, Springer, 1999, pp. 19-73

71. Thomaszewski, H, Boniecki, M and Weglarz, H, Effect of grain size on R-curve behaviour of alumina ceramics, Journal of the European Ceramics Society, **20** (2000), pp. 2569 – 2574.

72. Rödel, J, Fuller, Jr. E.R, and Lawn, B.R, "In-situ Observations of Toughening Processes in Alumina Reinforced with Silicon Carbide Whiskers", Journal of the American Ceramics Society, **74** [12] (1991) pp. 3154-3157.

73. Rödel, J, "Interaction Between Crack Deflection and Crack Bridging", Journal of the European Ceramics Society, **10** [3] (1992) pp.143-150.

74. Seidel, J. Claussen, N and Rödel, J, "Reliability of Alumina: Effect of Grain Size", Journal of the European Ceramics Society, **15** (1995) pp. 395-404.

75. A. Zimmermann, M. Hoffman, B. D. Flinn, R. K. Bordia, T. Chuang, E. R. Fuller Jr. and J. Rödel, "Fracture of Alumina with Controlled Pores", Journal of the American Ceramics Society, **81** [9] (1998) pp. 2449–2457.

76. Element Six (Pty) Ltd, Private Correspondence, Mr J. Reid.

77. Drozda, T, Tool and manufacturing engineers handbook, Society of Manufacturing Engineers, Vol. 1, 4th edition, (1983), chapter 3, pp. 19

Appendices:

Appendix A: Rietveld Analysis

The percentages associated with each plot are for crystalline materials only. Any amorphous materials present could significantly alter the validity of these results. The results have been calculated based on a simple analytical peak shape model – this could be improved but would most likely not be worthwhile based on the amount of effort required.

Rietveld refinement was done using Topas A version 4.1 and Structural models used were taken from the ICSD - version 1.4.4. Powder X-ray diffraction data were collected using a Bruker AXS D8 equipped with a primary beam Göbel mirror, a radial Soller slit, a VÅntec-1 detector and using Cu-K_α radiation (40kV, 40mA). Data were collected in the 2θ range 5 to 100° in 0.021° steps, using a scan speed resulting in an equivalent counting time of 73.2 s per step.

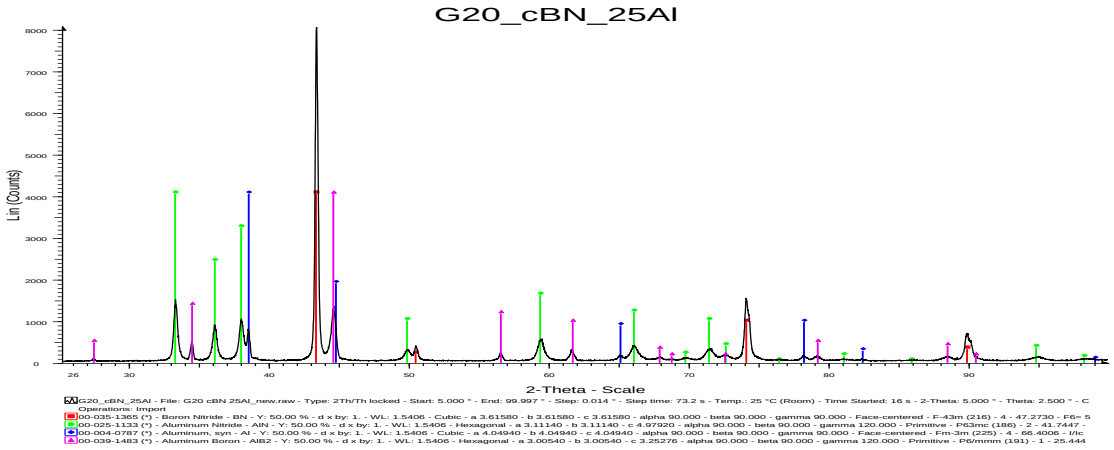

Figure A 1: XRD scan of G20 cBN +25 vol.% Al showing various phases.

Rieveld refinement shown in Figure A2- A4 shows that there is approximately 1.28 wt.% Al in G6 cBN + 25 vol.% Al sample, 1.05 wt.% in G20 cBN + 20vol.%Al

and 2.73wt.% in G20 cBN + 25vol.%Al samples.

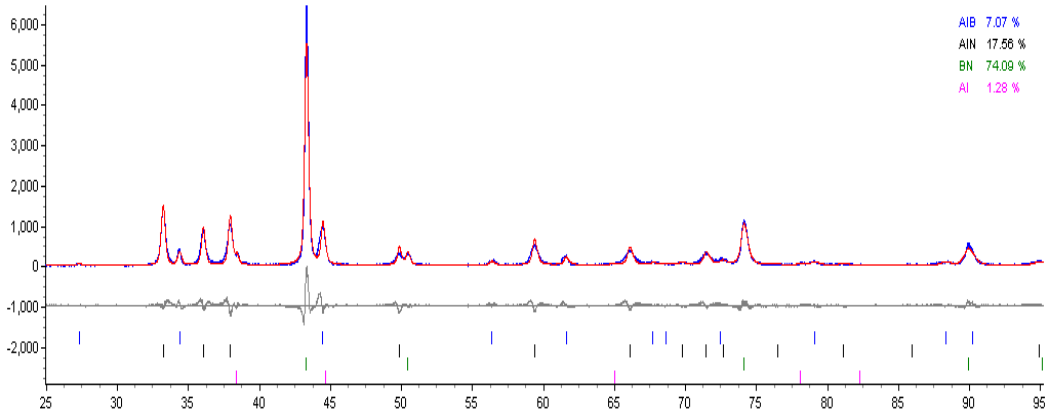

Figure A 2: Rietveld analysis of G6 cBN + 25vol.% Al.

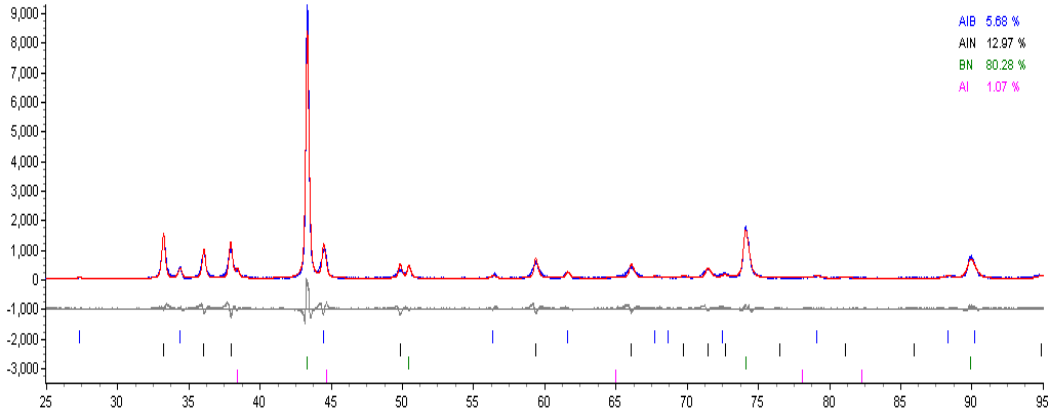

Figure A 3: Rietveld analysis of G20 cBN + 20vol.% Al.

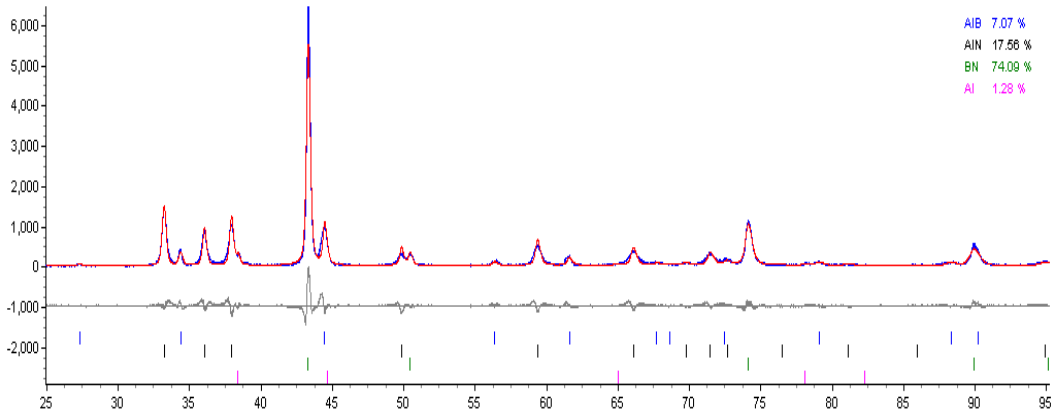

Figure A 4: Rietveld analysis of G20 cBN + 25vol.% Al.

Appendix B: Determination of the Grain Size and Binder Phase Composition using Image Analysis Tools

Image analysis techniques have been used to quantify and characterise the microstructure of the sintered PCBN-Al composite materials. The microstructures of the sintered materials were looked at in a Phillips-ESEM XL30 and 10 SEM micrographs of the microstructure were taken. The magnification of the micrographs depended on the size of the cBN materials; a high magnification was used for G2 and G6 materials while a low magnification was used for G10 and G20. The micrographs represented the average microstructure for each material.

Using image analysis software program (AnalySIS "Pro") the grain size and the percentage of the binder and cBN phases were determined. The method used to determine the percentage of the phases was by measuring the area of light intensity of the different phases. The cBN phase shows a darker intensity than the binder phase.

The grain size and grain size distribution was determined by measuring the grain size for each grain and calculating the distribution. The data from the AnalySIS program was then processed automatically by using Mathcad and Mathconnex programs. The program module was designed to calculate the grain size distribution and mean free path of both the cBN and binder phase for the PcBN materials.

Grain Size and Composition of the Sintered Materials:

The grain size and composition of the various PcBN-Al composite materials are shown in tables B 1-8. The volume percentage of the cBN and binder phase with standard deviation of the various PcBN-Al composite materials are shown in tables B 1, 3, 5 and 7. The grain size distribution and mean free path (MFP) of both the cBN grains and the binder phase for the various PcBN-Al composite materials are shown in tables B2, 4, 6 and 8.

Figures B 1-4 shows the modified SEM micrographs obtained from the AnalySIS program. These micrographs show colour differences in the cBN and binder phases and the various grain sizes. Figure B1a-f show the micrographs of the G2 cBN-Al composite materials. The grain size of the different composites can be seen in Figure B1a, c and e; the red and green phases show the different grain sizes while the black phase shows the binder phase. The phase composition is shown in Figure B1 b, d and f; the green phase is the cBN phase and the blue phase is the binder phase. A clear difference in the amount of binder phase can be seen. Similarly for Figures B2-4; although in Figure B2 b, d and f the cBN phase is shown in blue and the binder phase is green. The grain size images in Figures B3 and B4 show the larger cBN grain sizes in yellows and blues.

G2 cBN Materials:

Table B. 1: Phase composition of the G2 cBN-Al composite materials

	Volume % of Phases		
Material	**cBN**	**Binder**	**Standard deviation**
G2 cBN + 15%Al	82.12	17.88	1.45
G2 cBN + 20%Al	70.21	29.79	1.84
G2 cBN + 25%Al	60.02	39.98	1.65

Table B. 2: Grain size of the G2 cBN-Al composite materials

	G2-15	**G2-20**	**G2-25**
Mean cBN grain size (µm)	1.49	1.72	1.78
D10 (µm)	0.89	0.97	1.04
D50 (µm)	1.46	1.70	1.72
D90 (µm)	2.10	2.24	2.37
Maximum cBN grain size (µm)	2.79	3.30	3.21
cBN MFP (µm)	0.79	0.39	0.50
Standard deviation (µm)	0.90	0.71	0.81
Maximum cBN MFP (µm)	9.58	10.39	8.96
Binder pool size (µm)	0.78	1.29	1.90
Standard deviation (µm)	0.40	0.56	0.69
Maximum Binder pool size (µm)	2.14	3.12	4.70
Binder Mean Free Path (MFP) (µm)	0.21	0.26	0.36
Standard deviation (µm)	0.24	0.50	0.69

Maximum binder MFP (µm)	2.5	9.73	10.64

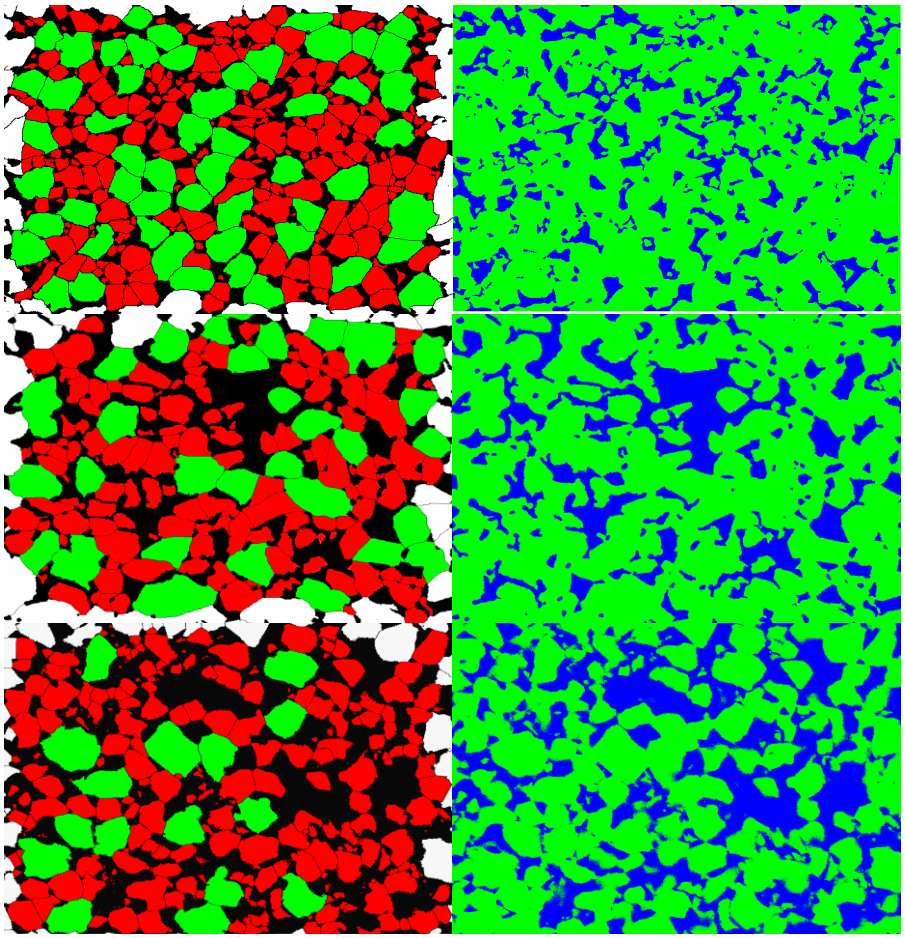

Figure B. 1: Modified SEM micrographs for the determination of grain size and phase composition of the G2 cBN-Al composite materials. a) G2 cBN + 15vol.% Al grain size and b) G2 cBN + 15vol.% Al phase composition; c) G2 cBN + 20vol.% Al grain size and d) G2 cBN + 20vol.% Al phase composition; e) G2 cBN + 25vol.% Al grain size and f) G2 cBN + 25vol.% Al phase composition.

G6 cBN Materials:

Table B. 3: Phase composition of the G6 cBN-Al composite caterials:

	Volume %		
Phases	**cBN**	**Binder**	**Standard deviation**
G6cBN+15%Al	74.25 %	25.75 %	1.89
G6cBN+20%Al	67.97 %	32.03 %	2.95
G6cBN+25%Al	59.29 %	40.71 %	4.13

Table B. 4: Grain size of the G6 cBN-Al composite materials:

	G6-15	G6-20	G6-25
Mean cBN grain size (µm)	4.68	4.73	4.72
D10 (µm)	2.62	2.57	2.9
D50 (µm)	4.73	4.9	4.93
D90 (µm)	6.44	6.41	5.98
Maximum cBN grain size (µm)	7.38	7.23	6.95
cBN MFP (µm)	1.56	1.59	1.88
Standard deviation (µm)	2.09	2.02	2.15
Maximum cBN MFP (µm)	17.58	17.84	19.18
Binder pool size (µm)	3.13	4.46	4.80
Standard deviation (µm)	1.18	1.53	1.75
Maximum Binder pool size (µm)	7.36	9.36	9.76
Binder Mean Free Path (MFP) (µm)	0.90	1.26	1.55
Standard deviation (µm)	1.2	1.77	2.11
Maximum binder MFP (µm)	13.22	18.73	19.18

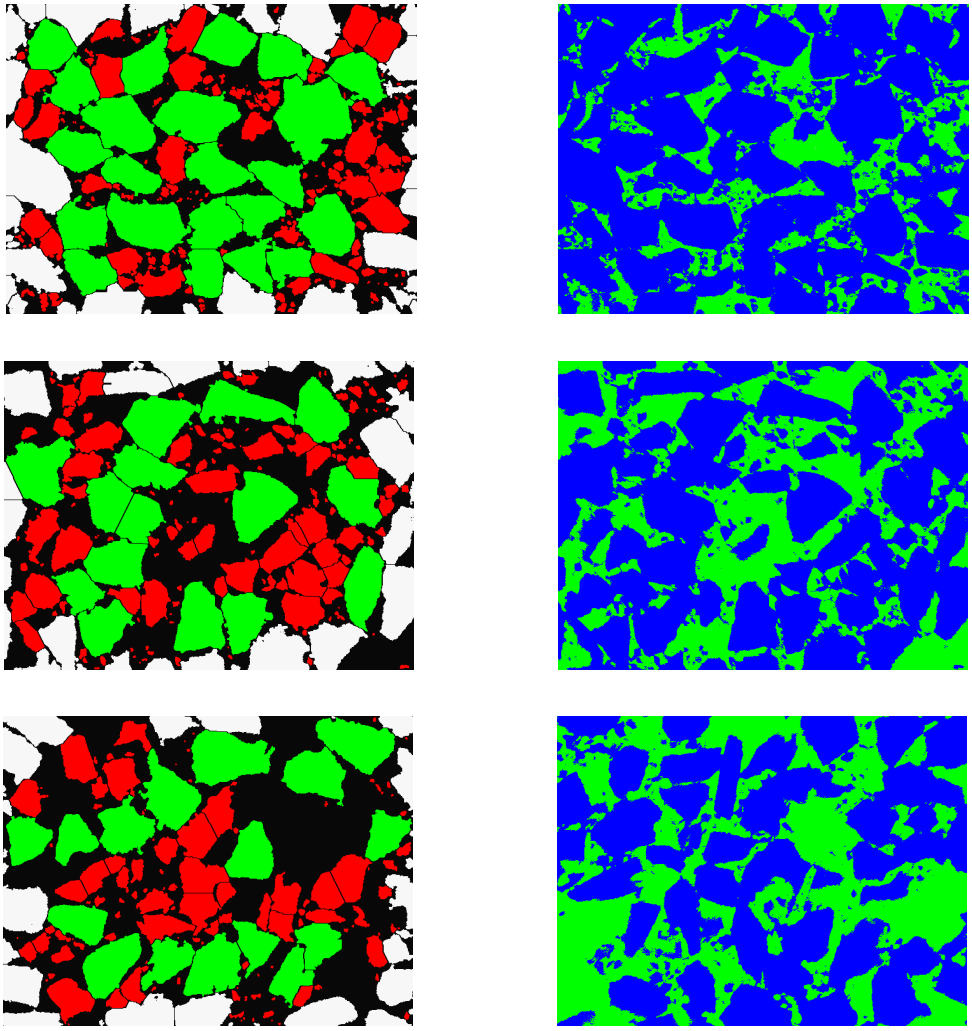

Figure B. 2: Modified SEM micrographs for the determination of grain size and phase composition of the G6 cBN-Al composite materials. a) G6 cBN + 15vol.% Al grain size and b) G6 cBN + 15vol.% Al phase composition; c) G6 cBN + 20vol.% Al grain size and d) G6 cBN + 20vol.% Al phase composition; e) G6 cBN + 25vol.% Al grain size and f) G6 cBN + 25vol.% Al phase composition.

G10 cBN Materials:

Table B. 5: Phase composition of the G10 cBN + 15%Al composite material:

	Volume %		
Phases	**cBN**	**Binder**	**Standard deviation**
G10cBN+15%Al	80.73 %	19.27 %	1.39

Table B. 6: Grain csze of the G10 cBN + 15%Al composite material:

	G10-15
Mean cBN grain size (µm)	10.79
D10 (µm)	5.90
D50 (µm)	10.96
D90 (µm)	14.86
Maximum cBN grain size (µm)	17.18
cBN MFP (µm)	2.85
Standard deviation (µm)	4.50
Maximum cBN MFP (µm)	47.34
Binder pool size (µm)	4.35
Standard deviation (µm)	1.45
Maximum Binder pool size (µm)	12.15
Binder Mean Free Path (MFP) (µm)	1.15
Standard deviation (µm)	1.61
Maximum binder MFP (µm)	20.09

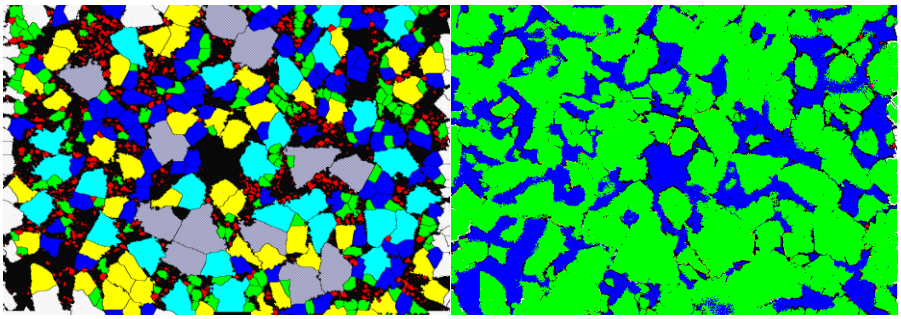

Figure B. 3: Modified SEM micrographs for the determination of grain size and phase composition of the G10 cBN-Al composite material. a) G10 cBN + 15vol.% Al grain size and b) G10 cBN + 15vol.% Al phase composition;

G20 cBN Materials:

Table B. 7: Phase omposition of the G20 cBN –Al composite materials:

	Volume %		
Phases	**cBN**	**Binder**	**Standard deviation**
G20cBN+15%Al	75.08%	24.92%	2.27%
G20cBN+20%Al	70.55%	29.45%	2.27%
G20cBN+25%Al	60.21%	39.79%	2.73%

Table B. 8: Grain size of the G20 cBN-Al composite materials:

	G20-15	G20-20	G20-25
Mean cBN grain size (µm)	12.52	13.25	12.76
D10 (µm)	5.05	5.12	5.48
D50 (µm)	12.27	13.20	12.88
D90 (µm)	18.72	18.93	18.81
Maximum cBN grain size (µm)	25.39	27.75	22.64
cBN MFP (µm)	4.81	5.25	5.46
Standard deviation (µm)	5.85	5.95	5.64
Maximum cBN MFP (µm)	54.09	63.53	48.90
Binder pool size (µm)	7.70	7.70	10.99
Standard deviation (µm)	3.14	3.14	4.31
Maximum Binder pool size (µm)	17.99	17.99	23.11
Binder Mean Free Path (MFP) (µm)	2.12	2.59	4.02
Standard deviation (µm)	2.39	3.02	4.66
Maximum binder MFP (µm)	25.03	32.15	43.39

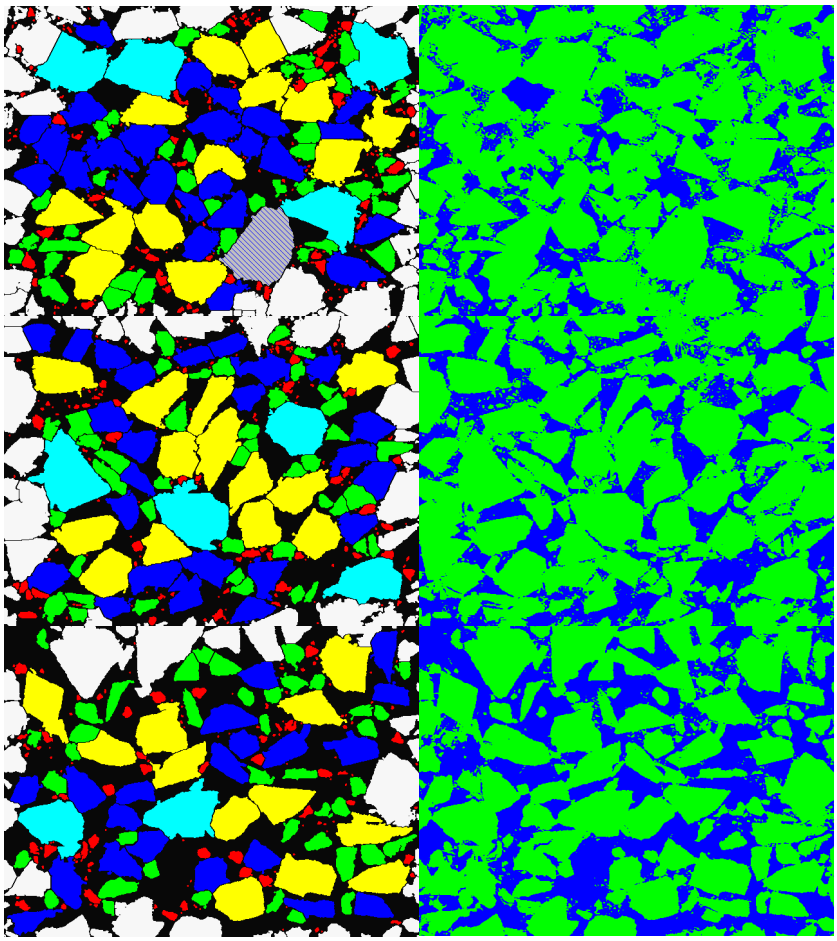

Figure B. 4: Modified SEM micrographs for the determination of grain size and phase composition of the G20 cBN-Al composite materials. a) G20 cBN + 15vol.% Al grain size and b) G20 cBN + 15vol.% Al phase composition; c) G20 cBN + 20vol.% Al grain size and d) G20 cBN + 20vol.% Al phase composition; e) G20 cBN + 25vol.% Al grain size and f) G20 cBN + 25vol.% Al phase composition.

Appendix C: Hardness Estimation

Using the assumption of the rule of volume mixtures, the hardness can be estimated for the materials also assuming that the major binder phase consists of AlN.

H_V = vol. % cBN x H_V (cBN) + vol. % AlN x H_V (AlN)

85% cBN
$H_V = 0.85 \times 45 + 0.15 \times 12$
$= 40.05$ GPa

80% cBN
$H_V = 0.80 \times 45 + 0.20 \times 12$
$= 38.4$ GPa

75% cBN
$H_V = 0.75 \times 45 + 0.25 \times 12$
$= 36.75$ GPa

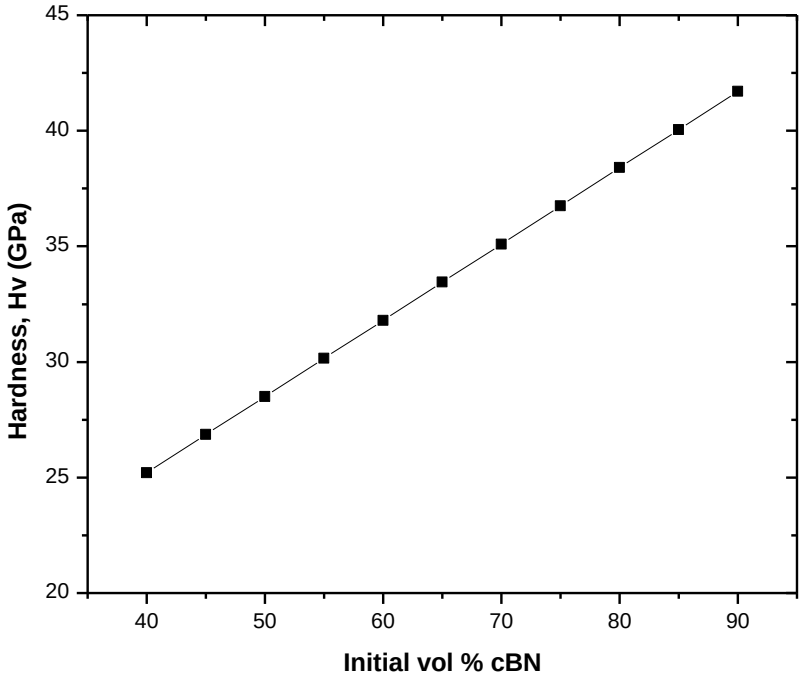

Figure C. 1: Hardness estimation with initial vol.% cBN.

Appendix D: Results of the Hardness Measurements

Table D shows the results of the Vickers Hardness measurements. The Hardness procedure is described in section 4.5.

Table D. 1: Results of the Vickers mardness measurements.

	Hardness, H_{V5} (GPa)									
Sample	**G2cBN+15%Al**	**G2cBN+20%Al**	**G2cBN+25%Al**	**G6cBN+15%Al**	**G6cBN+20%Al**	**G6cBN+25%Al**	**G10cBN+15%Al**	**G20cBN+15%Al**	**G20cBN+20%Al**	**G20cBN+25%Al**
1	42.07	32.38	31.19	34.29	27.51	21.78	37.68	26.03	21.66	15.54
2	41.18	34.97	32.38	34.29	27.51	20.51	31.68	24.44	21.20	16.17
3	39.48	32.38	33.64	37.12	27.51	21.00	36.38	21.86	20.26	15.34
4	42.07	33.64	29.00	37.12	26.58	24.75	37.88	22.16	18.46	15.96
5	38.67	34.29	30.62	36.38	27.04	22.21	35.67	23.25	19.08	15.65
6	40.31	34.79	33.64	37.12	27.04	21.84	32.43	21.53	18.04	15.14
7	41.08	33.81	33.00	37.42	26.82	20.50	36.53	21.59	18.40	15.28
8	41.08	32.02	33.00	34.70	27.57	23.43	38.47	25.05	21.50	16.02
9										
10										
Mean	**40.74**	**33.54**	**32.06**	**36.06**	**27.20**	**22.00**	**35.84**	**23.24**	**19.83**	**15.64**
std dev	**1.20**	**1.15**	**1.65**	**1.39**	**0.38**	**1.47**	**2.51**	**1.74**	**1.50**	**0.38**

Appendix E: Results of the SEVNB Fracture Toughness

The results of the Fracture toughness testing using the Single-edge V notch beam (SEVNB) method is shown the Tables E1-10. The fracture toughness procedure is described in Section 4.5. The fracture toughness K_{1c} is calculated using the following equations:

$$K_{Ic} = \sigma\sqrt{a}Y = \frac{F}{B\sqrt{W}} \cdot \frac{S_1 - S_2}{W} \cdot \frac{3\sqrt{\alpha}}{2(1-\alpha)^{1.5}} Y$$

$$Y = 1.9887 - 1.326\alpha - \frac{(3.49 - 0.68\alpha + 1.35\alpha^2)\alpha(1-\alpha)}{(1+\alpha)^2} \qquad \text{and} \qquad \alpha = \frac{a}{W}$$

Table E. 1: G2cBN+15%Al

Sample	a, µm	W, m	a/W	Load (F), N	B	i	J	k	Y	K_{1C} (MPa.m$^{0.5}$)
1	1305.39	0.00374	0.349	246.91	0.00305	1323746.4	2.674	1.687	1.099	6.565
2	1251.25	0.00372	0.336	256.22	0.00304	1381867.1	2.688	1.609	1.116	6.671
3	923.67	0.00398	0.232	324.13	0.00304	1690083.4	2.513	1.074	1.281	5.842
4	1064.30	0.00377	0.282	297.93	0.00302	1606717.5	2.653	1.311	1.195	6.674
									Mean	6.438
									Std dev	0.400

Table E. 2: G2cBN+20%Al

Sample	a, µm	W, m	a/W	Load (F), N	B	i	J	k	Y	K_{1C} (MPa.m$^{0.5}$)
1	1180.08	0.00410	0.288	374.47	0.0029	2016607	2.439	1.339	1.186	7.811
2	1155.08	0.00406	0.285	341.37	0.00289	1853807	2.463	1.322	1.191	7.191
3	978.28	0.00412	0.237	366.54	0.00286	1996650	2.427	1.098	1.271	6.763
4	987.97	0.00407	0.243	347.23	0.00289	1883312	2.457	1.122	1.262	6.547
5	971.09	0.00410	0.237	385.50	0.00289	2083201	2.439	1.095	1.272	7.079
									Mean	7.078
									Std dev	0.483

Table E. 3: G2cBN+25%Al

Sample	a, µm	W, m	a/W	Load (F), N	B	i	J	k	Y	K_{1C} (MPa.m$^{0.5}$)
1	973.20	0.00410	0.237	418.59	0.00303	2157528	2.439	1.097	1.271	7.342
2	960.70	0.00409	0.235	404.80	0.00303	2089000	2.445	1.086	1.276	7.079
3	1007.58	0.00410	0.246	380.67	0.00303	1962068	2.439	1.135	1.256	6.824
4	934.84	0.00411	0.227	420.83	0.00301	2180833	2.433	1.054	1.290	7.211
5	1027.34	0.00411	0.250	373.95	0.00287	2032396	2.433	1.155	1.249	7.129
									Mean	7.117
									Std dev	0.191

Table E. 4: G6cBN+15%Al

Sample	a, µm	W, m	a/W	Load (F), N	B	i	J	k	Y	K_{1C} (MPa.m$^{0.5}$)
1	1115.86	0.00411	0.271	369.47	0.00278	2073045	2.433	1.257	1.212	7.685
2	1004.30	0.00414	0.243	403.60	0.00276	2272676	2.415	1.121	1.262	7.764
3	1195.47	0.00408	0.293	369.98	0.00278	2083564	2.451	1.366	1.178	8.217
4	925.86	0.00407	0.227	343.78	0.00273	1973897	2.457	1.054	1.290	6.592
									Mean	7.564
									Std dev	0.690

Table E. 5: G6cBN+20%Al

Sample	a, µm	W, m	a/W	Load (F), N	B	i	J	k	Y	K_{1C} (MPa.m$^{0.5}$)
1	1093.97	0.00420	0.260	387.57	0.00277	2158949	2.381	1.204	1.231	7.614
2	1087.11	0.00422	0.258	396.87	0.00274	2229691	2.370	1.190	1.235	7.769
3	1077.11	0.00418	0.258	383.77	0.00275	2158508	2.392	1.191	1.235	7.595
4	1076.72	0.00422	0.255	408.59	0.00276	2278907	2.370	1.179	1.240	7.891
5	1117.11	0.00422	0.265	359.12	0.00273	2025002	2.370	1.224	1.223	7.186
									Mean	7.611
									Std dev	0.267

Table E. 6: G6cBN+25%Al

Sample	a, µm	W, m	a/W	Load (F), N	B	i	J	k	Y	K_{1C} (MPa.m$^{0.5}$)
1	1070.00	0.00411	0.260	350.33	0.00285	1917411	2.433	1.203	1.231	6.908
2	1099.30	0.00411	0.267	340.85	0.00286	1859003	2.433	1.237	1.219	6.821
3	1035.86	0.00411	0.252	366.54	0.00287	1992112	2.433	1.164	1.245	7.025
4	1040.63	0.00413	0.252	386.01	0.00285	2107576	2.421	1.164	1.245	7.395
									Mean	7.038
									Std dev	0.253

Table E. 7: G10cBN+15%Al

Sample	a, µm	W, m	a/W	Load (F), N	B	i	J	k	Y	K_{1C} (MPa.m$^{0.5}$)
1	1091.95	0.00408	0.268	380.84	0.00275	2168119	2.451	1.238	1.219	8.017
2	1051.88	0.00409	0.257	401.01	0.00279	2247446	2.445	1.188	1.236	8.071
3	1101.41	0.00418	0.263	396.70	0.00274	2239363	2.392	1.218	1.225	7.997
4	950.86	0.00408	0.233	416.35	0.00276	2361677	2.451	1.078	1.279	7.984
5	1071.41	0.00416	0.258	404.80	0.00274	2290580	2.404	1.190	1.236	8.095
									Mean	8.033
									Std dev	0.048

Table E. 8: G20cBN+15%Al

Sample	a, µm	W, m	a/W	Load (F), N	B	i	J	k	Y	K_{1C} (MPa.m$^{0.5}$)
1	1071.48	0.00415	0.258	406.70	0.00279	2262788	2.410	1.193	1.234	8.030
2	1068.36	0.00415	0.257	410.66	0.0028	2276688	2.410	1.189	1.236	8.063
3	1042.81	0.00414	0.252	389.12	0.002758	2192727	2.415	1.163	1.245	7.674
4	1059.61	0.00415	0.255	404.29	0.00278	2257453	2.410	1.179	1.239	7.952
									Mean	7.930
									Std dev	0.177

Table E. 9: G20cBN+20%Al

Sample	a, µm	W, m	a/W	Load (F), N	B	i	J	k	Y	K_{1C} (MPa.m$^{0.5}$)
1	1091.02	0.00416	0.262	368.78	0.00283	2020369	2.404	1.212	1.228	7.227
2	1094.94	0.00410	0.267	393.94	0.00287	2143678	2.439	1.235	1.219	7.877
3	1116.02	0.00406	0.275	374.98	0.00285	2064917	2.463	1.274	1.207	7.816
4	1310.86	0.00418	0.314	369.47	0.00288	1984238	2.392	1.477	1.148	8.046
5	1292.81	0.00418	0.309	369.64	0.00284	2013122	2.392	1.453	1.154	8.075
									Mean	7.808
									Std dev	0.343

Table E. 10: G20cBN+25%Al

Sample	a, µm	W, m	a/W	Load (F), N	B	i	J	k	Y	K_{1C} (MPa.m$^{0.5}$)
1	1205.23	0.00420	0.287	334.48	0.00286	1804567	2.381	1.335	1.187	6.809
2	1200.55	0.00418	0.287	345.51	0.00287	1862031	2.392	1.336	1.187	7.064
3	1097.19	0.00417	0.263	357.92	0.00288	1924517	2.398	1.216	1.226	6.883
4	1039.22	0.00416	0.250	373.95	0.00289	2006165	2.404	1.154	1.249	6.950
5	1042.50	0.00419	0.249	381.53	0.00287	2053724	2.387	1.149	1.251	7.045
									Mean	6.950
									Std dev	0.108

Appendix F: Results of the Compact Tension Measurements for Determining R-Curve Behaviour.

The results of the Compact tension measurements to determine the R-curve behaviour of the PcBN-Al composite material is shown in Tables F 1-10. The R-curve behaviour procedure is described in Section 4.5. The resistance toughness K_R is calculated using the equations below:

$$K_{IR} = \frac{F}{BW^{1/2}} f\left(\frac{c}{W}\right)$$

$$f\left(\frac{c}{W}\right) = \frac{\left(2+\frac{c}{W}\right)\left(0.886+4.64\left(\frac{c}{W}\right)-13.32\left(\frac{c}{W}\right)^2+14.72\left(\frac{c}{W}\right)^3-5.6\left(\frac{c}{W}\right)^4\right)}{\left(1-\frac{c}{W}\right)^{3/2}}$$

Table F. 1: G2cBN+15% Al

Sample	Length [mm]	Length, c [cm]	Δc (cm)	Load [N]	Load, P (kN)	*(c/W)*	*$P/(B.W^{0.5})$*	*f (c/W)*	K_R ($MPa.m^{0.5}$) (calc)
1	7.5	0.75	0	39.3	0.0393				
	11.304	1.1304	0.3804	39.1	0.0391	0.40	0.07	7.35	0.48
	11.797	1.1797	0.4297	367.1	0.3671	0.42	0.61	7.71	4.71
	12.321	1.2321	0.4821	343.5	0.3435	0.44	0.57	8.11	4.64
	12.783	1.2783	0.5283	329.1	0.3291	0.46	0.55	8.50	4.66
	13.254	1.3254	0.5754	344.2	0.3442	0.47	0.57	8.92	5.12
2	7.5	0.75	0	116.3	0.1163				
	10.286	1.0286	0.2786	115.5	0.1155	0.37	0.19	6.68	1.29
	10.662	1.0662	0.3162	646.5	0.6465	0.38	1.08	6.92	7.46
	11.13	1.113	0.363	673	0.673	0.40	1.12	7.23	8.11
	11.513	1.1513	0.4013	701	0.701	0.41	1.17	7.50	8.76

Table F. 2: G2cBN+20% Al

Sample	Length [mm]	Length, c [cm]	Δc (cm)	Load [N]	Load, P (kN)	*(c/W)*	*P/(B.W$^{0.5}$)*	*f (c/W)*	K_R (MPa.m$^{0.5}$) (calc)
1	7.5	0.75	0	60.9	0.0609				
	10.901	1.0901	0.3401	60.4	0.0604	0.39	0.10	7.08	0.71
	11.42	1.142	0.392	119.5	0.1195	0.41	0.20	7.43	1.48
	11.939	1.1939	0.4439	143.6	0.1436	0.43	0.24	7.81	1.87
	12.413	1.2413	0.4913	364.5	0.3645	0.44	0.61	8.19	4.97
	12.878	1.2878	0.5378	372.4	0.3724	0.46	0.62	8.58	5.32
	13.357	1.3357	0.5857	383.1	0.3831	0.48	0.64	9.01	5.76
	13.838	1.3838	0.6338	381.5	0.3815	0.49	0.64	9.49	6.03
	14.328	1.4328	0.6828	376.6	0.3766	0.51	0.63	10.02	6.29
	14.807	1.4807	0.7307	372.3	0.3723	0.53	0.62	10.58	6.57
2	7.5	0.75	0	151.1	0.1511				
	11.512	1.1512	0.4012	150.4	0.1504	0.41	0.25	7.50	1.88
	11.966	1.1966	0.4466	510.3	0.5103	0.43	0.85	7.83	6.66
	12.438	1.2438	0.4938	516.2	0.5162	0.44	0.86	8.21	7.06
	12.889	1.2889	0.5389	530.1	0.5301	0.46	0.88	8.59	7.59

Table F. 3: G2cBN+25% Al

Sample	Length [mm]	Length, c [cm]	Δc (cm)	Load [N]	Load, P (kN)	*(c/W)*	*P/(B.W$^{0.5}$)*	*f (c/W)*	K_R (MPa.m$^{0.5}$) (calc)
1	7.5	0.75	0	51.7	0.0517				
	11.139	1.1139	0.3639	50.6	0.0506	0.40	0.08	7.24	0.61
	11.577	1.1577	0.4077	306.7	0.3067	0.41	0.51	7.54	3.86
	12.096	1.2096	0.4596	430	0.43	0.43	0.72	7.93	5.69
	12.563	1.2563	0.5063	429.9	0.4299	0.45	0.72	8.31	5.95
	13.049	1.3049	0.5549	428.4	0.4284	0.47	0.71	8.73	6.23
	13.521	1.3521	0.6021	423.8	0.4238	0.48	0.71	9.17	6.48

Table F. 4: G6cBN+15% Al

Sample	Length [mm]	Length, c [cm]	Δc (cm)	Load [N]	Load, P (kN)	*(c/W)*	*P/(B.W$^{0.5}$)*	*f (c/W)*	K_R (MPa.m$^{0.5}$) (calc)
1	7.5	0.75	0	53.2	0.0532				
	12.337	1.2337	0.4837	52.5	0.0525	0.44	0.09	8.12	0.71
	13.205	1.3205	0.5705	82	0.082	0.47	0.14	8.87	1.21
	13.642	1.3642	0.6142	217.9	0.2179	0.49	0.36	9.29	3.37
	16.254	1.6254	0.8754	118.3	0.1183	0.58	0.20	12.67	3.50
	19.159	1.9159	1.1659	108.4	0.1084	0.68	0.18	19.86	3.59
	19.665	1.9665	1.2165	104.8	0.1048	0.70	0.17	21.82	3.81
	20.174	2.0174	1.2674	93.4	0.0934	0.72	0.16	24.14	3.76
	20.62	2.062	1.312	76.3	0.0763	0.74	0.13	26.51	3.37
	21.075	2.1075	1.3575	69.2	0.0692	0.75	0.12	29.36	3.39
	21.535	2.1535	1.4035	61.8	0.0618	0.77	0.10	32.77	3.38
2	7.5	0.75	0	58.1	0.0581				
	10.19	1.019	0.269	121.5	0.1215	0.36	0.20	6.63	1.34

	10.656	1.0656	0.3156	320.9	0.3209	0.38	0.53	6.92	3.70
	10.886	1.0886	0.3386	505	0.505	0.39	0.84	7.07	5.95
	11.313	1.1313	0.3813	603.7	0.6037	0.40	1.01	7.36	7.40
	11.699	1.1699	0.4199	601.3	0.6013	0.42	1.00	7.63	7.65

Table F. 5: G6cBN+20% Al

Sample	**Length [mm]**	**Length, c [cm]**	**Δc (cm)**	**Load [N]**	**Load, P (kN)**	***(c/W)***	***P/(B.W$^{0.5}$)***	***f (c/W)***	**K_R (MPa.m$^{0.5}$) (calc)**
1	7.5	0.75	0	73.7	0.0737				
	10.244	1.0244	0.2744	72.6	0.0726	0.37	0.12	6.66	0.81
	10.743	1.0743	0.3243	203.9	0.2039	0.38	0.34	6.97	2.37
	11.201	1.1201	0.3701	364.5	0.3645	0.40	0.61	7.28	4.42
	11.085	1.1085	0.3585	462	0.462	0.40	0.77	7.20	5.54
	11.563	1.1563	0.4063	543.9	0.5439	0.41	0.91	7.53	6.83
	12.25	1.225	0.475	535.7	0.5357	0.44	0.89	8.05	7.19
	12.713	1.2713	0.5213	539.3	0.5393	0.45	0.90	8.44	7.58
	13.157	1.3157	0.5657	2.3	0.0023	0.47	0.00	8.83	0.03
2	7.5	0.75	0	97.7	0.0977				
	9.458	0.9458	0.1958	96.9	0.0969	0.34	0.16	6.19	1.00
	10.026	1.0026	0.2526	185.4	0.1854	0.36	0.31	6.53	2.02
	10.579	1.0579	0.3079	214.3	0.2143	0.38	0.36	6.87	2.45
	11.067	1.1067	0.3567	333.4	0.3334	0.40	0.56	7.19	3.99
	11.203	1.1203	0.3703	506.6	0.5066	0.40	0.84	7.28	6.15
	11.689	1.1689	0.4189	557.7	0.5577	0.42	0.93	7.63	7.09
	12.132	1.2132	0.4632	570.1	0.5701	0.43	0.95	7.96	7.56
	12.585	1.2585	0.5085	566.8	0.5668	0.45	0.94	8.33	7.87
	13.008	1.3008	0.5508	563.2	0.5632	0.46	0.94	8.69	8.16
	13.452	1.3452	0.5952	550.5	0.5505	0.48	0.92	9.10	8.35
	13.94	1.394	0.644	130.4	0.1304	0.50	0.22	9.60	2.09

Table F. 6: G6cBN+25% Al

Sample	**Length [mm]**	**Length, c [cm]**	**Δc (cm)**	**Load [N]**	**Load, P (kN)**	***(c/W)***	***P/(B.W$^{0.5}$)***	***f (c/W)***	**K_R (MPa.m$^{0.5}$) (calc)**
1	7.5	0.75	0	60.1	0.0601				
	9.431	0.9431	0.1931	59.7	0.0597	0.34	0.10	6.18	0.61
	9.937	0.9937	0.2437	175.5	0.1755	0.35	0.29	6.47	1.89
	10.435	1.0435	0.2935	270	0.27	0.37	0.45	6.78	3.05
	10.44	1.044	0.294	232.8	0.2328	0.37	0.39	6.78	2.63
	10.709	1.0709	0.3209	436.7	0.4367	0.38	0.73	6.95	5.06
	11.209	1.1209	0.3709	562.7	0.5627	0.40	0.94	7.28	6.83
	11.665	1.1665	0.4165	573	0.573	0.42	0.96	7.61	7.27
	12.091	1.2091	0.4591	600.7	0.6007	0.43	1.00	7.93	7.94
	12.529	1.2529	0.5029	595.3	0.5953	0.45	0.99	8.28	8.22
	12.982	1.2982	0.5482	587.3	0.5873	0.46	0.98	8.67	8.49
	13.459	1.3459	0.5959	581.6	0.5816	0.48	0.97	9.11	8.83
	13.854	1.3854	0.6354	556.1	0.5561	0.49	0.93	9.51	8.81

	14.279	1.4279	0.6779	546.7	0.5467	0.51	0.91	9.96	9.08

Table F. 7: G10cBN+15% Al

Sample	Length [mm]	Length, c [cm]	Δc (cm)	Load [N]	Load, P (kN)	*(c/W)*	*$P/(B.W^{0.5})$*	*f (c/W)*	K_R ($MPa.m^{0.5}$) (calc)
1	7.5	0.75	0	39.3	0.0393				
	11.304	1.1304	0.3804	39.1	0.0391	0.40	0.07	7.35	0.48
	11.797	1.1797	0.4297	367.1	0.3671	0.42	0.61	7.71	4.71
	12.321	1.2321	0.4821	343.5	0.3435	0.44	0.57	8.11	4.64
	12.783	1.2783	0.5283	329.1	0.3291	0.46	0.55	8.50	4.66
	13.254	1.3254	0.5754	344.2	0.3442	0.47	0.57	8.92	5.12

Table F. 8: G20cBN+15% Al

Sample	Length [mm]	Length, c [cm]	Δc (cm)	Load [N]	Load, P (kN)	*(c/W)*	*$P/(B.W^{0.5})$*	*f (c/W)*	K_R ($MPa.m^{0.5}$) (calc)
1	7.5	0.75	0	87.1	0.0871				
	10.397	1.0397	0.2897	83.5	0.0835	0.37	0.14	6.75	0.94
	10.885	1.0885	0.3385	645.5	0.6455	0.39	1.08	7.07	7.60
	11.31	1.131	0.381	681	0.681	0.40	1.14	7.35	8.35
	11.838	1.1838	0.4338	670	0.67	0.42	1.12	7.74	8.64
	12.3	1.23	0.48	651.5	0.6515	0.44	1.09	8.09	8.79
2	7.5	0.75	0	148.9	0.1489				
	10.187	1.0187	0.2687	146.7	0.1467	0.36	0.24	6.62	1.62
	10.677	1.0677	0.3177	503.1	0.5031	0.38	0.84	6.93	5.81
	11.122	1.1122	0.3622	709.6	0.7096	0.40	1.18	7.23	8.55
	11.549	1.1549	0.4049	703.4	0.7034	0.41	1.17	7.52	8.82
	11.987	1.1987	0.4487	701.2	0.7012	0.43	1.17	7.85	9.17
	12.215	1.2215	0.4715	711	0.711	0.44	1.19	8.03	9.51

Table F. 9: G20cBN+20% Al

Sample	Length [mm]	Length, c [cm]	Δc (cm)	Load [N]	Load, P (kN)	*(c/W)*	*$P/(B.W^{0.5})$*	*f (c/W)*	K_R ($MPa.m^{0.5}$) (calc)
1	7.5	0.75	0	56.1	0.0561				
	9.627	0.9627	0.2127	55.8	0.0558	0.34	0.09	6.29	0.59
	10.112	1.0112	0.2612	165.8	0.1658	0.36	0.28	6.58	1.82
	10.19	1.019	0.269	419.1	0.4191	0.36	0.70	6.63	4.63
	10.642	1.0642	0.3142	599.6	0.5996	0.38	1.00	6.91	6.90
	11.135	1.1135	0.3635	609	0.609	0.40	1.02	7.23	7.34
	11.626	1.1626	0.4126	620.4	0.6204	0.42	1.03	7.58	7.84
2	7.5	0.75	0	103.3	0.1033				
	10.094	1.0094	0.2594	102.3	0.1023	0.36	0.17	6.57	1.12
	10.567	1.0567	0.3067	423.1	0.4231	0.38	0.71	6.86	4.84
	11.018	1.1018	0.3518	613.4	0.6134	0.39	1.02	7.16	7.31
	11.458	1.1458	0.3958	620.8	0.6208	0.41	1.03	7.46	7.72
	11.851	1.1851	0.4351	617.3	0.6173	0.42	1.03	7.75	7.97

	12.051	1.2051	0.4551	613.9	0.6139	0.43	1.02	7.90	8.08
	12.492	1.2492	0.4992	603.2	0.6032	0.45	1.01	8.25	8.29
	12.914	1.2914	0.5414	602.3	0.6023	0.46	1.00	8.61	8.64
	12.924	1.2924	0.5424	601.2	0.6012	0.46	1.00	8.62	8.64
	13.463	1.3463	0.5963	588.9	0.5889	0.48	0.98	9.12	8.95
	13.975	1.3975	0.6475	560.3	0.5603	0.50	0.93	9.63	9.00

Table F. 10: G20cBN+25% Al

Sample	**Length [mm]**	**Length, c [cm]**	**Δc (cm)**	**Load [N]**	**Load, P (kN)**	***(c/W)***	***P/(B.W$^{0.5}$)***	***f (c/W)***	**K_R (MPa.m$^{0.5}$) (calc)**
1	7.5	0.75	0	483	0.0483				
	20.874	2.0874	1.3374	474	0.0474	0.75	0.08	28.04	2.22
	21.345	2.1345	1.3845	930	0.093	0.76	0.16	31.29	4.85
	21.808	2.1808	1.4308	1053	0.1053	0.78	0.18	35.11	6.16
	22.321	2.2321	1.4821	956	0.0956	0.80	0.16	40.29	6.42
	22.87	2.287	1.537	844	0.0844	0.82	0.14	47.35	6.66
	23.345	2.3345	1.5845	666	0.0666	0.83	0.11	55.21	6.13
	23.854	2.3854	1.6354	504	0.0504	0.85	0.08	66.23	5.56
	24.442	2.4442	1.6942	451	0.0451	0.87	0.08	84.11	6.32
	24.94	2.494	1.744	352	0.0352	0.89	0.06	106.30	6.24
	25.399	2.5399	1.7899	247	0.0247	0.91	0.04	136.59	5.62
2	7.5	0.75	0	977	0.0977				
	10.136	1.0136	0.2636	970	0.097	0.36	0.16	6.59	1.07
	10.418	1.0418	0.2918	3715	0.3715	0.37	0.62	6.77	4.19
	10.799	1.0799	0.3299	4689	0.4689	0.39	0.78	7.01	5.48
	11.295	1.1295	0.3795	5568	0.5568	0.40	0.93	7.34	6.82
	11.757	1.1757	0.4257	5757	0.5757	0.42	0.96	7.68	7.37
	12.332	1.2332	0.4832	5750	0.575	0.44	0.96	8.12	7.78
	12.819	1.2819	0.5319	5698	0.5698	0.46	0.95	8.53	8.10
	13.326	1.3326	0.5826	5539	0.5539	0.48	0.92	8.98	8.29
	13.826	1.3826	0.6326	5458	0.5458	0.49	0.91	9.48	8.62

Appendix G: Results of the Flexural Strength Tests

The results of the flexural strength testing for the PcBN-Al composite materials are given in Tables G 1-10 below. The samples dimensions; length (l), width (b) and thickness (d); load to failure (F) and flexural strength (σ_f) are shown. The mean strength and standard deviation for each material composition are also shown. Sample dimensions were approximately 25x4x3 mm^3.

The flexural strength (σ_f) for a 4-point bend testing is calculated based on the equation: $\sigma_f = \frac{3Fa}{bd^2}$ *where* $a = \frac{S_2 - S_1}{2} = \frac{20-10}{2} = 5\,mm$

Table G. 1: G2 cBN + 15% Al

Sample	length (l)	width (b)	thickness (d)	F (load) (N)	Flexural strength (σ_f) [MPa]
1	25.27	3.92	2.86	756.1	353.7
2	25.33	3.87	2.97	714.6	313.9
3	25.48	3.74	3.08	1045.3	441.9
4	25.38	3.75	3.00	773.2	343.6
5	25.39	3.96	3.05	1080.2	439.8
6	25.28	3.75	2.99	759.5	339.8
7	25.39	3.79	3.06	828.8	350.3
8	25.25	3.92	2.86	704.6	329.6
9	25.40	3.78	3.08	953.5	398.8
10	25.33	3.99	2.86	744.9	342.3
11	25.29	3.76	2.97	766.8	346.7
12	25.47	3.74	3.12	953.1	392.6
13	25.37	3.78	2.84	754.5	371.2
14	25.32	4.00	2.84	827.1	384.5
15	25.27	4.00	2.85	700.9	323.6
16	25.42	3.93	3.07	903.8	366.0
17	24.49	3.96	2.93	972.2	428.98
18	25.24	3.98	3.03	1029.6	422.6
				Mean	371.7
				Std dev	40.8

Table G. 2: G2 cBN + 20% Al

Sample	length (l)	width (b)	thickness (d)	F (load) (N)	Flexural strength (σ_f) [MPa]
1	25.31	4.06	2.95	874.3	371.1
2	25.19	3.96	2.96	872.8	377.3
3	25.37	4.04	2.89	769.5	342.0
4	25.36	4.01	2.90	875.3	389.3
5	25.47	4.01	2.92	1179.4	517.4
6	25.43	4.00	2.89	968.9	435.0
7	25.48	3.94	3.03	904.1	374.9
8	25.37	4.00	2.96	1029.6	440.6
9	25.31	4.06	2.88	760.9	338.9
10	25.23	4.00	3.03	1121.5	458.0
11	25.38	3.99	3.00	933.8	390.0
12	25.31	4.04	2.87	1095.7	493.8
13	25.59	3.99	2.88	1175.8	532.9
14	25.17	3.99	2.92	1023.8	451.3
15	25.23	4.06	2.86	703.0	317.5
16	25.20	3.98	2.94	885.9	386.2
17	25.31	4.04	2.92	940.4	409.4
18	25.28	4.03	2.88	875.9	393.0
19	25.26	4.04	2.92	874.9	380.9
20	25.26	4.06	2.97	774.4	324.3
				Mean	406.2
				Std dev	61.0

Table G. 3: G2 cBN + 25% Al

Sample	length (l)	width (b)	thickness (d)	F (load) (N)	Flexural strength (σ_f) [MPa]
1	25.19	4.01	2.90	994.8	442.4
2	25.41	4.07	2.99	1265.1	521.5
3	25.44	4.11	2.97	1085.5	449.1
4	25.48	4.07	2.85	912.8	414.1
5	25.36	4.10	3.07	1135.6	440.8
6	25.39	4.10	2.92	897.4	385.0
7	25.45	4.04	3.03	1048.2	423.9
8	25.34	4.08	2.92	894.7	385.7
9	25.49	4.09	2.98	1079.5	445.8
10	25.23	4.05	2.88	1068.9	477.3
11	25.36	4.09	2.90	791.6	345.2
12	25.36	3.99	2.88	1059.8	480.3
13	25.25	4.02	2.93	1032.4	448.7
14	25.29	4.10	3.00	1108.4	450.5
15	25.33	4.08	2.90	917.6	401.1
16	25.31	4.09	3.06	919.5	360.1
17	25.60	4.06	2.94	929.3	397.2
18	25.38	4.10	2.92	961.6	412.5
19	25.18	4.10	2.89	950.5	416.3
20	25.21	4.11	2.94	987.9	417.1
				Mean	425.7
				Std dev	41.8

Table G. 4: G6 cBN + 15% Al

Sample	length (l)	width (b)	thickness (d)	F (load) (N)	Flexural strength (σ_f) [MPa]
1	25.46	4.11	2.97	1202.02	497.3
2	25.41	4.11	2.85	949.1	426.4
3	25.36	4.09	2.92	758.7	326.3
4	25.40	4.10	2.91	748.3	323.3
5	25.37	4.10	2.92	699.2	300.0
6	25.28	4.10	2.91	973.1	420.4
7	25.17	4.12	2.86	1047.1	466.0
8	25.13	4.11	2.84	1000.5	452.7
9	25.38	4.08	2.90	730.4	319.3
10	25.39	4.09	2.88	762.5	337.1
11	25.25	4.11	2.97	1087.2	449.8
12	25.11	4.08	2.92	706.1	304.4
13	25.34	4.14	2.90	881.2	379.6
14	25.49	4.09	2.90	670.8	292.5
15	25.20	4.10	2.82	1001.03	460.5
16	25.14	4.09	2.92	669.7	288.0
17	25.09	4.06	2.86	719.2	324.8
18	25.50	4.15	2.82	970.2	440.9
19	25.44	4.11	2.92	759.02	324.8
20	25.19	4.11	2.85	1026.7	461.3
				Mean	379.8
				Std dev	71.7

Table G. 5: G6 cBN + 20% Al

Sample	length (l)	width (b)	thickness (d)	F (load) (N)	Flexural strength (σ_f) [MPa]
1	25.45	4.19	2.95	925.5	380.7
2	25.42	4.22	2.93	952.2	394.2
3	25.28	4.18	2.83	836.1	374.6
4	28.17	4.22	2.90	991.2	418.9
5	25.46	4.23	2.93	879.2	363.1
6	25.43	4.22	2.94	893.8	367.5
7	25.23	4.18	2.77	876.9	410.1
8	25.39	4.22	2.87	891.9	384.8
9	25.40	4.21	3.02	945.8	369.5
10	25.40	4.21	2.84	965.3	426.4
11	25.13	4.17	2.87	822.8	359.3
12	25.17	4.17	2.76	884.1	417.5
13	25.29	4.22	2.76	632.2	294.9
14	25.43	4.22	2.96	907.9	368.3
15	25.40	4.22	2.94	923.5	379.7
16	25.17	4.23	2.93	920.01	380.0
17	25.37	4.18	2.83	819.5	367.2
18	25.59	4.18	2.78	904.3	419.9
19	25.19	4.18	2.89	873.3	375.2
				Mean	381.7
				Std dev.	30.1

Table G. 6: G6 cBN + 25% Al

Sample	length (l)	width (b)	thickness (d)	F (load) (N)	Flexural strength (σ_f) [MPa]
1	25.37	4.13	2.85	931.9	416.7
2	25.45	4.14	2.90	982.1	423.0
3	25.39	4.18	2.84	915.3	407.2
4	25.45	4.14	2.90	908.3	391.3
5	25.37	4.17	2.87	1012.9	442.3
6	25.44	4.10	2.87	863.8	383.6
7	25.39	4.14	2.90	934.5	402.5
8	25.35	4.14	2.85	1080.5	481.9
9	25.40	4.12	2.88	893.6	392.2
10	25.28	4.11	2.88	979.8	431.1
11	25.39	4.12	2.89	967.9	421.9
12	25.44	4.12	2.93	982.7	416.7
13	25.40	4.11	2.93	982.8	417.7
14	25.33	4.13	2.90	979.8	423.1
15	25.38	4.14	2.87	1029.8	452.9
16	25.47	4.12	2.89	921.6	401.7
17	25.43	4.11	2.92	994.8	425.8
18	25.48	4.15	2.93	974.1	410.1
19	25.34	4.18	2.85	888.8	392.6
20	25.39	4.12	2.95	1001.03	418.7
				Mean	417.7
				Std dev	23.0

Table G. 7: G10 cBN + 15% Al

Sample	length (l)	width (b)	thickness (d)	F (load) (N)	Flexural strength (σ_f) [MPa]
1	25.44	4.18	2.93	1046	437.2
2	25.34	4.10	2.89	1020	446.7
3	25.44	4.18	2.96	1044.8	427.9
4	25.40	4.09	3.03	947.2	378.4
5	25.39	4.09	3.00	1154.4	470.4
6	25.52	4.10	3.02	1073.1	430.4
7	25.43	4.18	2.98	1111.2	449.0
8	25.37	4.17	2.91	1068.6	453.9
9	25.46	4.07	2.85	951.6	431.7
10	25.40	4.16	2.96	1114.5	458.6
11	25.45	4.17	2.95	1095.7	452.8
12	25.23	4.13	2.94	1059.5	445.1
13	25.35	4.08	2.86	964.8	433.6
14	25.45	4.12	2.78	915.5	431.3
15	25.38	4.17	3.02	1204.9	475.2
16	25.44	4.17	2.95	1164.4	481.3
17	25.40	4.16	2.98	1137.6	461.8
18	25.37	4.11	2.79	912.9	428.0
19	25.43	4.13	2.79	981.5	457.9
20	25.35	4.08	2.94	999.8	425.2
				Mean	443.8
				Std dev	22.7

Table G. 8: G20 cBN + 15% Al

Sample	length (l)	width (b)	thickness (d)	F (load) (N)	Flexural strength (σ_f) [MPa]
1	25.35	4.11	2.98	893.1	367.0
2	25.41	4.12	2.93	916.6	388.7
3	25.51	4.19	2.91	810.05	342.4
4	25.38	4.13	3.00	951.7	384.0
5	25.40	4.13	2.90	892.1	385.2
6	25.45	4.14	2.82	945.7	430.8
7	25.40	4.14	2.86	900.02	398.6
8	25.46	4.12	3.00	1035.3	418.8
9	25.34	4.11	2.93	864	367.3
10	25.47	4.12	2.94	899.3	378.8
11	25.43	4.12	2.86	759.9	338.2
12	25.39	4.11	2.88	879.5	386.9
13	25.52	4.11	2.84	829.7	375.4
14	25.42	4.11	2.94	891.7	376.5
15	25.34	4.10	2.96	855.2	357.1
16	25.37	4.09	2.99	1022.4	419.4
17	25.42	4.11	2.98	885.9	364.0
18	25.45	4.12	2.87	950.1	419.9
19	25.41	4.12	2.98	954.1	391.1
20	25.34	4.10	2.95	921.7	387.5
				Mean	383.9
				Std dev	25.06

Table G. 9: G20 cBN + 20% Al

Sample	length (l)	width (b)	thickness (d)	F (load) (N)	Flexural strength (σ_f) [MPa]
1	25.44	4.13	2.97	846.9	348.7
2	25.38	4.14	2.73	753	366.0
3	25.37	4.12	3.05	902.8	353.3
4	25.46	4.19	2.98	829.2	334.2
5	25.44	4.11	2.99	869.3	354.8
6	25.34	4.12	2.98	708.7	290.5
7	25.39	4.13	2.90	803.3	346.9
8	25.36	4.18	2.90	786.9	335.7
9	25.32	4.17	2.88	728.7	316.0
10	25.34	4.10	2.93	815.6	347.5
11	25.37	4.16	2.96	801.7	329.9
12	25.34	4.19	2.91	796.8	336.8
13	25.40	4.14	3.02	900.5	357.7
14	25.40	4.19	2.87	835.9	363.3
15	25.44	4.08	2.89	800.4	352.3
16	25.36	4.18	2.97	904.9	368.1
17	25.39	4.14	2.73	690.9	335.8
18	25.43	4.13	2.91	860.7	369.1
19	25.40	4.12	2.89	846.2	368.8
20	25.41	4.15	2.72	731.6	357.4
				Mean	346.6
				Std dev	19.6

Table G. 10: G20 cBN + 25% Al

Sample	length (l)	width (b)	thickness (d)	F (load) (N)	Flexural strength (σ_f) [MPa]
1	25.38	4.17	2.78	824.7	383.8
2	25.34	4.17	3.04	978.9	381.0
3	25.33	4.19	3.07	1036.02	393.5
4	25.36	4.17	3.06	1078.8	414.4
5	25.35	4.18	2.81	838.5	381.0
6	25.33	4.23	2.97	846.9	340.4
7	25.47	4.19	2.80	914.7	417.6
8	25.31	4.17	2.99	935.5	376.4
9	25.21	4.17	3.00	854	341.3
10	25.34	4.18	2.92	956.4	402.5
11	25.35	4.17	2.90	920.02	393.5
12	25.35	4.16	2.92	915.7	387.2
13	25.30	4.19	2.94	890.9	368.9
14	25.27	4.17	2.94	938.6	390.6
15	25.39	4.13	2.93	842.3	356.3
16	25.23	4.18	3.03	850.04	332.2
17	25.25	4.16	3.00	943.5	377.9
18	25.34	4.19	2.94	925.9	383.4
19	25.23	4.19	2.85	878.7	387.2
				Mean	379.4
				Std dev	23.2

Appendix H: Results of the Weibull Statistics

The Tables H 1-10 show the results from the Weibull-statistical analysis of the flexural strength data of the PcBN-Al composite materials, which use the "Maximum Likelihood" method. The results show the characteristic strength values (σ_O) and the Weibull modulus (m) for the various confidence intervals. The average strength (σ), Weibull modulus (m) and standard deviation (s) are also shown as a comparison.

Weibull Statistics of the PcBN-Al Composite Materials.

Table H. 1: G 2 cBN + 15 % Al

	σ_u	
C. I. Limits	σ_c	m
Statistical Characteristic (63%)	390.1	9.77
2 %	367.7	5.99
5 %	372.6	6.57
10 %	376.8	7.25
25 %	383.6	8.15
75 %	397.7	10.44
90 %	404.5	11.71
95 %	408.6	12.47
98 %	413.9	13.31
m average	9.08	
σ	371.7	
Standard deviation s	40.81	

Table H. 2: G 2 cBN + 20 % Al

	σ_u	
C. I. Limits	σ_c	m
Statistical Characteristic (63%)	432.7	6.97
2 %	400.4	4.42
5 %	407.4	4.82
10 %	413.3	5.29
25 %	423.2	5.89
75 %	443.6	7.44
90 %	453.8	8.3
95 %	459.8	8.81
98 %	467.6	9.4
m average	6.53	
Σ	406.3	
Standard deviation s	61.08	

Table H. 3: G 2 cBN + 25 % Al

	σ_u	
C. I. Limits	σ_c	m
Statistical Characteristic (63%)	444.5	10.03
2 %	422.6	6.78
5 %	427.4	7.4
10 %	431.4	8.12
25 %	438.1	9.05
75 %	451.9	11.43
90 %	458.5	12.75
95 %	462.4	13.54
98 %	467.5	14.41
m average	10.03	
Σ	425.8	
Standard deviation s	41.9	

Table H. 4: G 6 cBN + 15 % Al

	σ_u	
C. I. Limits	σ_c	m
Statistical Characteristic (63%)	409.4	6.14
2 %	374.8	3.89
5 %	382.3	4.25
10 %	388.6	4.66
25 %	399.2	5.19
75 %	421.3	6.56
90 %	432.1	7.31
95 %	438.5	7.76
98 %	447.0	8.27
m average	5.75	
Σ	379.8	
Standard deviation s	71.7	

Table H. 5: G 6 cBN + 20 % Al

	σ_u	
C. I. Limits	σ_c	m
Statistical Characteristic (63%)	394.5	15.67
2 %	380.6	9.77
5 %	383.7	10.7
10 %	386.3	11.76
25 %	390.5	13.16
75 %	399.1	16.73
90 %	403.2	18.72
95 %	405.6	19.9
98 %	408.8	21.21
m average	14.62	
Σ	381.7	
Standard deviation s	30.1	

Table H. 6: G 6 cBN + 25 % Al

	σ_u	
C. I. Limits	σ_c	m
Statistical Characteristic (63%)	429.1	16.2
2 %	414.9	10.26
5 %	418.0	11.2
10 %	420.7	12.29
25 %	424.9	13.7
75 %	433.7	17.3
90 %	437.9	19.3
95 %	440.4	20.5
98 %	443.6	21.8
m average	15.2	
Σ	417.7	
Standard deviation s	23.04	

Table H. 7: G 10 cBN + 15 % Al

	σ_u	
C. I. Limits	σ_c	m
Statistical Characteristic (63%)	453.8	23.97
2 %	443.6	15.18
5 %	445.8	16.56
10 %	447.7	18.17
25 %	450.8	20.25
75 %	457.1	25.58
90 %	460.1	28.53
95 %	461.8	30.29
98 %	464.1	32.25
m average	22.44	
Σ	443.9	
Standard deviation s	22.7	

Table H. 8: G 20 cBN + 15 % Al

	σ_u	
C. I. Limits	σ_c	m
Statistical Characteristic (63%)	395.5	16.6
2 %	382.8	10.51
5 %	385.6	11.47
10 %	387.9	12.58
25 %	391.8	14.03
75 %	399.7	17.71
90 %	403.5	19.77
95 %	405.7	20.98
98 %	408.6	22.33
m average	15.54	
Σ	383.9	
Standard deviation s	25.06	

Table H. 9: G 20 cBN + 20 % Al

	σ_u	
C. I. Limits	σ_c	M
Statistical Characteristic (63%)	354.8	24.88
2 %	347.2	15.76
5 %	348.9	17.2
10 %	350.3	18.87
25 %	352.6	21.03
75 %	357.3	26.56
90 %	359.5	29.62
95 %	360.9	31.45
98 %	362.6	33.48
m average	23.3	
Σ	346.7	
Standard deviation s	19.67	

Table H. 10: G 20 cBN + 25 % Al

	σ_u	
C. I. Limits	σ_c	m
Statistical Characteristic (63%)	389.7	19.88
2 %	378.9	12.39
5 %	381.3	13.56
10 %	383.3	14.92
25 %	386.6	16.7
75 %	393.2	21.22
90 %	396.4	23.74
95 %	398.3	25.24
98 %	400.8	26.91
m average	18.5	
Σ	379.5	
Standard deviation s	23.28	

Appendix I: Flaw Size

The flaw size of the various materials can be estimated using the Griffiths equation (equation 3.1 in Chapter 3) relating the strength and fracture toughness of the material to the flaw size of failure. Based on the fracture toughness, K_{Ic}, the size of a crack initiating flaw can be calculated for a definite strength value σ_f according to

$$a = \left(\frac{K_{Ic}}{\sigma_f \cdot Y} \right)^2, \qquad Y = \sqrt{\pi}/2 \ , \ a \ = \text{radius of flaw, [Munz (2007)]}$$

This can be used to determine whether the results obtained from the strength and fracture toughness measurements are in the correct range by comparing them with the results of the actual flaw size measured by microscopy. The flaw size of the flaws in each material will be measured using optical microscopes or scanning electron microscopes to determine the accuracy of the estimated results. Table I1 shows the estimated flaw size for the PcBN-Al composites, in the range between 300 -650 μm.

Table I. 1: Estimation of the flaw size of the PcBN-Al composites.

Sample	Strength (MPa)	Fracture toughness, K_{IC} ($MPa.m^{0.5}$)	Estimated Flaw size (μm)
G2 cBN + 15% Al	371.7	6.44	382
G2 cBN + 20% Al	406.3	7.08	386
G2 cBN + 25% Al	425.8	7.12	356
G6 cBN + 15% Al	379.8	7.56	505
G6 cBN + 20% Al	381.7	7.61	506
G6 cBN + 25% Al	417.7	7.04	361
G10 cBN + 15% Al	443.9	8.03	417
G20 cBN + 15% Al	383.9	7.93	543
G20 cBN + 20% Al	346.7	7.81	646
G20 cBN + 25% Al	379.5	6.95	427

The type and size of each flaw from each sample material was estimated using microscopy. Figures I 1-10 show the probability graphs for each material. Table I 2-11 show the flaw type, strength and measured flaw size. Not all the flaws could be identified and only a few of the flaws were measured, 10-15% of the tested specimens of each batch; of a high, medium and low strength.

The type of flaw is shown:

B - binder	SD - Surface defect	B/P - binder or pore	P - Pore	P & B - binder surrounding pore

Figure I. 1: Strength distribution of G2 cBN + 15% Al

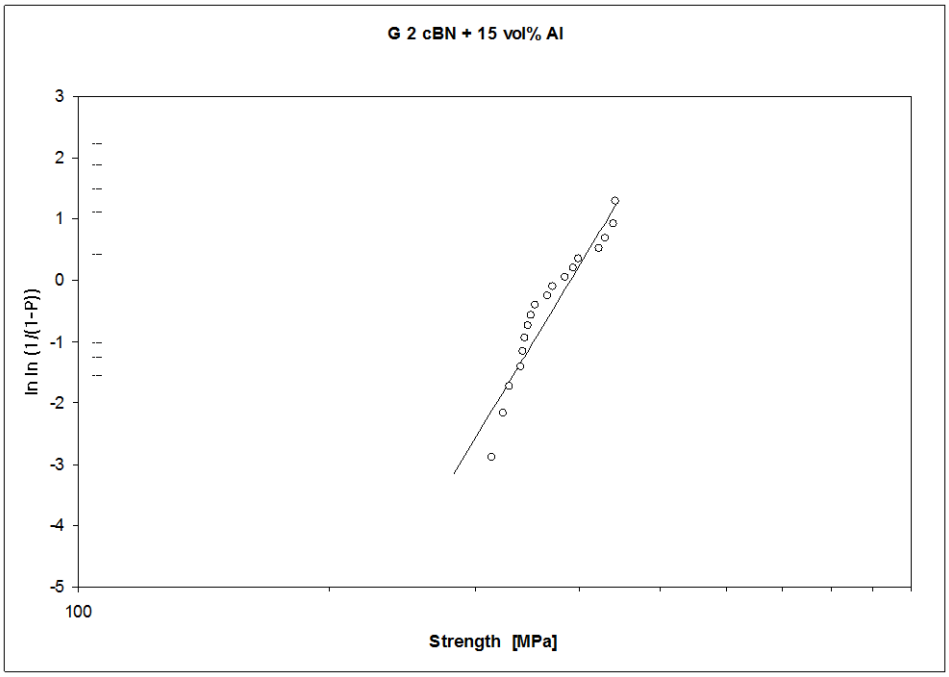

Table I. 2: Flaw type and size for G2 cBN + 15% Al

Sample No:	Flaw type	Strength (MPa)	Flaw Size (µm)
3	B	442	
5	Large P	440	400
17	P	429	
18	P	423	
9	B	399	
12	Large B	393	
14	Large B	385	
13	?	371	
16	?SD	366	
1	Large B	354	110
7	B	350	
11	?	347	
4	Large B	344	
10	Large B	342	
6	Large B	340	
8	Large P SD	330	
15	Large P SD	324	208
2	P	314	208

Figure I. 2: Strength distribution of G2 cBN + 20% Al

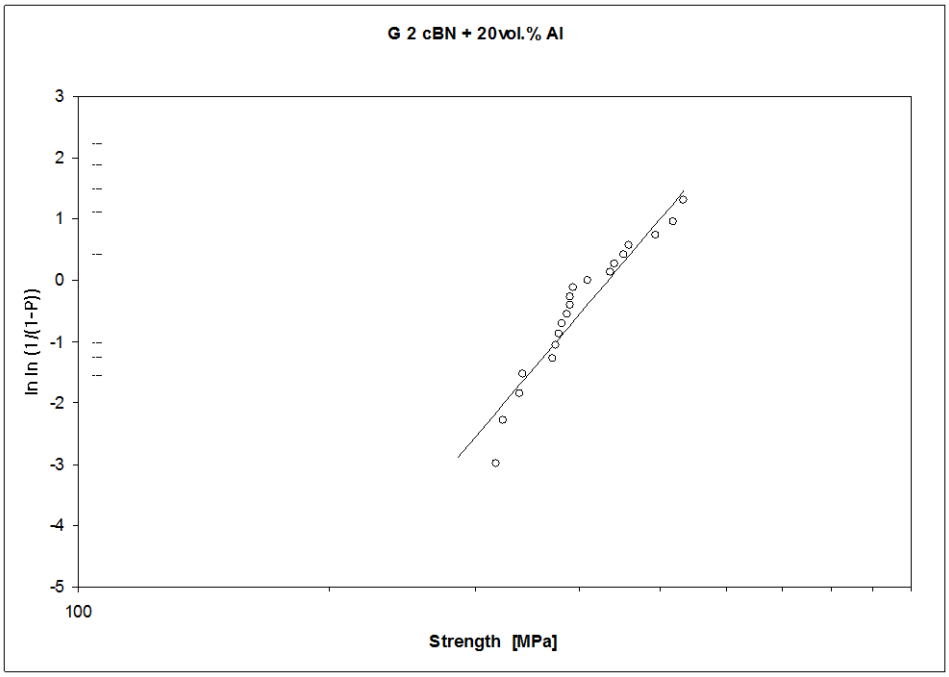

Table I. 3: Flaw type and size for G2 cBN + 20% Al

Sample No:	Flaw type	Strength (MPa)	Flaw Size (µm)
13	B	533	
5	B	517	410
12	?	494	
10	?	458	
14	B	451	
8	B	441	
6	Oxide inclusion	435	421
17	B	409	
18	P	393	
11	B	390	
4	B	389	
16	B	386	
19	P	381	
2	ED	377	
7	B	375	
1	P / large grain	371	200
3	P	342	
9	P	339	190
20	SD	324	100
15	B/P	318	

Figure I. 3: Strength distribution of G2 cBN + 25% Al

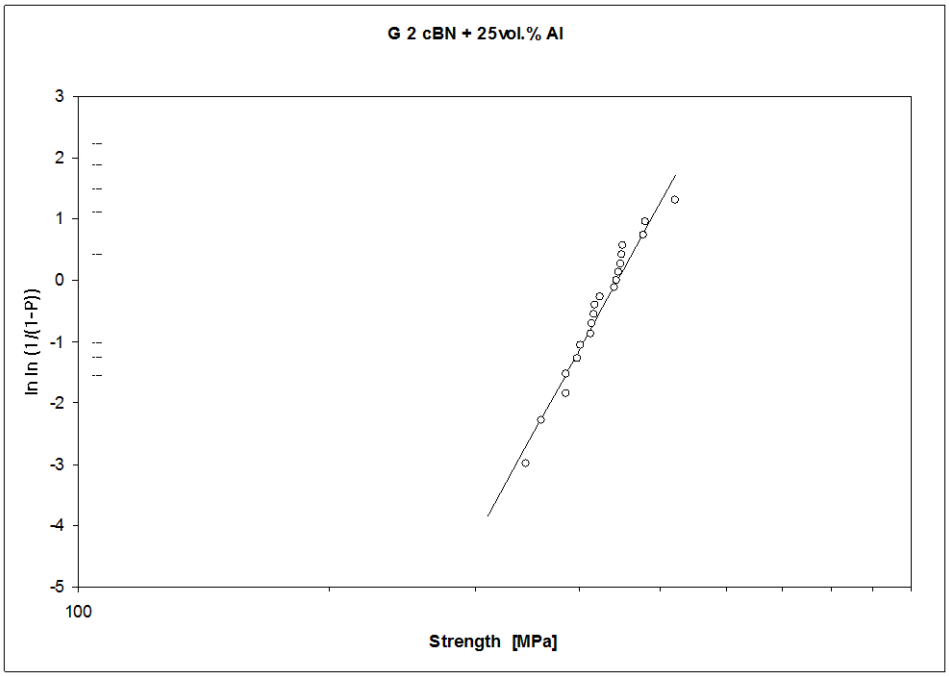

Table I. 4: Flaw type and size for G2 cBN + 25% Al

Sample No:	Flaw type	Strength (MPa)	Flaw Size (µm)
2	B	522	180
12	P	480	
10	B	477	
14	P	451	
3	B	449	
13	B	449	
9	B	446	
1	ED P & B	442	85
5	?	441	
7	?	424	
20	SD	417	
19	Large P	416	275
4	B	414	
18	P	413	
15	B with small P	401	150
17	B/P	397	
8	SD	386	
6	B	385	
16	B	360	
11	?B	345	

Figure I. 4: Strength distribution of G6 cBN + 15% Al

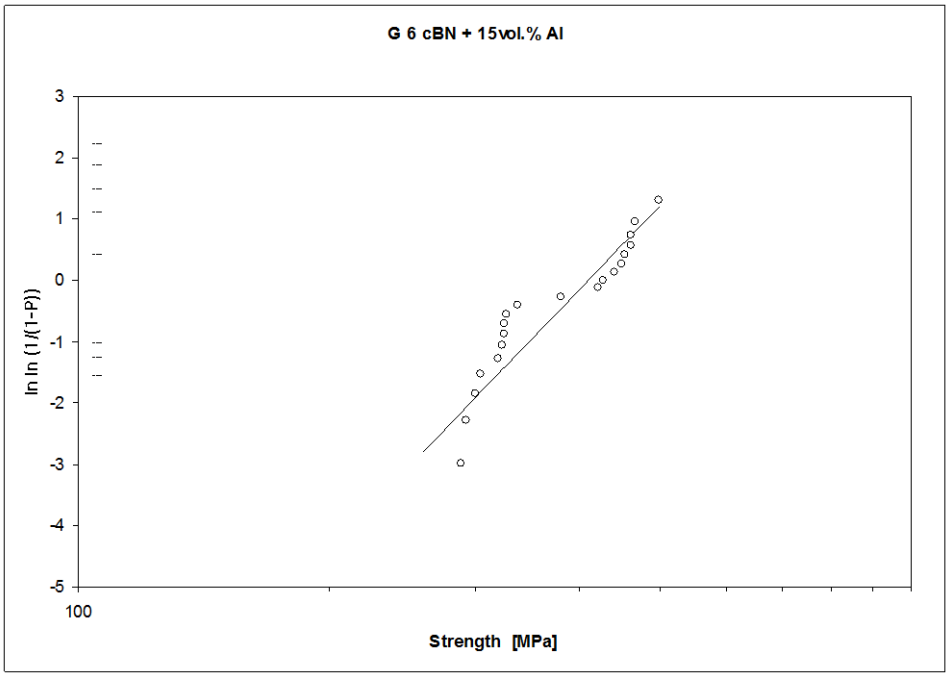

Table I. 5: Flaw type and size for G6 cBN + 15% Al

Sample No:	Flaw type	Strength (MPa)	Flaw Size (µm)
8	B	482	
15	B	453	
5	SD B	442	263
10	?	431	
17	B	426	
14	B	423	487
2	B	423	
11	B	422	
20	B	419	
13	B	418	
12	P	417	
1	B	417	
18	ED	410	
3	B	407	
7	B	403	
16	B with P	402	359
19	B	393	
9	SD	392	
4	P	391	
6	P	384	

Figure I. 5: Strength distribution of G6 cBN + 20% Al

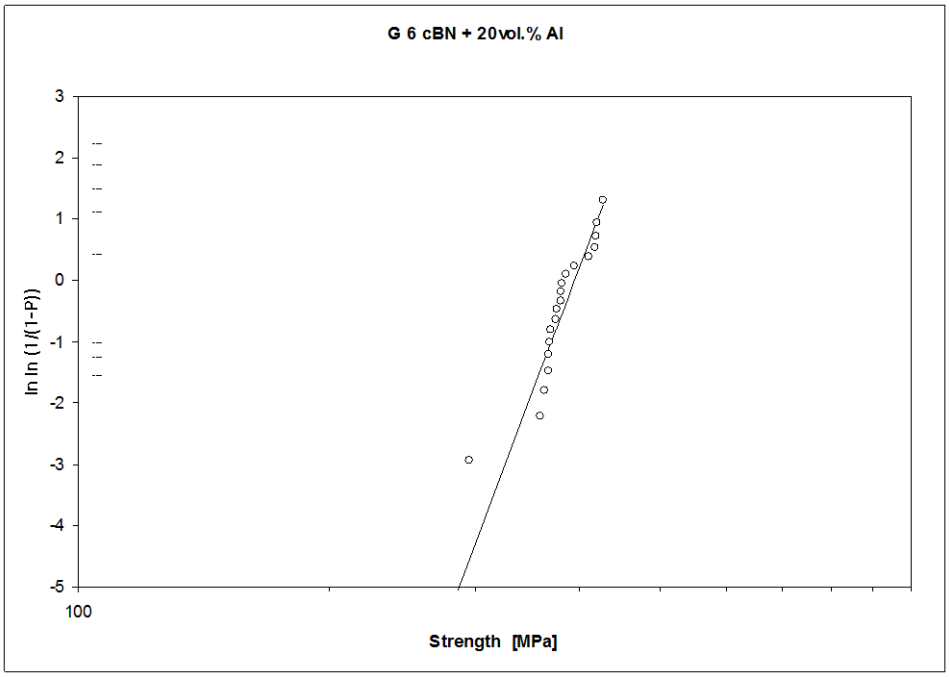

Table I. 6: Flaw type and size for G6 cBN + 20% Al

Sample No:	Flaw type	Strength (MPa)	Flaw Size (µm)
11	SD Large P	426	257
19	Large B	420	
4	B	419	
13	SD P	418	226
7	B	410	
2	B	394	
8	B	385	
1	P	381	
17	B	380	
16	B	380	
20	B	375	
3	P	375	500
10	B	370	
15	B/P	368	
6	B	368	
18	B	367	
5	B	363	
12	B	359	
14	B	295	298

Figure I. 6: Strength distribution of G6 cBN + 25% Al

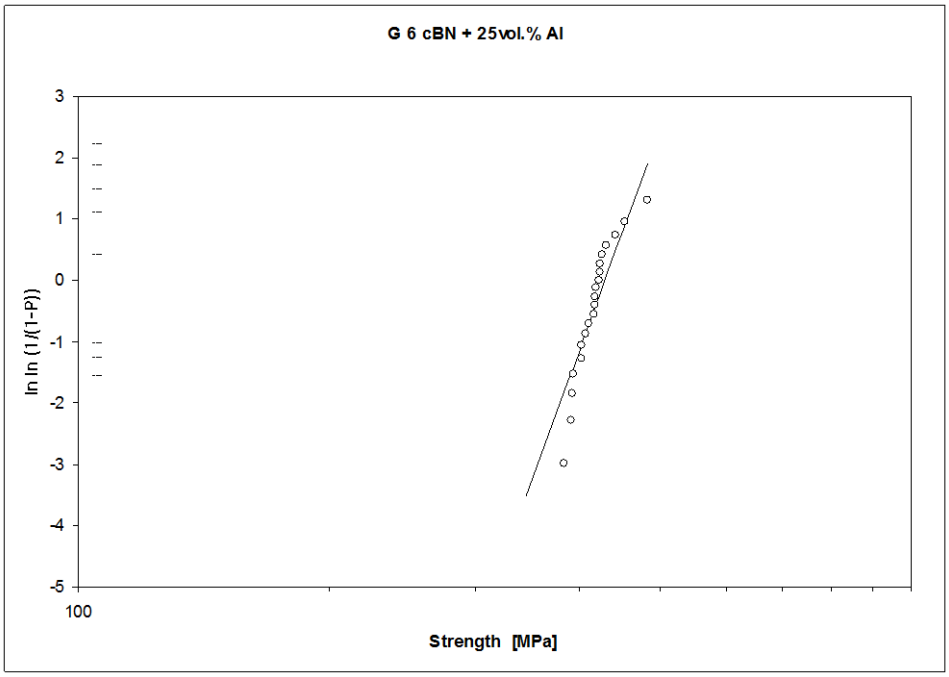

Table I. 7: Flaw type and size for G6 cBN + 25% Al

Sample No:	Flaw type	Strength (MPa)	Flaw Size (µm)
1	B	497	
7	P	466	370
20	P	461	
15	P	461	
8	B	453	
11	?	450	
18	B	441	
2	B	426	
6	P	420	148
13	B	380	
10	P	337	
3	P	326	
19	P	325	
17	B	325	
4	B	323	216
9	P	319	
12	SD P	304	188
5	P	300	
14	P	293	162
16	P	288	

Figure I. 7: Strength distribution of G10 cBN + 15% Al

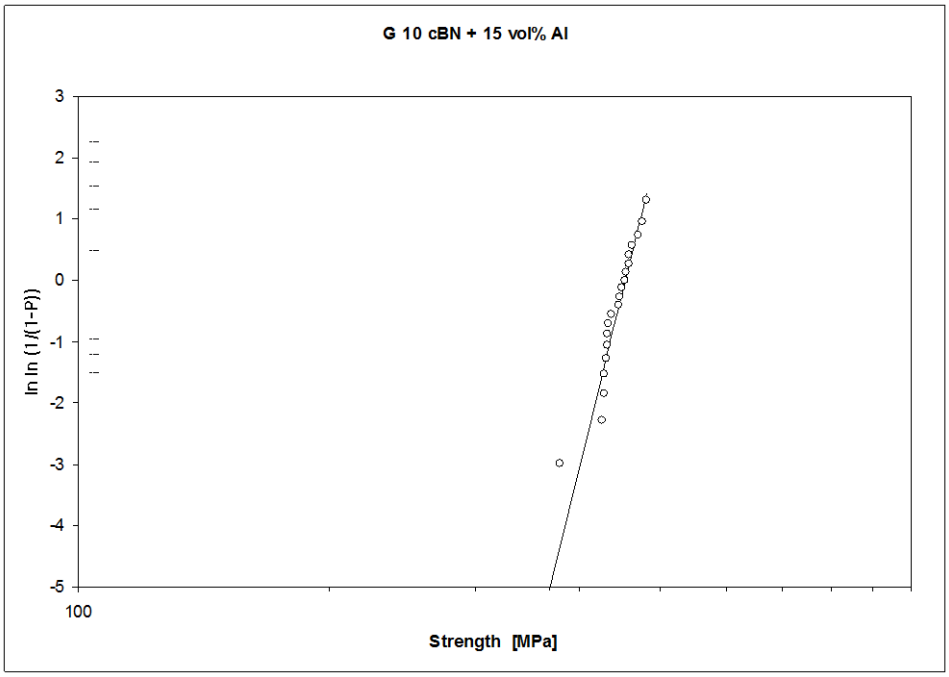

Table I. 8: Flaw type and size for G10 cBN + 15% Al

Sample No:	Flaw type	Strength (MPa)	Flaw Size (µm)
16	?	481	
15	?	475	270
5	?	470	
17	?	462	
10	?	459	
19	SD	458	310
8	B	454	
11	P	453	
7	B	449	
2	? P	447	
12	B	445	
1	B	437	
13	B	434	
9	B	432	
14	B	431	
6	B	430	
18	P	428	
3	B	428	417
20	B	425	
4	B with small P	378	237

Figure I. 8: Strength distribution of G20 cBN + 15% Al

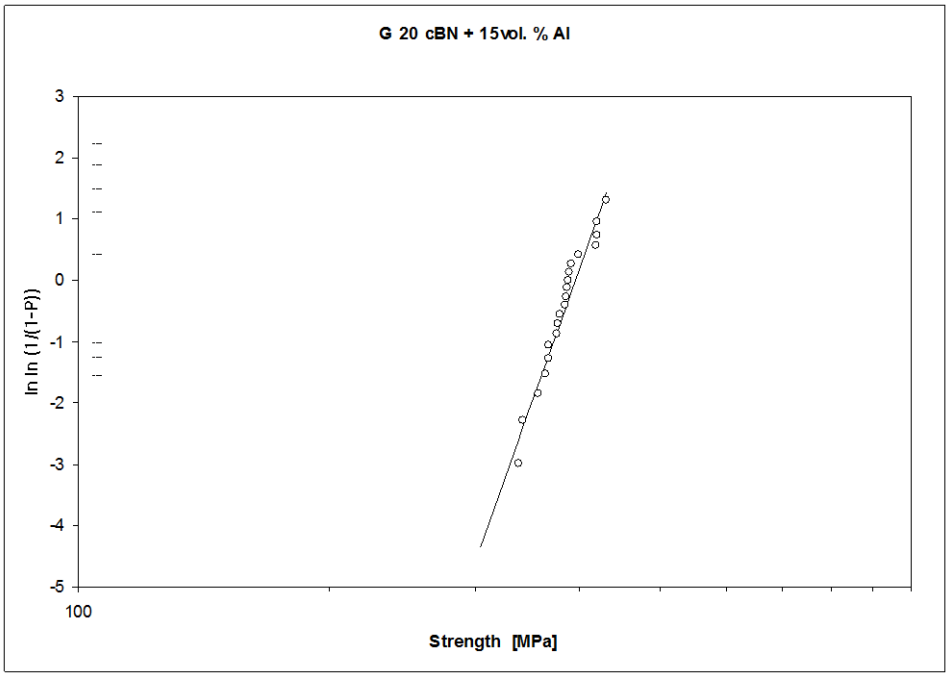

Table I. 9: Flaw type and size for G20 cBN + 15% Al

Sample No:	Flaw type	Strength (MPa)	Flaw Size (µm)
6	?	431	
18	B	420	312
16	ED P	419	
8	?	419	
7	P	399	
19	B	391	
2	B	389	236
20	SD	388	
12	P	387	
5	B	385	325
4	B	384	203
10	B	379	
14	P	377	
13	B	375	
9	B	367	
1	?	367	
17	P	364	163
15	P	357	
3	?	342	
11	?B	338	265

Figure I. 9: Strength distribution of G20 cBN + 20% Al

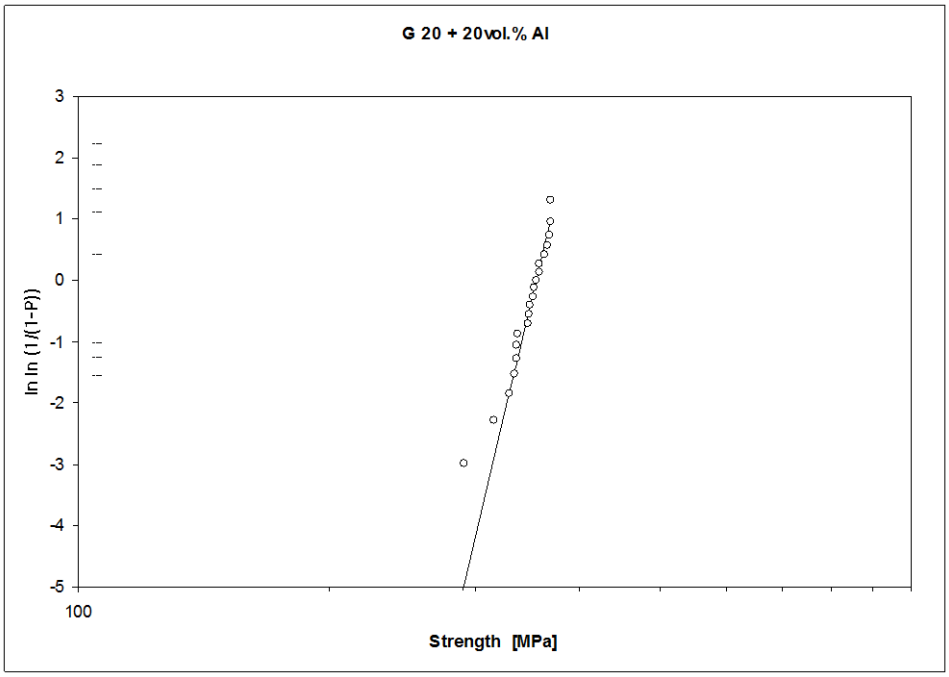

Table I. 10: Flaw type and size for G20 cBN + 20% Al

Sample No:	Flaw type	Strength (MPa)	Flaw Size (µm)
18	ED P	369	
19	B	369	
16	SD P	368	365
2	B	366	
14	?	363	
13	?	358	
20	Large B	357	290
5	P	355	
3	B	353	
15	?	352	
1	B	349	
10	B	348	
7	B	347	
12	?	337	
17	SD P	336	237
8	B	336	
4	ED B with P	334	212
11	?	330	
9	B	316	
6	B	291	

Figure I. 10: Strength distribution of G20 cBN + 25% Al

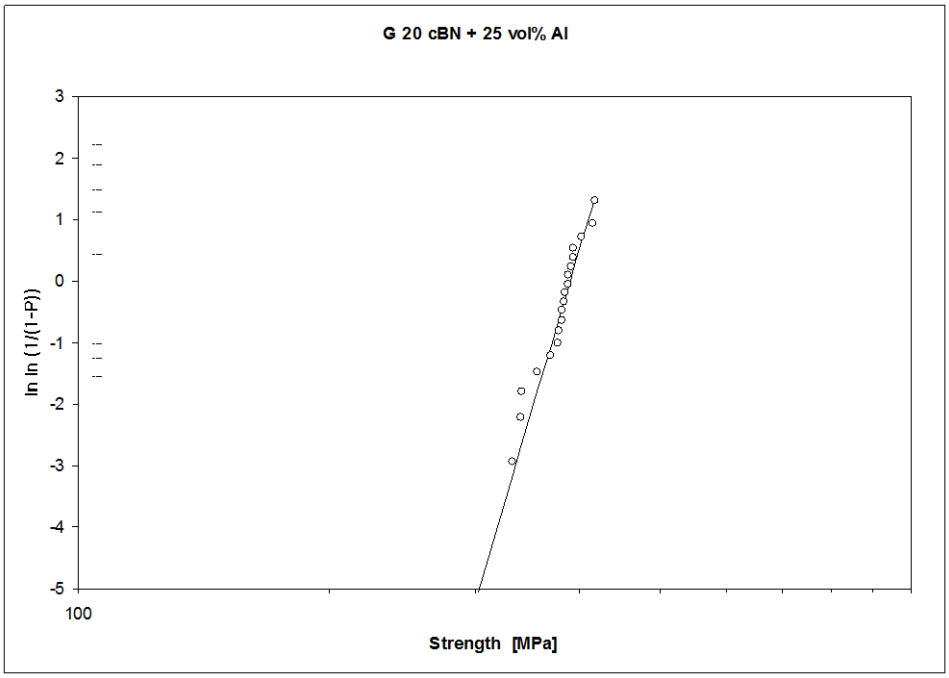

Table I. 11: Flaw type and size for G20 cBN + 25% Al

Sample No:	Flaw type	Strength (MPa)	Flaw Size (µm)
7	B	418	
4	P	414	208
10	P	403	
3	B @ edge	394	246
11	B	394	
14	? P	391	
19	? P	387	
12	B	387	
1	B	384	
18	B	383	
5	P	381	
2	P	381	
17	P	378	
8	P	376	
13	?P	369	
15	B	356	
9	?	341	
6	B	340	
16	Large P/B in middle	332	126

Appendix J: Statistical Analysis of Properties

Hardness:

General Linear Model: Hardness versus Grain size, Al-content

```
Factor      Type   Levels  Values
Grain size  fixed       4  G02, G06, G10, G20
Al-content  fixed       3  15, 20, 25

Analysis of Variance for Hardness, using Adjusted SS for Tests

Source      DF   Seq SS   Adj SS   Adj MS       F      P
Grain size   3  3502.48  3075.66  1025.22  275.50  0.000
Al-content   2  1260.02  1260.02   630.01  169.30  0.000
Error       74   275.37   275.37     3.72
Total       79  5037.88
S = 1.92906   R-Sq = 94.53%   R-Sq(adj) = 94.16%
```

Test for Equal Variances: Hardness_1 versus Al-content
One-way ANOVA: Hardness_1 versus Grain Size_1

```
Source        DF       SS      MS       F      P
Grain Size_1   9  4887.61  543.07  252.98  0.000
Error         70   150.27    2.15
Total         79  5037.88
S = 1.465   R-Sq = 97.02%   R-Sq(adj) = 96.63%

                          Individual 95% CIs For Mean Based on
                          Pooled StDev
Level   N    Mean  StDev  ---------+---------+---------+---------+
G02-15  8  40.740  1.195                                       (*-)
G02-20  8  33.535  1.151                           (-*)
G02-25  8  32.060  1.648                         (-*)
G06-15  8  36.058  1.385                               (-*)
G06-20  8  27.198  0.380                   (-*)
G06-25  8  22.003  1.473           (*-)
G10-15  8  35.840  2.514                               (*-)
G20-15  8  23.239  1.743             (*-)
G20-20  8  19.828  1.505       (*-)
G20-25  8  15.638  0.378  (*-)
                          ---------+---------+---------+---------+
                                21.0      28.0      35.0      42.0

Pooled StDev = 1.465
```

This shows that there are significant differences between the grain size and binder content of the various materials and their effect on the hardness. The grain size has a larger effect on the hardness than the binder content.

Fracture Toughness:

General Linear Model: K1c versus Grain size, Al-content

```
Factor      Type   Levels  Values
Grain size  fixed       4  G02, G06, G10, G20
Al-content  fixed       3  15, 20, 25

Analysis of Variance for K1c, using Adjusted SS for Tests

Source      DF   Seq SS   Adj SS  Adj MS     F      P
Grain size   3   5.6544   5.7495  1.9165  5.96  0.002
Al-content   2   1.7688   1.7688  0.8844  2.75  0.076
Error       41  13.1863  13.1863  0.3216
Total       46  20.6095
S = 0.567112   R-Sq = 36.02%   R-Sq(adj) = 28.22%
Unusual Observations for K1c
```

One-way ANOVA: K1c versus Grain size

```
Source      DF      SS     MS     F      P
Grain size   3   5.654  1.885  5.42  0.003
Error       43  14.955  0.348
Total       46  20.610
S = 0.5897   R-Sq = 27.44%   R-Sq(adj) = 22.37%


                          Individual 95% CIs For Mean Based on
                          Pooled StDev
Level   N    Mean   StDev  --------+---------+---------+---------+-
G02    14  6.9092  0.4646  (-----*------)
G06    14  7.2376  0.8238        (------*-----)
G10     5  8.0331  0.0480                 (----------*---------)
G20    14  7.5364  0.5052              (------*-----)
                          --------+---------+---------+---------+-
                                7.00      7.50      8.00      8.50

Pooled StDev = 0.5897
```

This shows that there is only a significant difference in the fracture toughness of the G2 and G10 and G20 materials.

One-way ANOVA: K1c versus Al-content

```
Source      DF      SS     MS     F      P
Al-content   2   1.674  0.837  1.94  0.155
Error       44  18.936  0.430
Total       46  20.610
S = 0.6560   R-Sq = 8.12%   R-Sq(adj) = 3.94%

Individual 95% CIs For Mean Based on
                          Pooled StDev
Level   N    Mean   StDev  -------+---------+---------+---------+--
15     18  7.3754  0.9508             (----------*---------)
20     15  7.4991  0.4715                 (----------*----------)
```

```
25     14  7.0347  0.1870  (----------*----------)
                           -------+---------+---------+---------+--
                                6.90      7.20      7.50      7.80

Pooled StDev = 0.6560
```

This shows that there is very little significant difference between the fracture toughness for the 15, 20 and 25% materials, they all overlap.

Strength:

General Linear Model: Flexural Strength versus Grain Size_1, Al-content

```
Factor        Type   Levels  Values
Grain Size_1  fixed       4  G02, G06, G10, G20
Al-content    fixed       3  15, 20, 25

Analysis of Variance for Flexural Strength, using Adjusted SS for Tests

Source          DF  Seq SS  Adj SS  Adj MS      F      P
Grain Size_1     3   88126   94502   31501  18.50  0.000
Al-content       2   33645   33645   16822   9.88  0.000
Error          191  325302  325302    1703
Total          196  447072
S = 41.2692   R-Sq = 27.24%   R-Sq(adj) = 25.33%

Unusual Observations for Flexural Strength
```

One-way ANOVA: Flexural Strength versus Grain size

```
Source       DF      SS     MS      F      P
Grain size    9  151284  16809  10.63  0.000
Error       187  295788   1582
Total       196  447072
S = 39.77   R-Sq = 33.84%   R-Sq(adj) = 30.65%


                          Individual 95% CIs For Mean Based on
                          Pooled StDev
Level    N    Mean  StDev  ------+---------+---------+---------+---
G02-15  18  371.70  40.81         (----*----)
G02-20  20  406.25  61.08                   (----*----)
G02-25  20  425.77  41.90                         (----*----)
G06-15  20  379.81  71.76            (----*----)
G06-20  20  381.10  29.42            (----*----)
G06-25  20  417.71  23.04                      (----*----)
G10-15  20  443.87  22.74                            (----*----)
G20-15  20  383.92  25.06             (----*----)
G20-20  20  346.69  19.67  (----*----)
G20-25  19  379.47  23.28           (----*-----)
                          ------+---------+---------+---------+---
                              350       385       420       455

Pooled StDev = 39.77
```

One-way ANOVA: Flexural Strength versus Al-content

```
Source       DF      SS     MS     F      P
Al-content    2   27268  13634  6.30  0.002
Error       194  419804   2164
Total       196  447072
S = 46.52   R-Sq = 6.10%   R-Sq(adj) = 5.13%


                          Individual 95% CIs For Mean Based on
                          Pooled StDev
Level   N    Mean  StDev  ------+---------+---------+---------+---
15     78  395.42  52.53              (------*------)
20     60  378.01  47.02  (-------*-------)
25     59  408.13  36.40                       (-------*-------)
                          ------+---------+---------+---------+---
                              375       390       405       420

Pooled StDev = 46.52
```

This shows that there is very little significant difference between the strength for the 15, 20 and 25% materials, they all overlap.

One-way ANOVA: Flexural Strength versus Grain Size_1

```
Source         DF      SS     MS      F      P
Grain Size_1    3   88126  29375  15.79  0.000
Error         193  358946   1860
Total         196  447072
S = 43.13   R-Sq = 19.71%   R-Sq(adj) = 18.46%


                          Individual 95% CIs For Mean Based on Pooled StDev
Level   N    Mean  StDev    +---------+---------+---------+---------
G02    58  402.26  53.10              (---*---)
G06    60  392.87  49.21           (---*---)
G10    20  443.87  22.74                       (-----*-----)
G20    59  369.87  28.01    (--*---)
                            +---------+---------+---------+---------
                          360       390       420       450

Pooled StDev = 43.13
```

This shows that the strength of the G10 and G20 are significantly different, while very little difference between G2 and G6.

Calculation of the % Contribution:

Grain Size and Binder content contributions to Hardness:

$$\%Grain\_Size = \frac{3502.48}{5037.88} \times 100 = 69.52\%$$
$$\%Binder = \frac{1260.02}{5037.88} \times 100 = 25.01\%$$
$$\%error = 100 - 69.52 - 25.01 = 5.47\%$$

R-Sq = 94.53%

This suggests that the grain size and binder content have a good fit to the general linear model for Hardness. The grain size has a larger contribution to the hardness than the binder content.

Grain Size and Binder content contributions to Fracture Toughness:

$$\%Grain\_Size = \frac{5.6544}{20.6095} \times 100 = 27.43\%$$
$$\%Binder = \frac{1.7688}{20.6095} \times 100 = 8.58\%$$
$$\%error = 100 - 27.43 - 8.58 = 63.98\%$$

R-Sq = 36.02%

This suggests that the cBN grain size and binder content have a very poor fit to the general linear model of the Fracture toughness results.

Grain Size and Binder content contributions to Strength:

$$\%Grain\_Size = \frac{88126}{447072} \times 100 = 19.71\%$$
$$\%Binder = \frac{33645}{447072} \times 100 = 7.52\%$$
$$\%error = 100 - 19.71 - 7.52 = 72.76\%$$

R-Sq = 27.24%

This suggests that the cBN grain size and binder content have a very poor fit to the general linear model of the Strength results.